

# Upgrading of Lignocellulose-Derived Sugars to Value-Added Chemicals via Heterogeneously Catalyzed Continuous-Flow Processes

---

vorgelegt von

Dipl.-Ing.

**Marius Bäuml**

ORCID: 0000-0002-3665-9398

von der Fakultät II – Mathematik und Naturwissenschaften  
der Technischen Universität Berlin  
zur Erlangung des akademischen Grades

Doktor der Ingenieurwissenschaften

– Dr.-Ing. –

**genehmigte Dissertation**

## **Promotionsausschuss:**

Vorsitzender: Prof. Dr. Arne Thomas

Gutachter: Prof. Dr. Markus Antonietti

Gutachter: Prof. Dr. Reinhard Schomäcker

**Tag der wissenschaftlichen Aussprache:** 01. Oktober 2019

Berlin 2019



## ABSTRACT (ENGLISH)

---

In the present work, a methodology is proposed for the synthesis of metal-based hydrogenation catalysts supported on hierarchically porous carbon pellets, which are suitable for industrial flow processes. For the preparation of the carbon support, durum semolina is used as the carbon source, in addition to ZnO nanopowder as the porogenic templating agent. Owing to their large surface area of  $756 \text{ m}^2 \text{ g}^{-1}$  and mesopore volume of  $0.49 \text{ cm}^3 \text{ g}^{-1}$  (QSDFT  $\text{N}_2$  adsorption), the extruded cylindrical pellets ( $2.4 \times 3.5 \text{ mm}$ ) offer excellent properties as a support material for highly active catalyst pellets, tailored to the use in large packed bed reactors.

The performance of the Ni/C and Pt/C catalysts, prepared with several metal loadings from the support pellets, is investigated in packed-bed flow reactors for two important applications of biomass valorization: the hydrogenation of the bioderived platform molecules 5-hydroxymethylfurfural (HMF) and levulinic acid (LA) to the value-added chemicals 2,5-dimethylfuran (DMF) and  $\gamma$ -valerolactone (GVL), respectively. Aiming at the development of sustainable processes, only water and ethanol are used as green solvents in these processes.

In the selective hydrogenation of HMF in ethanol over the synthesized 21wt% Ni/C catalyst, a DMF yield of 80.5% (99.0% conversion) is obtained at  $150^\circ\text{C}$ . High catalytic stability is observed during the whole operation period of 33 h.

For the hydrogenation of LA to GVL in water at  $160^\circ\text{C}$ , the prepared 2.7wt% Pt/C catalyst provides excellent GVL yield of 96.4% (98.9% conversion) and a Pt time yield of  $54.7 \text{ mol}_{\text{GVL}} \text{ h}^{-1} \text{ mol}_{\text{Pt}}^{-1}$  (66.2% conversion).

With formic acid (FA) as an alternative and renewable hydrogen source, the GVL selectivity was further enhanced to 98.7% (65.3% LA conversion) and a 92.6% GVL yield (97.7% LA conversion) was obtained, using the same type of 2.7wt% Pt/C catalyst at  $220^\circ\text{C}$ . The high activity and remarkable selectivity of the FA-assisted hydrogenation demonstrates its potential for a sustainable and self-sufficient integrated refining strategy of sugars to GVL, in which *in situ* formed FA can be employed as a bioderived reducing agent.

---





## ABSTRACT (DEUTSCH)

---

In der vorliegenden Arbeit wird eine Synthesemethodik vorgestellt für metallbasierte, auf hierarchisch porösen Kohlenstoffpellets geträgerte Hydrierkatalysatoren, welche sich für die Anwendung in industriellen Flussprozessen eignen. Für die Synthese des Kohlenstoffträgers wird Hartweizengrieß als Kohlenstoffquelle sowie ZnO-Nanopulver als porenbildendes Template verwendet. Die extrudierten zylindrischen Pellets ( $2,4 \times 3,5$  mm) bieten mit ihrer großen Oberfläche von  $756 \text{ m}^2 \text{ g}^{-1}$  und ihrem großen Mesoporenvolumen von  $0,49 \text{ cm}^3 \text{ g}^{-1}$  (QSDFT für  $\text{N}_2$ -Adsorption) ausgezeichnete Voraussetzungen als Trägermaterial für hochaktive Katalysatoren für die Nutzung in Festbett-Rohrreaktoren.

Die synthetisierten Ni/C- und Pt/C-Katalysatoren, welche mit verschiedenen Metallbeladungen aus den Trägerpellets hergestellt wurden, werden hinsichtlich ihrer katalytischen Reaktivität in Festbettreaktoren anhand zweier bedeutender Anwendungen der Biomasseveredelung untersucht: Hydrierung der biobasierten Plattformchemikalien 5-Hydroxymethylfurfural (HMF) bzw. Lävulinsäure (LA) hin zu den veredelten Chemikalien 2,5-Dimethylfuran (DMF) bzw.  $\gamma$ -Valerolacton (GVL). Um nachhaltige Prozesse im Sinne der grünen Chemie zu entwickeln, werden hierbei als grüne Lösungsmittel ausschließlich Wasser und Ethanol eingesetzt.

Für die selektive HMF-Hydrierung in Ethanol über dem synthetisierten 21 gew.% Ni/C Katalysator wurde 80,5% DMF-Ausbeute (99,0% HMF-Umsatz) bei  $150^\circ\text{C}$  erzielt. Während der gesamten Betriebszeit von 33 h konnte hohe katalytische Stabilität beobachtet werden.

Für die LA-Hydrierung zu GVL in Wasser erreichte der synthetisierte 2,7 gew.% Pt/C Katalysator bei  $160^\circ\text{C}$  exzellente GVL-Ausbeute von 96,4% (98,9% Umsatz) und Pt-Zeitausbeute von  $54,7 \text{ mol}_{\text{GVL}} \text{ h}^{-1} \text{ mol}_{\text{Pt}}^{-1}$  (66,2% Umsatz).

Mit Ameisensäure (FA) als alternativer und regenerativer Wasserstoffquelle wurden unter Verwendung des gleichen 2,7% Pt/C-Katalysators bei  $220^\circ\text{C}$  zudem die GVL-Selektivität auf 98,7% (65,3% LA-Umsatz) gesteigert und eine GVL-Ausbeute von 92,6% (97,7% LA-Umsatz) erzielt. Die hohe Aktivität und außerordentliche Selektivität bei der FA-vermittelten Hydrierung zeigt das Potenzial auf für eine nachhaltige und autarke Veredelungsstrategie von Zuckern zu GVL, wobei die *in situ* geformte FA als biobasiertes Reduktionsmittel dienen kann.

---



# CONTENTS

<b>Abstract (English)</b> .....	<b>iii</b>
<b>Abstract (Deutsch)</b> .....	<b>v</b>
<b>Contents</b> .....	<b>vii</b>
<b>Notation</b> .....	<b>ix</b>
<b>1 Introduction</b> .....	<b>1</b>
1.1 Motivation .....	1
1.2 Objective of the Present Work .....	4
<b>2 State of the Art</b> .....	<b>7</b>
2.1 Biorefinery and the Principles of Green Chemistry .....	7
2.2 Lignocellulosic Biomass .....	9
2.3 Pretreatment of Lignocellulosic Biomass .....	11
2.4 Solid Acid Catalysts for Cellulose Upgrading .....	12
2.4.1 Cellulose Depolymerization .....	12
2.4.2 Production of 5-Hydroxymethylfurfural and Levulinic Acid .....	13
2.5 Hydrogenation over Metal-based Catalysts .....	17
2.5.1 Production of 2,5-Dimethylfuran from 5-Hydroxymethylfurfural .....	17
2.5.2 Production of $\gamma$ -Valerolactone from Levulinic Acid .....	19
<b>3 Catalyst Design and Characterization</b> .....	<b>25</b>
3.1 Synthesis of Pelletized Carbon Supports .....	25
3.1.1 Salt-melt Templating with $\text{ZnCl}_2$ Solution .....	27
3.1.2 Hard Templating with NaCl Crystals .....	31
3.1.3 Hard Templating and Activation with ZnO Nanopowder .....	33
3.2 Incorporation of Metal Nanoparticles .....	39
3.2.1 Nickel .....	39
3.2.2 Platinum .....	46
3.3 Solid Acid Catalyst .....	48
3.3.1 Characterization .....	48
3.4 Solid Base Catalyst .....	50
3.4.1 Characterization .....	50

<b>4 Reactor Design</b>	<b>53</b>
4.1 Continuous Flow Set-up	53
4.2 Flow Dispersion	57
<b>5 Catalyst Performance</b>	<b>61</b>
5.1 Valorization of Sugars	63
5.1.1 Dehydration of Fructose	63
5.1.2 Conversion of Glucose	64
5.2 Hydrodeoxygenation of 5-Hydroxymethylfurfural	70
5.3 Hydrogenation of Levulinic Acid	89
5.3.1 External Molecular Hydrogen	89
5.3.2 Formic Acid as Hydrogen Source	93
<b>6 Conclusion and Outlook</b>	<b>103</b>
<b>A Materials and Methods</b>	<b>107</b>
A.1 Chemicals and Materials	107
A.2 Applied Methods	108
A.2.1 Product Analysis Methods	108
A.2.2 Characterization Methods	109
<b>Acknowledgment</b>	<b>115</b>
<b>List of Tables</b>	<b>117</b>
<b>List of Figures</b>	<b>119</b>
<b>References</b>	<b>123</b>

## Symbols

Symbol	Unit	Description
$A$	$\text{L g}_M \text{h}^{-1}$	Pre-exponential factor (unit valid for first order reaction)
$Bo$	---	Bodenstein number
$C_i$	$\text{mol L}^{-1}$	Concentration of component $i$ in solution
$C_i$	$\text{mol kg}^{-1}$	Concentration of active sites $i$ on catalyst
$d$	$\text{nm}; \mu\text{m}; \text{mm}$	Diameter
$d_s$	$\text{nm}$	Equivalent spherical diameter (see section 4.2)
$E_a$	$\text{kJ mol}^{-1}$	Activation energy
$k$	$\text{L g}_M \text{h}^{-1}$	Rate constant (unit valid for first order reaction)
$L$	$\text{mm}$	Length
$m_i$	$\text{g}$	Weight of catalyst, species, or element $i$
$M_i$	$\text{g mol}^{-1}$	Molar mass of species $i$
$n$	---	Reaction order (partial or overall)
$NTY_i$	$\text{mol}_i \text{h}^{-1} \text{mol}_{\text{Ni}}^{-1}$	Nickel time yield (molar)
$NTY_i$	$\text{g}_i \text{h}^{-1} \text{g}_{\text{Ni}}^{-1}$	Nickel time yield (specific)
$P$	$\text{bar}$	Total pressure
$PTY_i$	$\text{mol}_i \text{h}^{-1} \text{mol}_{\text{Pt}}^{-1}$	Platinum time yield (molar)
$PTY_i$	$\text{g}_i \text{h}^{-1} \text{g}_{\text{Pt}}^{-1}$	Platinum time yield (specific)
$r$	$\text{mol}_i \text{h}^{-1} \text{g}_M^{-1}$	Reaction rate (commonly), $r := m_M^{-1} \text{d}N_i/\text{d}t$
$r$	$\text{mol}_i \text{h}^{-1} \text{mol}_M^{-1}$	Reaction rate (molar), $r := N_M^{-1} \text{d}N_i/\text{d}t$
$R$	$\text{J mol}^{-1} \text{K}^{-1}$	Universal gas constant, $R = 8.314 \text{ J mol}^{-1} \text{K}^{-1}$
$SSA$	$\text{m}^2 \text{g}^{-1}$	Specific surface area of porous particle
$S_i$	%	Overall selectivity towards component $i$
$T$	$\text{K}; ^\circ\text{C}$	Reaction temperature
$TOF$	$\text{mol}_i \text{h}^{-1} \text{mol}_M^{-1}$	Turnover frequency of metal $M$ (Ni or Pt)
$TOS$	$\text{h}$	Time on stream

Symbol	Unit	Description
$V_p$	$\text{m}^3 \text{g}^{-1}$	Pore volume
$V_m^{STP}$	$\text{mL}_{\text{STP}} \text{mol}^{-1}$	Molar volume of ideal gas at STP, $V_m^{STP} = 22\,414 \text{ mL}_{\text{STP}} \text{mol}^{-1}$
$w_i$	wt%	Weight fraction of element $i$
$X$	%	Conversion
$Y_i$	%	Yield towards species $i$
$\varepsilon_p$	%	Catalyst pellet porosity
$\varepsilon_{bed}$	%	Bed voidage (bed porosity)
$\rho_m$	$\text{mol m}^{-3}$	Molar density
$\tau$	$\text{s g}_{\text{cat}} \text{mol}_{\text{react}}^{-1}$	Space time (commonly), $\tau := m_{\text{cat}}/\dot{N}_{\text{react}}^0$
$\tau_w$	$\text{s g}_{\text{cat}} \text{g}_i^{-1}$	Space time (weight specific), $\tau_w := m_{\text{cat}}/\dot{m}_{\text{react}}^0$
$\tau_N$	$\text{s mol}_{\text{cat}} \text{mol}_{\text{react}}^{-1}$	Space time (molar), $\tau_N := N_{\text{cat}}/\dot{N}_{\text{react}}^0$

## Indices

### Subscripts

<i>0</i>	Initial (before reaction, dissociation etc.)
<i>ana</i>	Analyte
<i>C</i>	Carbon support pellet
<i>cat</i>	Catalyst pellet
<i>g</i>	Gas phase
<i>l</i>	Liquid phase
<i>M</i>	Metal (Ni, Pt, Ru)
<i>p</i>	Pore
<i>R</i>	Reactor
<i>s</i>	Solid phase (catalyst and dilution)
<i>SA</i>	Solid acid catalyst
<i>tit</i>	Titrant
<i>tot</i>	Total (incl. all intermediates, products, and byproducts)
<i>w</i>	Reactor wall

### Superscripts

<i>cu</i>	Cumulative
<i>eq</i>	At equivalence point of titration
<i>h</i>	Hypothetical

## Abbreviations

Acronym	Description
2-MTHF	2-Methyltetrahydrofuran
2-PEA	2-Pentenoic acid
3-PEA	3-Pentenoic acid
5-MF	5-Methylfurfural
BET	Brunauer-Emmett-Teller theory of gas physisorption
BHMF	2,5-Bis(hydroxymethyl)furan
BJH	Barrett-Joyner-Halenda method for mesopore size analysis
C, C <sub>ZnO</sub>	Carbon support pellet synthesized on the ZnO route (see section 3.1.3)
C <sub>NaCl</sub>	Carbon support pellet synthesized on the NaCl route (see section 3.1.2)
C <sub>ZnCl</sub>	Carbon support pellet synthesized on the ZnCl <sub>2</sub> route (see section 3.1.1)
DMF	2,5-Dimethylfuran
DMTHF	2,5-Dimethyltetrahydrofuran
EMF	5-Ethoxymethylfurfural
EMHMF	2-Ethoxy-5-hydroxymethylfuran
EMMF	2-Ethoxymethyl-5-methylfuran
FA	Formic acid
FID	Flame ionization detector
GC	Gas chromatograph
GVL	$\gamma$ -Valerolactone
GHVA	$\gamma$ -Hydroxyvaleric acid
HD	2,5-Hexanedione
HDO	Hydrodeoxygenation
HMF	5-Hydroxymethylfurfural
HMF-Ac	“HMF acetal” [5-(diethoxymethylfuran-2-yl)methanol]
HPLC	High performance liquid chromatography
ID	Inner diameter
IL	Ionic liquid
ICP	Inductively coupled plasma
IWI	Incipient wetness impregnation
LA	Levulinic acid
LCB	Lignocellulosic biomass



OD	Outer diameter
OD××	Reactor with outer diameter of ×× mm (see section 4.1)
MC	microcrystalline
MFA	5-Methylfurfuryl alcohol
MS	Mass spectrometry/spectrometer
NTY	Nickel time yield
PFR	Plug flow reactor
PTY	Platinum time yield
QSDF	Quenched Solid State Functional Theory for pore size analysis
PSS	Crosslinked polystyrene sulfonate (= polystyrene- <i>co</i> -divinylbenzene)
RDS	Reaction determining step
SEM	Scanning electron microscopy/microscope
SSA	Specific surface area
STP	Standard temperature (0 °C) and pressure (1 atm)
TEM	Transmission electron microscopy/microscope
TOS	Time-on-stream
VOC	Volatile organic compounds
XRD	X-ray powder diffraction
wt	Weight fraction



# 1

## INTRODUCTION

### 1.1 Motivation

The extensive environmental and social impact of crude oil exploitation is a hot topic in science, technology, and society. Almost every aspect of our life is driven by the utilization of this raw material, which is the predominant resource for most chemicals, materials, consumables, and especially transportation fuels. However, the centralized crude oil exploitation creates strong economic and political dependencies on a handful of regions that comprise the most part of the earth's oil occurrence. In addition, the global demand for energy and consumables is increasing each year. Considering the advancing depletion of crude oil reserves, the production and supply of energy and materials will be challenging in the future. The global crude oil exploitation is assumed to pass through a maximum – the so-called Hubbert's peak – within the next 50 years, followed by a continuous decline<sup>1</sup>. Therefore, the accessibility of crude oil, on which our prosperity is established, can be more and more limited or uncertain in the future.

Regarding this imbalance of rising demand of energy and petroleum-based products on the one hand versus the depletion of oil reserves on the other hand, it is paramount to focus on new strategies to ensure our standard of living for the future. Therefore, interest is rising in renewable and more sustainable alternatives for the energy supply and production of chemical building blocks<sup>2</sup>, based on the utilization of biomass.

In addition, combustion of petrochemical products, such as fuels and unrecycled polymers, increases the CO<sub>2</sub> emissions because the carbon cycle is not closed. By displacing such products

by bioderived products, the net CO<sub>2</sub> emissions can be balanced through accelerated biomass regrowth<sup>3</sup> and, therefore, the greenhouse effect can be mitigated. The effectiveness of the additional CO<sub>2</sub> uptake and carbon sequestration, associated with the growth and harvest of biomass for biorefinery, depends on many factors, such as the type of biomass, the ecosystem aboveground and belowground, the conversion of land use, the diversion of the crop components, and the treatment and refining processes<sup>4</sup>. However, it is believed that the production and use of biofuels from lignocellulosic feedstocks grown on marginal lands offer almost carbon neutrality<sup>4</sup>.

Among the several classes of biomass, the predominant type is lignocellulosic biomass (LCB), which comprises all terrestrial plants. It is categorized into virgin biomass and biomass waste. The first category includes naturally occurring plants such as trees, bushes, and small vegetation, whereas the latter accrues in large amounts in the agricultural industry (sugarcane bagasse, corn stover, straw), forestry-related industries (paper pulp, saw mill) and domestic organic waste. The high availability of low-value biomass emphasizes the importance of establishing industrial processes capable of converting the mentioned abundant feedstock into platform molecules that form the basis of a holistic biobased chemical industry. In this context, cellulose is of particular interest, as it is the major component of LCB (ca. 35-50%, depending on the type of plant) and, therefore, the most abundant natural carbon source on earth. Through diverse treatment technologies, this biopolymer can be cleaved into the repeating unit glucose and further isomerized towards fructose.

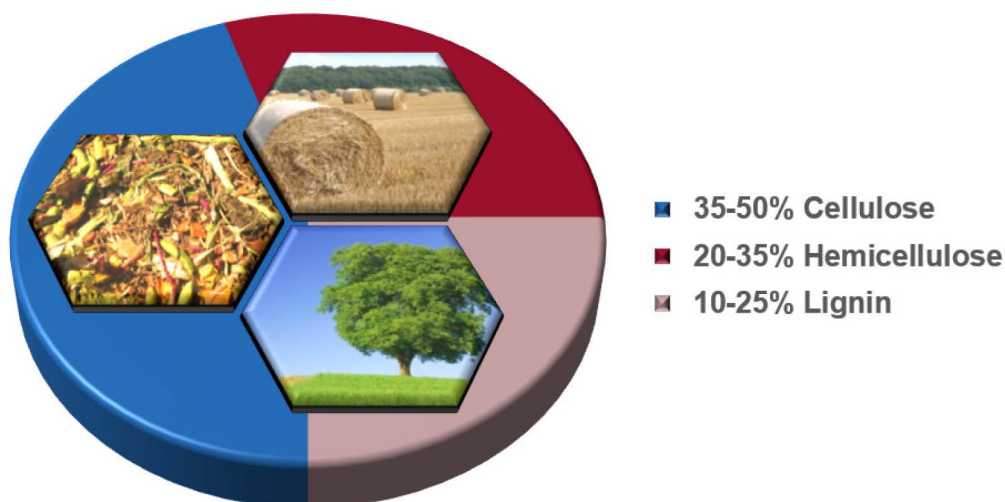


**Figure 1-1:** Main components of lignocellulosic biomass

To pave the way for a shift towards renewable resources, the U.S. Department of Energy published in 2004 a list of twelve top value-added chemicals that can be produced from biomass

and are considered the most important building blocks for establishing an extensive refining industry based on biomass<sup>5</sup> (Table 1-1).

**Table 1-1:** Twelve top value-added chemicals as building blocks for biorefinery, according to the U.S. Dept. of Energy<sup>5</sup>

Succinic/fumaric/malic acid	Aspartic acid	Itaconic acid	Glycerol
2,5-Furandicarboxylic acid	Glucaric acid	Levulinic acid	Sorbitol
3-Hydroxypropionic acid	Glutamic acid	3-Hydroxybutyrolactone	Xylitol/arabinitol

Among these molecules is levulinic acid (LA), which is produced from 5-hydroxymethylfurfural (HMF), the dehydration product of fructose and glucose. HMF is often referred to as the “sleeping giant”<sup>6</sup>, hinting at its large unexploited potential as a versatile building block for the production of various biofuels, chemicals, and polymers. LA is the starting point of several upgrading schemes towards value-added chemicals such as  $\gamma$ -valerolactone (GVL), 2-methyltetrahydrofuran, and valeric acid, which find application as precursors for products in various fields, such as fuels, fuel additives, polymers, resins, solvents, pharmaceuticals, and flavors. Apart from the conversion towards LA, HMF can be transformed into 2,5-dimethylfuran (DMF). Beyond the promising use as a high-quality biofuel, DMF is a precursor for the production of renewable *p*-xylene, which is of crucial importance for the chemical and polymer industry<sup>7</sup>.

Despite the great potential of biorefinery, to date only few processes are implemented already in a mature stage and cost-efficient way, such as the production of bioethanol for the use as biofuel<sup>8</sup>. However, conventional bioethanol production is based on the use of food sources and entails diversion of food sources. The resulting increase in food prices is already placing millions of people at risk for going hungry (“food-vs.-fuel” dilemma)<sup>9</sup>. Therefore, efforts are being made in academia and industry to substitute gasoline and bioethanol by other biofuels that are produced in a more sustainable fashion and offer superior fuel properties.

As an example, DMF exhibits promising fuel properties superior to those of bioethanol and even conventional gasoline, including a high research octane rating of 119, immiscibility with water, and lower volatility<sup>10,11</sup>. Furthermore, its energy density is 40% higher compared with bioethanol (30 vs. 21 MJ/L) and the stoichiometric carbon efficiency of DMF production is 100%, while in the case of bioethanol 33% of the carbon source is already emitted as CO<sub>2</sub> during the fermentation process<sup>11</sup>.

**Table 1-2:** Fuel properties of bioethanol, DMF, and gasoline

Property	Bioethanol	DMF	Gasoline
Energy density	21 MJ/L <sup>11</sup>	30 MJ/L <sup>11</sup>	32 MJ/L <sup>11</sup>
Research octane number	110 <sup>11</sup>	119 <sup>11</sup>	95.8 <sup>11</sup>
Boiling temperature	78 °C	94 °C	35–200 °C
Hygroscopic	Yes	No	No
Carbon efficiency of production	67%	100%	100%

## 1.2 Objective of the Present Work

Due to the importance of the mentioned platform molecules fructose, HMF, and LA for biorefining schemes, the selective production and transformation of these compounds towards the value-added products DMF and GVL is the focus of the present work.

For many catalytic applications, a necessary step for the scale-up of laboratory catalysis to a process of industrial extent is the implementation of a continuous-flow system rather than a batch process. Compared with batch systems, continuous-flow operation can offer a variety of advantages, *e.g.* in terms of cost efficiency and the potential to integrate sequential catalyzed reaction steps into a multiprocess system<sup>12,13</sup>. Since operation in continuous flow entails different technical requirements than batch processes, it is necessary to develop catalysts that are tailored to efficient continuous-flow processes. This includes the necessity for low pressure drop along the reactor axis, which requires the catalyst to be in macroscopic shapes (*e.g.* granules or pellets of uniform size) instead of polydisperse fine powders. However, most of the current research on the mentioned valorization schemes is dedicated to laboratory-scale catalysis in batch systems and neglects the question of industrial feasibility.

Therefore, the objective of this work is to develop catalyzed processes for the conversion of sugars towards furanic platform molecules and consecutive value-added chemicals in continuous-flow systems, bridging the gap to actual industrial conditions. To establish efficient hydrogenation applications for the production of the target molecules DMF and GVL, the present work provides a simple and cost-efficient synthesis methodology for high-performance hydrogenation catalysts. In this novel approach, active metal was incorporated on extruded carbon pellets with very high surface area and pore volume. In an iterative procedure, the methodology was enhanced by adjusting the composition of the precursor mixture with different carbon sources and porogenic templating agents.

The performance of the prepared hydrogenation catalysts was subsequently investigated in catalytic flow experiments. This joint interplay of catalyst synthesis and performance testing in packed-bed reactors is outlined in Figure 1-2. The direct performance feedback allows for immediate adjustments of the catalyst synthesis methodology towards better catalytic properties and, therefore, catalyst optimization oriented at large-scale applications.



**Figure 1-2:** Graphical outline of the present work. HMF: 5-hydroxymethylfurfural; LA: levulinic acid; DMF: 2,5-dimethylfuran; GVL:  $\gamma$ -valerolactone



# 2

## STATE OF THE ART

### **2.1 Biorefinery and the Principles of Green Chemistry**

The term biorefinery – in analogy to oil refinery – describes emerging concepts of integrated biomass conversion processes or facilities in which such processes are operated. The processes can be highly different, depending on the diverse biomass feedstocks and on the products, which can be classified into bioenergy (fuels, power, and heat) and biobased products (chemicals and materials)<sup>14</sup>. Among all renewable energy sources, biomass is the only source with a potential for such a dual application<sup>15</sup>. The valorization of the various types of biomass to biofuels and biobased products can be implemented through jointly applied process technologies<sup>2</sup>.

To implement the biorefinery design in a sustainable way, the values of green chemistry have to be respected and integrated into the processes. The area of green chemistry is based upon a set of 12 principles, shown in Figure 2-1, which serve as guidelines for the development of chemical products and processes in a way that protects and benefits the economy, people, and the planet<sup>16</sup>. Among others, these principles include the prevention of waste (rather than treating or cleaning up created waste), maximizing the incorporation of all materials used in the process, using and producing safer and non-toxic substances (rather than chemicals and solvents that are hazardous to humans or the environment), minimizing energy consumption, and, wherever practical, the use of renewable feedstock<sup>16</sup>.



**Figure 2-1:** The 12 principles of green chemistry, according to the ACS Green Chemistry Pocket Guide<sup>16</sup>

The integration of the green chemistry principles into the biorefinery design aims at establishing sustainable technologies for the production of value-added chemicals which have the potential to be competitive with petrochemical processes in the future<sup>2,17</sup>. The evaluation of sustainability of biorefinery processes is very complex and has to be considered under various aspects. Each process must be evaluated individually in terms of its various ecological, social, and economic consequences. For that reason, biorefinery processes are more and more controlled and assessed through certification schemes that monitor the impacts of biorefinery processes and multiprocess systems<sup>18</sup>.

As promising the potential for various application fields of biorefinery appears, as demanding are the challenges for catalysis engineering to implement economic and sustainable solutions of large-scale selective conversion towards value-added products. This does not only apply to the development of suitable catalytic materials, but also to the design of the reactor and a suitable multiprocess environment with integrated pre- and post-treatment, in order to maximize product yields, minimize waste streams, and optimize cost-efficiency<sup>19</sup>.

## 2.2 Lignocellulosic Biomass

Lignocellulosic biomass (LCB) is the most abundant type of renewable resources. It consists of the three biopolymers cellulose, hemicellulose, and lignin, with low amounts of additional components such as minerals, acetyl groups, and phenolic substituents<sup>8</sup>, as presented in Figure 2-2. These polymers are arranged into interconnected non-uniform structures, which can be very different for different types of lignocellulosic biomass. The encapsulation of crystalline cellulose by the hydrophobic lignin-hemicellulose matrix lends the biological material its strength and robustness<sup>20</sup>.

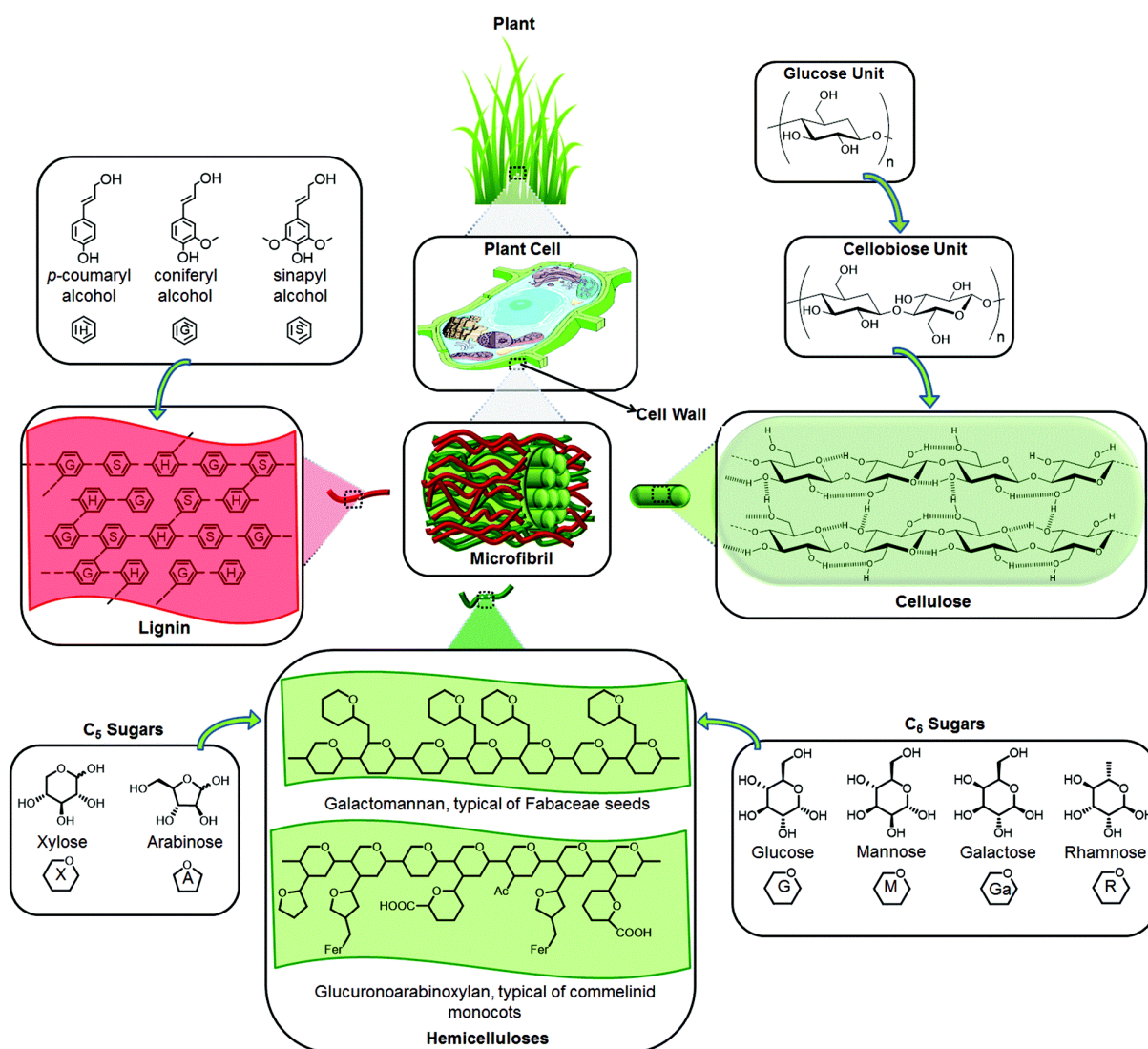


Figure 2-2: Structure and constituents of LCB. Adapted from Isikgor and Becer<sup>8</sup> and edited.

Cellulose, the major constituent of most types of LCB and most abundant biopolymer on earth, is composed of linear chains of thousands of glucose units, linked via  $\beta(1,4)$ -glycosidic bonds.

Extensive intra- and intermolecular hydrogen bonding networks are responsible for the high strength of the crystalline material, which makes it difficult to be hydrolyzed.

Contrary to cellulose, hemicellulose is a heteropolymer, consisting of several different polysaccharides such as xylan and glucuronoxylan, which are composed of several different pentose (xylose, arabinose) and hexose (glucose, mannose, rhamnose, galactose) as well as acetylated sugar units<sup>8</sup>. Hemicellulose has a random, amorphous structure and exhibits lower mechanical and chemical strength than the crystalline cellulose due to a weaker hydrogen bonding network.

Lignin is a cross-linked phenolic polymer composed of phenylpropanoid units<sup>21</sup>. In its function as the cellular glue, it lends tensile strength to the plant tissue<sup>8</sup>. Its structure is based on oxidative coupling of the three building blocks *p*-coumaryl alcohol, coniferyl alcohol, and sinapyl alcohol<sup>22</sup>.

Due to the heterogeneity and chemical and mechanical stability of LCB, sustainable and efficient treatment and valorization of this feedstock is a challenging, but promising task<sup>8</sup>. To make biorefinery processes competitive with the petrochemical industry, which had been established and improved over many decades, strong efforts are currently made in industry and academia on chemistry and engineering issues related to biorefinery fields<sup>17</sup>.

The compositional variety and the higher oxygen content<sup>23</sup>, compared with crude oil, allows for the versatile production of a wider range of products. For the production of biofuels, on the other hand, the high oxygen content of LCB must be decreased in further reaction steps, in order to increase the energy density, decrease the boiling point to a level suitable for liquid fuels, and decrease the solubility with water<sup>24</sup>. The difference in oxygen content of LCB-based products, compared with petroleum and petroleum-based products is illustrated in Figure 2-3.

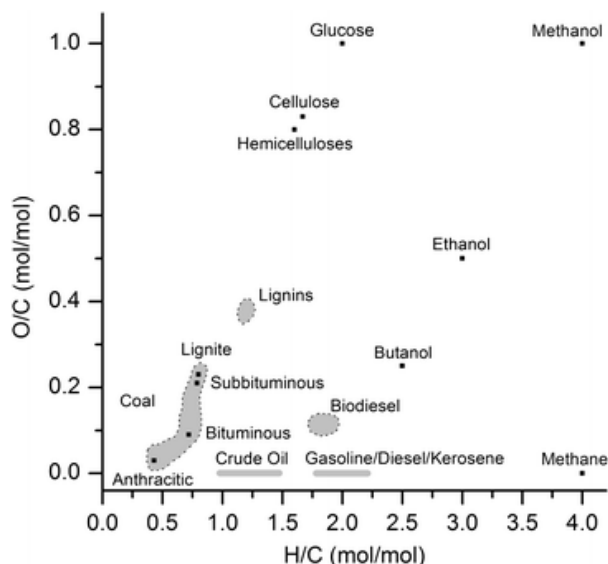


Figure 2-3: O/C and H/C molar ratio for biobased and petroleum-based products. Adapted from Rinaldi and Schüth<sup>23</sup>

## 2.3 Pretreatment of Lignocellulosic Biomass

The crucial first step for the valorization of LCB is the separation into the three major components lignin, cellulose, and hemicellulose<sup>8</sup>. Single-step biomass processing methods, such as pyrolysis, are not desirable as they commonly entail partial deconstruction of the biomass due to the high operation temperature<sup>8</sup>. Instead, pretreatment processes are necessary that are able to crack the supramolecular structure of the lignin-cellulose-hemicellulose matrix and facilitate the isolation of the cellulosic material<sup>25</sup>. Pretreatment of the LCB can involve chemical, mechanical, physical, or biological processes<sup>20</sup>. Amongst other techniques, the biopolymers can be separated by thermal and mechanical fractionation, solubilization, or hydrolysis, with each of these methods providing highly different pretreatment products and offering distinct advantages and disadvantages<sup>26</sup>, while combinations of different pretreatment procedures can be beneficial for the overall efficacy<sup>20</sup>.

Chemical pretreatment techniques for example generally aim at disrupting the LCB matrix by partially hydrolyzing the carbohydrate fractions or by breaking the lignin seal, thus increasing the accessibility of the carbohydrate polymers<sup>27</sup>. Basic pretreatment, *e.g.* with metal hydroxides or ammonia, induces swelling of the LCB, which leads to an increased internal surface area of the material and a decreased degree of polymerization<sup>20</sup>. By disrupting the structure of lignin, the linkage of the lignin with the cellulose and hemicellulose is broken. Alternatively, acidic treatment in dilute sulfuric, hydrochloric, and phosphoric acid selectively depolymerizes the hemicellulose up to its monomer units, which makes the cellulose more accessible<sup>20</sup>.

The complexity of the raw material itself, the different pretreatment techniques, as well as the various possibilities for the combination and integration of subsequent valorization steps still pose great challenges, but also provide a large potential for developing efficient and cheap pretreatment technologies<sup>27</sup>.

## 2.4 Solid Acid Catalysts for Cellulose Upgrading

### 2.4.1 Cellulose Depolymerization

With an approximate fraction of *ca.* 55-85% of the matter, C<sub>5</sub> and C<sub>6</sub> sugars comprise the major part of the dried LCB<sup>8</sup>, chemically linked *via* glycosidic bonds into the biopolymers cellulose and hemicellulose. Complete hydrolysis of these bonds towards the monosaccharides constitutes the starting point for the various valorization pathways. Due to the highly interconnected crystalline network of cellulose and high stability of its  $\beta$ -1,4-glycosidic bonds that link the glucose units, the depolymerization of cellulose is particularly challenging. The most efficient industrial saccharification processes involves the use of concentrated hydrochloric acid and sulfuric acid<sup>8,28</sup>. However, such homogeneously catalyzed processes entail additional separation steps of the liquid mineral acids from the product stream.

In search for more sustainable processes that do not entail the issue of catalyst separation, several Lewis and Brønsted acid catalysts have been proposed in science and academia for the hydrolysis<sup>29</sup>; however the key issue remains the very limited solubility of poly- and oligomers in most solvents and, therefore, limited accessibility of solid acid functionalities. Generally, the presence of Cl<sup>-</sup> appears to be beneficial for the hydrolysis of the polysaccharides, as it helps dissolving and adsorbing the carbohydrates<sup>30</sup>. The use of chloric solvents, mainly ionic liquids such as 1-butyl-3-methylimidazolium chloride ([BMIm]Cl), can increase the solubility of the polymers and facilitate solid acid catalysis. Rinaldi *et al.*<sup>31</sup> investigated the performance of cellulose depolymerization in [BMIm]Cl over Amberlyst-15, a commercially available variant of an ion-exchange resin consisting of highly sulfonated polystyrene crosslinked with divinylbenzene units. This macroporous material contains a high density of sulfo groups and is one of the most common representative of polymer-based materials with acidic functional sites<sup>32</sup>. Within 3 hours of reaction time, Rinaldi *et al.*<sup>31</sup> obtained glucose yields of up to 28.8% from cellulose over a high amount of catalyst. In order to intensify the interaction between the cellulose and the solid acid sites, the work of Shuai and Pan<sup>33</sup> proposed the use of a cellulose-mimetic catalyst, a sulfonated chloromethyl polystyrene resin, containing cellulose-binding sites (-Cl) in

vicinity to the catalytic sulfo groups, reportedly obtaining a surprising glucose yield of 93% within 10 h at 120 °C from a small cellulose amount of 100 mg. With the objective of preventing the use of liquid acids, enzymatic processes have been proposed, using a combination of cellulases for the coupled hydrolysis steps of cellulose<sup>34</sup>. The enzymatic treatment of cellulose with endo- and exocellulase yields the soluble di-, tri- and tetrasaccharides<sup>35</sup>, which could be further processed over solid acid catalysts without the use of harsh mineral acids and solvents. For the hydrolysis of the disaccharide intermediate cellobiose in water, Foo *et al.*<sup>36</sup> proposed the use of sulfonated carbon sheets in a fixed-bed reactor at 200 °C, obtaining a cellobiose conversion of up to 50% and glucose yield of up to 26%.

## 2.4.2 Production of 5-Hydroxymethylfurfural and Levulinic Acid

### 2.4.2.1 Fructose as feedstock

HMF is widely obtained by dehydration of fructose. It can be further hydrolyzed and decomposed to levulinic acid (LA) and formic acid (FA), as presented in Figure 2-4.

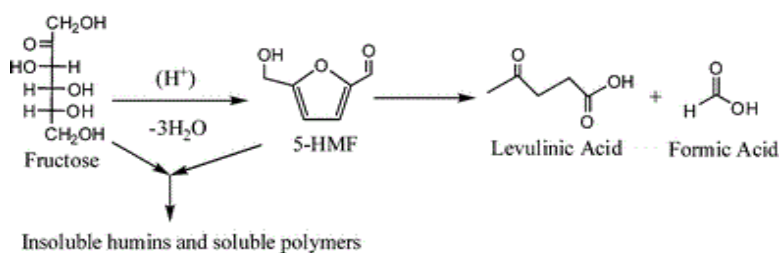


**Figure 2-4:** Scheme of acid-catalyzed fructose dehydration to HMF with consecutive hydrolysis and decomposition to levulinic acid and formic acid. Adapted from Qi *et al.*<sup>37</sup> and edited.

Several Brønsted acids have been identified as efficient homogeneous catalysts – with high or complete conversion for sulfuric acid, phosphoric acid, and hydrochloric acid<sup>30,38</sup>. Since the homogeneous catalysis entails the issue of difficult downstream separation of the catalyst and is therefore not preferable in terms of green chemistry and sustainability, the following section focuses on heterogeneously catalyzed processes that facilitate easy catalyst recovery and recyclability<sup>39</sup>. As the cleaner alternatives to the harsh mineral acids, a variety of solid Brønsted acids has been proposed for the fructose dehydration. In view of the principles of green chemistry, the following paragraph focuses on those works that use greener solvents that are either non-hazardous and bioderived or completely separated and recycled downstream, such as water, isopropanol, 2-butanol, instead of undesirable hazards, such as volatile organic compounds.

Using Amberlyst-70 together with microwave heating for the fructose dehydration in water at 150 °C, Antonetti *et al.*<sup>40</sup> obtained HMF yield of up to 46% and an additional 2% of the



consecutive product LA. Watanabe *et al.*<sup>41</sup> proposed the use of Dowex 50wx8-100, a similar sulfonated polystyrene-divinylbenzene material, which provided 73.4% HMF and ca. 6% LA yield in water-acetone at 150 °C.

Apart from polymers with acid functionalities, zeolites have been successfully employed for the fructose dehydration to HMF. Moreau *et al.*<sup>42</sup> reported the use of H-mordenites, while Nijhuis *et al.*<sup>43</sup> tested H-ZSM-5 and  $\beta$ -zeolite (BEA), obtaining HMF yields of 74, 45, and 32%, for H-mordenites, H-ZSM-5 and  $\beta$ -zeolite, respectively, with all their experiments being conducted in water-methyl isobutyl ketone at 165 °C.

Furthermore, metal oxides with acid sites exhibited catalytic activity for the HMF synthesis from fructose. Qi *et al.*<sup>44</sup> tested TiO<sub>2</sub> and ZrO<sub>2</sub> in water under microwave irradiation at 200 °C, reaching 38.1% and 30.5% HMF yield, respectively.

Despite decent results for several reported HMF production processes *via* acid-catalyzed fructose dehydration, the limited availability and high costs of fructose still pose a challenge for economically competitive large-scale valorization processes. As an example, in an in-depth techno-economic analysis of an simulated industrial catalytic process for the HMF and DMF production from fructose, Kazi *et al.*<sup>45</sup> calculated in 2011 a minimum selling price of HMF and DMF of 1.33 USD/L and 2.02 USD/L, respectively. In this calculation, which is based on published laboratory catalytic results, they identified as the bottleneck the feedstock cost of fructose, which amounts to almost half of the total costs, as can be seen in Figure 2-5. The need for cheaper feedstock in order to decrease the overall costs of the production of HMF and consecutive products is addressed in the following subchapter.

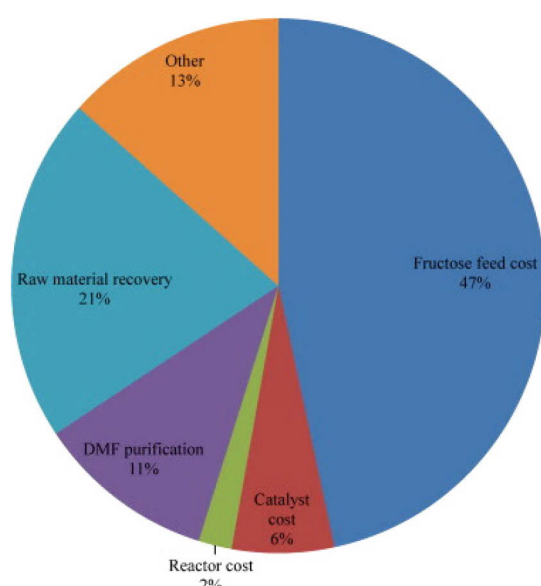


**Figure 2-5:** Major contributors to DMF price. Adapted from Kazi *et al.*<sup>45</sup>



## 2.4.2.2 Glucose as feedstock

Due to the high cost and low abundance of fructose in nature, cost-efficient and sustainable HMF production methods are needed which are based on the consumption of the isomer glucose, the most abundant monomer in nature. As proposed by Hu *et al.*<sup>30</sup>, the dehydration reaction towards HMF can occur on two pathways, illustrated in Figure 2-6: a direct acyclic pathway and the more dominant cyclic pathway, involving the isomerization to fructose on the 1,2-enediol or 1,2-hydride shift mechanism.

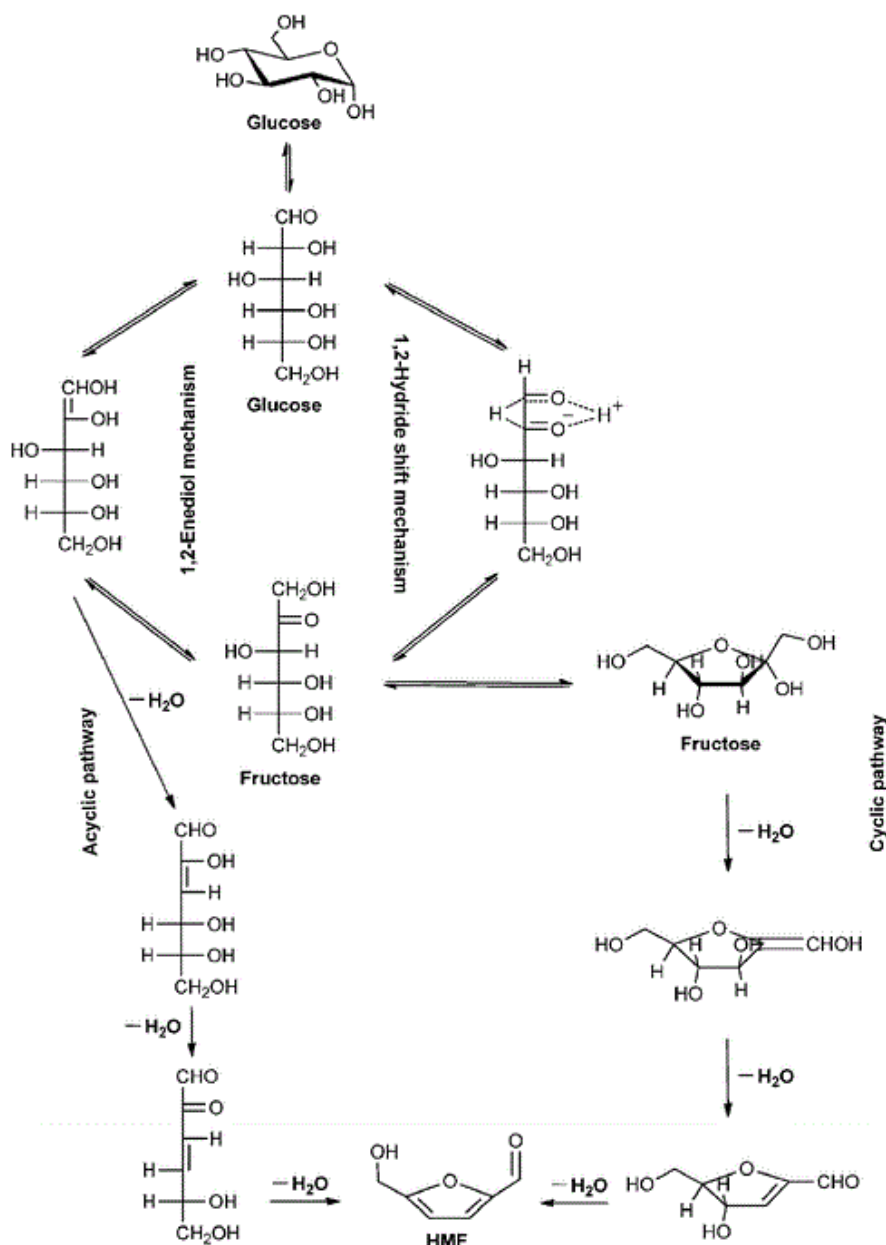


**Figure 2-6:** Proposed pathways for HMF production from fructose and glucose. Adapted from Lin *et al.*<sup>30</sup> and edited.

The implementation of an efficient glucose conversion process proves to be more difficult and challenging, compared with fructose. First of all, due to the stable pyranoside ring structure of glucose, both isomerization mechanisms proceed very slowly and, therefore, constitute the rate determining steps for the HMF production, whereas the as-formed fructose is rapidly dehydrated. Furthermore, glucose tends to form oligosaccharides with reactive reducing groups and, therefore, higher risk of cross-polymerization with reactive intermediates and HMF, while fructose only reversibly transforms in low amounts to the equilibrium species difructose and dianhydrides<sup>46</sup>. For these reasons, many catalytic systems with decent performance for the fructose dehydration are ineffective for glucose.

Similarly to the hydrolysis reaction of polysaccharides, the presence of  $\text{Cl}^-$  seems to be highly beneficial for the adsorption, solubility, and isomerization reaction of glucose, as well as for the subsequent dehydration of fructose<sup>30</sup>. Although good catalytic performance for the glucose conversion has been reported in various studies using several metal chlorides such as  $\text{AlCl}_3$ ,  $\text{CrCl}_3$ , and  $\text{SnCl}_4$ <sup>30</sup>, which act as Lewis acids, their downstream separation and recyclability is problematic. However, replacement of these liquid acids by heterogeneous catalysts still poses a big challenge to academia and industry. Since Brønsted acids such as Amberlyst-15, efficient for the fructose dehydration, exhibit very low catalytic activity for the isomerization reaction, they need to be complemented by solid Lewis acid or, alternatively, solid Lewis base catalysts<sup>30</sup>.

In view of better catalyst separation and recyclability, several types of heterogeneous catalysts have been proposed in the literature for the isomerization and dehydration of glucose. Among those are  $\text{TiO}_2$  and  $\text{ZrO}_2$  materials that do not only exhibit acidic properties, effective for the dehydration of fructose, but also basic properties, which promote the isomerization of glucose into fructose<sup>47</sup>. Qi *et al.*<sup>44</sup> reported high activity for the microwave-assisted acid-catalyzed dehydration of glucose over anatase ( $\text{TiO}_2$ ) at 200 °C, reaching yields of 17.4% for fructose and 7.7% for HMF with a total glucose conversion of 41.6%. Under the same conditions,  $\text{ZrO}_2$  exhibited lower activity for the acid-catalyzed dehydration of fructose, but higher activity for the base-catalyzed isomerization of glucose, providing yields of 25.5% for fructose and 4.6% for HMF with a total conversion of 48.4%<sup>44</sup>. The HMF yield could be greatly increased by changing the solvent to a 50:50 water/[HMIM]Cl mixture, obtaining a 53% HMF yield and 4% fructose yield with glucose conversion of 92%<sup>48</sup>. Using mesoporous  $\text{TiO}_2$  nanoparticles in a microwave-assisted process, Dutta *et al.*<sup>49</sup> obtained HMF in a yield of 24.8% in water at 120 °C, which was only slightly enhanced to 25.9% by temperature increase to 130 °C and change of solvent to water/ methyl isobutyl ketone. Although the use of hazardous solvents is not desirable for sustainable

biorefinery processes<sup>50</sup>, the use of *N*-methyl-2-pyrrolidone and dimethyl sulfoxide at 140 °C provided increased HMF yields of 29.6 and 37.2%, respectively<sup>49</sup>. Aiming at increasing the acidity of the catalyst by sulfonation, Zhang *et al.*<sup>51</sup> prepared a SO<sub>4</sub><sup>2-</sup>/ZrO<sub>2</sub>-TiO<sub>2</sub> catalyst, which yielded up to 26.0% HMF with a total glucose conversion of 96.5% at 170 °C.

Furthermore, hydrotalcites have been reported to catalyze the glucose isomerization due to their basic sites. In combination with Amberlyst-15, an HMF yield of 42.3% was obtained in dimethylformamide at 80 and 100 °C, respectively<sup>52,53</sup>. However, the use of toxic solvents such as dimethylformamide should be avoided for the sake of sustainability<sup>50</sup> and water does not seem to be an option due to considerable leaching of the hydrotalcite, which was observed in the presence of water<sup>54</sup>.

On the other hand, Sn-containing  $\beta$ -zeolites appear to be stable under hydrothermal conditions and provided up to 32% fructose yield with 9% mannose and a total glucose conversion of 55% at 110 °C in water, as reported by Moliner *et al.*<sup>55</sup>. The performance could even be strongly enhanced by Gallo *et al.*<sup>54</sup>, using a bicatalytic system of Sn- $\beta$  with a molar ratio of Si:Sn = 400 and the solid Brønsted acid Amberlyst-70. At 130 °C, they obtained up to 63% HMF yield with 90% of glucose conversion in tetrahydrofuran-water (9:1), with similar results for GVL-water (9:1) and methyltetrahydrofuran-tetrahydrofuran-water (4.5:4.5:1)<sup>54</sup>. Replacing Sn- $\beta$  by Sn-SBA-15 with a molar ratio of Si:Sn = 40 provided 46% HMF yield with 90% glucose conversion in GVL, while the exclusive use of Brønsted acid Amberlyst-70 without Sn-doped catalyst delivered 29% HMF yield with 92% glucose conversion in GVL<sup>54</sup>.

## 2.5 Hydrogenation over Metal-based Catalysts

### 2.5.1 Production of 2,5-Dimethylfuran from 5-Hydroxymethylfurfural

HMF is a versatile platform molecule that can be upgraded towards numerous chemicals and materials<sup>30</sup>. One of the major conversion routes involves the selective hydrogenation to form 2,5-dimethylfuran (DMF), as shown on the right side of the simplified reaction scheme in Figure 2-7.

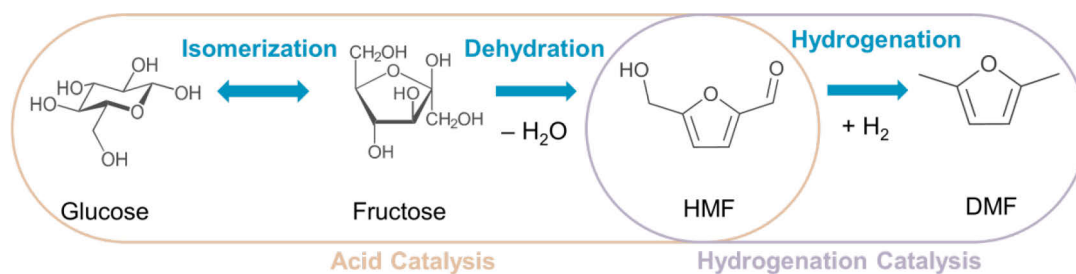


**Figure 2-7:** Simplified reaction scheme of hexose conversion towards DMF

Supported noble transition metals including Ru, Pt, and Pd have been proposed in the literature as highly active metal species that facilitate the hydrodeoxygenation of the formylmethyl and the hydroxymethyl group towards methyl groups without attacking the structure of the aromatic ring<sup>56–58</sup>. As a cheaper alternative, more abundant transition metals such as Cu and Ni have also successfully been employed<sup>56,59</sup>. A main challenge remains establishing a transition towards cost-efficient and sustainable large-scale processes. Regarding the costly purification of the intermediate HMF from the product of the acid-catalyzed sugar dehydration, it is desirable to hydrogenate the synthesized HMF without an intermediate purification step. A pioneering work for the selective production of DMF from HMF and fructose was published by Román-Leshkov *et al.*<sup>24</sup>, who prepared and tested a bimetallic Cu-Ru/C catalyst in *n*-butanol at 220 °C and 6.8 bar of  $\text{H}_2$ , obtaining yields of 71% DMF and 16% other furanic molecules. According to their hypothesis, this catalyst combined the selective hydrogenolysis behavior of Cu (rather than the preferential saturation of the double bonds exhibited by Ru) with the chloride-resistance of Ru<sup>24</sup>. As NaCl can contribute both to the conversion of carbohydrates as well as to the extraction of as-formed HMF from the aqueous into the organic phase, when applying a biphasic solvent system such as water/*n*-butanol, Román-Leshkov *et al.*<sup>24</sup> were testing the stability of their Cu-Ru/C catalyst in the presence of NaCl. The HMF hydrogenolysis activity dropped only slightly in the presence of 1.6 mM NaCl, providing yields of 61% DMF and 24% other furanic molecules, which hints at high chloride-resistance of the Cu-Ru/C catalyst and, therefore, compatibility with a preceding  $\text{Cl}^-$  promoted sugar dehydration step<sup>24</sup>. In an integrated process involving the acid-catalyzed conversion of corn stover to intermediate HMF in ionic liquids, similar DMF yields referring to intermediate HMF were obtained for the same catalyst at the same temperature and pressure, but resulting in overall DMF yields of only 9% referring to the cellulose feedstock, which is due to incomplete and unselective saccharification and dehydration of the carbohydrates<sup>60</sup>. To compare the reactivity of noble metals, Bell and Chidambaram conducted a mechanistic study of Pd, Ru, Pt, and Rh catalysts supported on carbon<sup>59</sup>. Among the tested metal catalysts, Pd/C in [EMIN]Cl/acetonitrile at 120 °C and 60 bar of  $\text{H}_2$  provided the highest activity

for the hydrodeoxygenation of HMF, reaching 47% of HMF conversion with yields of 16% DMF, 21% to furanic hydrogenation intermediates and – surprisingly – only 2.4% to tetrahydrofuranic compounds<sup>59</sup>, which is in contrast to the findings of Román-Leshkov *et al.*<sup>24</sup>, who reported selective hydrogenation of the furanic double bonds over their monometallic Pd/C catalyst towards hydrogenation.

Despite the excellent performance of several noble metal-based catalysts for the hydrodeoxygenation of HMF, cheaper catalytic materials based on more abundant sources are needed to pave the way for a cost-efficient DMF production. Among abundant non-noble metals, Ni provides decent hydrogenation reactivity. To combine high reactivity of Ni for the hydrogenation steps with an increased reactivity for the deoxygenation step, Huang *et al.*<sup>56</sup> proposed the use of Ni-based bifunctional catalysts with another metal that exhibits Lewis acid sites, promoting the deoxygenation of the hydroxy groups. In their work on several nickel-tungsten carbide based catalysts on carbon supports, Huang *et al.*<sup>56</sup> obtained DMF yield of up to 96% over a carbon-supported 7wt%Ni-30wt%W<sub>2</sub>C catalyst at 180 °C and 40 bar of H<sub>2</sub><sup>56</sup>. Hereupon, Braun and Antonietti<sup>61</sup> proposed an integrated continuous flow process with two serial packed-bed reactors for the acid-catalyzed dehydration of fructose, using Amberlyst-15, and the subsequent hydrodeoxygenation of HMF, using a 10wt% Ni/WC catalyst. At 30 bar of H<sub>2</sub> with ethanol as the solvent and operation of the acid-catalyzed reactor at 110 °C and the metal-catalyzed reactor at 150 °C, they obtained 38.5% DMF yield and 47.0% yield for ethyl levulinate, the ethanol ester of LA, which is readily formed at elevated temperature in the presence of ethanol<sup>61</sup>. As mentioned in section 2.4.2.1, LA is the consecutive acid-catalyzed product of HMF. Both LA and its ester ethyl levulinate are also valuable molecules which offer a parallel reaction branch for the valorization of hexoses towards value-added chemicals.

### 2.5.2 Production of $\gamma$ -Valerolactone from Levulinic Acid

As mentioned in section 1.1, LA is regarded by the U.S. Department of Energy as one of twelve top value-added bioderived chemicals that are essential building blocks, which allow for the conversion towards numerous high-value products, owing to their multiple functional groups<sup>5</sup>. One of the most important pathways involves the hydrogenation of LA towards  $\gamma$ -valerolactone (GVL), which requires the use of a hydrogen source such as external molecular hydrogen or other chemical hydrogen donors mentioned in section 2.5.2.2. In analogy to the hydrogenation of HMF presented in the previous subchapter, the reaction relies on the use of transition metals, such as Ru and Pt<sup>62,63</sup>.

The formation of GVL from LA can proceed *via* two parallel pathways. On the first pathway, LA is dehydrated to angelica lactone in  $\alpha$ -position, which can undergo isomerization to  $\beta$ -position<sup>64</sup>. Both isomers possess a double bond that can be further saturated towards GVL. This pathway of primary dehydration of LA is promoted by acid functionalities and usually entails coke formation and, therefore, can decrease product yields and accelerate catalyst deactivation<sup>65</sup>. The second pathway includes hydrogenation of levulinic acid towards  $\gamma$ -hydroxyvaleric acid (GHVA), an unstable intermediate that is instantly dehydrated to GVL over the acid sites<sup>64</sup>. In alcohols as solvents, the unreacted LA undergoes esterification at high temperatures. The resulting levulinic esters, such as ethyl levulinate, undergo hydrogenation towards hydroxylevulinic esters, followed by intramolecular transesterification and ring closing, eventually also forming GVL and releasing the solvent molecule. The suggested pathways are summarized in Figure 2-8.

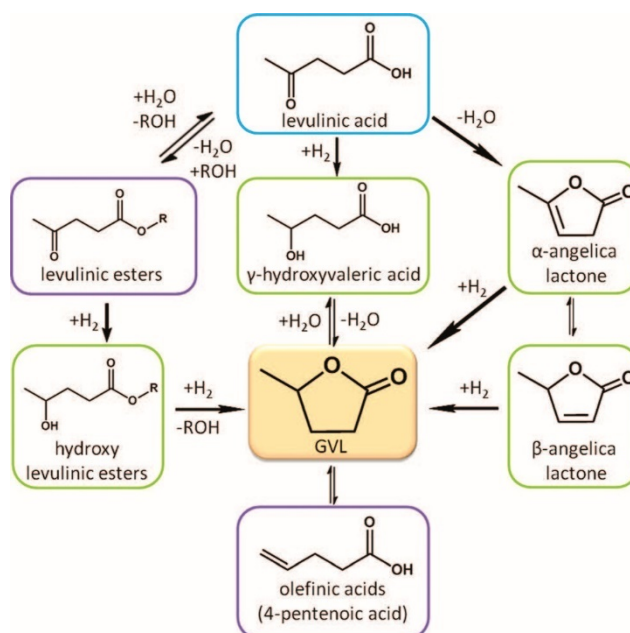


**Figure 2-8:** Reaction pathways for the production of GVL from LA, adapted from Alonso *et al.*<sup>64</sup>

### 2.5.2.1 External molecular hydrogen

In the literature, the platinum group metals Ru, Pd, and Pt are reported to exhibit excellent catalytic performance in terms of activity, selectivity, and stability, which explains why GVL production still strongly relies on the noble metal catalysis<sup>62,63</sup>.

Due to the high costs of such noble metals, efforts have been stepped up to decrease the necessary amount of active metal by increasing the catalytic activity in the LA hydrogenation, *e.g.* by employing bifunctional catalysts with additional acid sites. Acid sites on the catalyst can be obtained either by using an acidic support material or by functionalizing the support with acidic

moieties<sup>66,67</sup>. Sudhakar *et al.*<sup>68</sup> suggested the use of porous acidic hydroxyapatite as support with Pt, Pd, Ru, Ni, and Cu for the hydrogenation of LA, reaching up to 94% of LA conversion and 80% of GVL selectivity for the Ru-based catalyst at very high temperatures of up to 425 °C. Christian *et al.*<sup>69</sup> have proposed the use of Raney nickel for the hydrogenation of LA, obtaining a GVL yield of 94% for solvent-free LA hydrogenation.

In recent years, research has been intensified and diversified on the hydrogenation catalysis of LA. The investigated active metals Ru, Pd, Pt, Rh, Re, Ni, and Cu have been supported on various materials such as  $\gamma$ -Al<sub>2</sub>O<sub>3</sub>, SiO<sub>2</sub>, TiO<sub>2</sub>, ZrO<sub>2</sub>, zeolites, porous carbon, and composite materials<sup>66</sup>. In the work of Manzer<sup>63</sup>, 90% of LA conversion with a selectivity of 80% towards GVL have been obtained, using a Ru/C catalyst with 5.0wt% Ru loading at 150 °C and 55 bar of H<sub>2</sub>. Also using a Ru/C catalyst with 5.0wt% Ru, Yan *et al.*<sup>70</sup> obtained 90% of LA conversion and 86% GVL selectivity at 130 °C and 12 bar of H<sub>2</sub>, while all other tested catalysts 5.0wt% Pd/C, Raney nickel, and Urushibara nickel, exhibited surprisingly low activity with GVL yields of  $\leq 6\%$ <sup>70</sup>. To examine the influence of the catalyst support on the catalytic performance, several catalysts with 5.0wt% Ru have been tested by Al-Shaal *et al.*<sup>71</sup>, using TiO<sub>2</sub>, C, Al<sub>2</sub>O<sub>3</sub>, and SiO<sub>2</sub> as supports at the same process conditions (ethanol/water solution, 130 °C, 12 bar of H<sub>2</sub>). The highest GVL yield (89%) was reached using carbon as support, followed by Al<sub>2</sub>O<sub>3</sub> and SiO<sub>2</sub> with 76% and 75%, respectively. In a similar manner, Luo *et al.*<sup>39</sup> investigated the influence of several acid functionalities of the support by comparing 1.0wt% Ru catalysts supported on Nb<sub>2</sub>O<sub>5</sub>, TiO<sub>2</sub>, H- $\beta$ , and H-ZSM-5 in the solvents dioxane, 2-ethylhexanoic acid, and pure LA. They obtained the highest GVL yield of 97.5% for the 1.0wt% Ru/TiO<sub>2</sub> catalyst (200 °C, 40 bar), compared with the support materials Al<sub>2</sub>O<sub>3</sub> and SiO<sub>2</sub>. The above mentioned 5.0wt% Ru/TiO<sub>2</sub> catalyst by Al-Shaal *et al.*<sup>71</sup> provided catalytic activity on considerably lower level of 81% of LA conversion with 71% GVL yield, which can be attributed to the 70 K lower temperature that was used for this catalyst.

Also using Ru/TiO<sub>2</sub> catalysts in experiments combined with DFT calculations, Michel *et al.*<sup>72</sup> reported that the presence of water strongly enhances the catalytic reactivity of Ru by decreasing the activation barrier due to H-bonded water molecules. According to their prediction, this catalytic promotion can be generalized for other oxophilic metals such as Co and Ni, while the activity of Pt and Pd is expected not to be influenced by the presence of water<sup>72</sup>. The participation of water molecules in the hydrogenation reaction of LA was confirmed by Tan *et al.*<sup>73</sup>, using isotope-labeling with D<sub>2</sub>O. With a 1.0wt% Ru/TiO<sub>2</sub> catalyst in water, they obtained a 100% GVL yield at mild conditions of 70 °C and 40 bar of H<sub>2</sub><sup>73</sup>. Beside the promotion effect of water, this excellent catalytic performance is attributed to the high dispersion of Ru nanoparticles with an



average size of 2.0 nm, facilitated by the strong interaction between the metal and the TiO<sub>2</sub> support<sup>73</sup>. Even at room temperature, a surprising 100% of GVL yield was also reported by Xiao *et al.*<sup>74</sup>, who used a 2.0% Ru catalyst supported on few-layer graphene. Xiao *et al.* attribute this remarkable activity to the high metal dispersion with an average of 1.1 nm in particle size, facilitated by the strong interaction between the *dsp* states of the Ru nanoparticles with the sp<sup>2</sup> dangling bonds at the defect sites of graphene, which prevents the migration and aggregation of the nanoparticles<sup>74</sup>.

Despite the high performance of catalysts based on Ru, Pt, and Pd, the use of noble metals should be avoided in large-scale biorefinery applications. In search for alternative catalysts that are based on cheap and abundant metals, but still facilitate substantial GVL production, Hengne *et al.*<sup>75</sup> have reported the use of Cu-ZrO<sub>2</sub> and Cu-Al<sub>2</sub>O<sub>3</sub> nanocomposites in water and methanol, yielding up to 90% of GVL with 100% selectivity at 200 °C and 34 bar of H<sub>2</sub>. However, considerable catalyst deactivation by metal leaching and metal sintering has been observed for this catalyst<sup>75</sup>.

#### 2.5.2.2 Alternative hydrogen sources

The conventional production of molecular hydrogen involves either steam reforming of fossil energy carriers or water splitting<sup>76</sup>. Therefore, alternative hydrogen sources, obtained from biomass, have been proposed for hydrogenation processes in biorefinery. The use of liquid reducing reagents is simple and safe, compared with high-pressure molecular hydrogen, which is more difficult to handle safely<sup>77</sup>. Furthermore, the use of alternative hydrogen sources is reported to result in a higher atom efficiency<sup>66</sup>. Among other biobased compounds such as secondary alcohols, tetrahydroquinoline, methylpyrrolidine, and cyclohexene, particularly FA offers a great potential as a hydrogen source due to the low costs and generation as a byproduct in several biomass processing applications. This includes the preceding reaction step of HMF hydrolysis<sup>66,77</sup> towards LA, as presented in Figure 2-4.

The use of FA as a hydrogen reagent involves either *in situ* decomposition on metal sites to adsorbed hydrogen and released CO<sub>2</sub>, in which FA acts as a hydrogen precursor, or transfer hydrogenation, in which FA acts as a reducing agent. In the first case, the adsorbed hydrogen resides on the metal surface and engages in hydrogenation of LA<sup>66</sup>. In the second case, the hydroxy group of FA is adsorbed onto the catalyst surface, facilitating a transition-state bond with LA adsorbed to a neighboring metal site, followed by a hydride shift of the C-bonded H to the carbonyl-C of LA and release of the dehydrogenated FA as CO<sub>2</sub><sup>66</sup>.



Son *et al.*<sup>78</sup> examined several supported metal catalysts in water. At a molar ratio of 3:1 for FA:LA and 150 °C, the 5.0wt% Ru/C and 5.0wt% Au/ZrO<sub>2</sub> catalysts provided complete conversion of LA with a selectivity towards GVL of 90% and 97%, respectively<sup>78</sup>. In contrast, under the same reaction conditions, 5wt% Ru catalysts with different supports (C, SBA-15, Al<sub>2</sub>O<sub>3</sub>, TiO<sub>2</sub>, and ZrO<sub>2</sub>) provided considerably lower LA conversion (29%, 31%, 16%, 10%, and 11%, respectively) and GVL selectivity (73%, 71%, 17%, 20%, and 18%, respectively)<sup>78</sup>. Similarly, the activity of a 5wt% Pt/C catalyst was on a surprisingly low level, with 13% LA conversion and 13% GVL selectivity<sup>78</sup>. Braden *et al.*<sup>79</sup> observed in experiments with equimolar LA:FA ratio in water that the activity of a Ru/C monometallic catalyst for the simultaneous decomposition of FA and reduction of LA could be strongly increased by additional incorporation of Re. Over a 20wt% Cu/ZrO<sub>2</sub>, Yuan *et al.*<sup>80</sup> reported a GVL yield of 100% for combined *in situ* generation of hydrogen from FA and hydrogenation of LA at 200 °C and 10 bar of N<sub>2</sub>.

Al-Naji *et al.*<sup>81</sup> proposed a combination of noble and non-noble metals for the LA hydrogenation. Ni-Pt and Ni-Ru supported on ZrO<sub>2</sub> and  $\gamma$ -Al<sub>2</sub>O<sub>3</sub> were tested in solvent-free LA hydrogenation with FA, using a microwave batch reactor. While all tested combinations provided 100% GVL selectivity, the highest LA conversion (71%) was reached with the catalyst of 0.6wt% Ni combined with 1.9wt% Ru on  $\gamma$ -Al<sub>2</sub>O<sub>3</sub> support<sup>81</sup>. In a further work of Al-Naji *et al.*<sup>82</sup> tested a 1.6% Pt/ZrO<sub>2</sub> catalyst in aqueous solution of FA and LA in the molar ratio of 3.1:1, yielding 90% GVL with an LA conversion of 97% after 24 h of reaction at 240 °C. Increasing the reaction temperature facilitated the subsequent conversion of GVL to valeric acid, obtaining a yield of 22%, compared to the initial amount of LA. In addition, Al-Naji *et al.*<sup>83</sup> reported the use of bifunctional Pt catalysts supported on different zeolites with high density of acidic sites for the combined reaction chain of LA hydrogenation to GVL, followed by acid-promoted ring opening and subsequent hydrogenation of 2-pentenoic acid to valeric acid in aqueous solution. They found out that the ZSM-5(11) support provided the highest activity, compared with USY(30), USY(6), and Beta(12). Using a 2.0wt% Pt/ZSM-5(11) catalyst at 270 °C with a FA:LA molar ratio of 2.7:1 of the reactant solution, equilibrium of yields between valeric acid (75%) and GVL (23%) was reached and remained stable over time-on-stream. Besides the effect of acid functionality, this remarkable catalytic activity is attributed to the high metal dispersion (31%) with a very low average particle size of 0.7 nm<sup>83</sup>.



# 3

## CATALYST DESIGN AND CHARACTERIZATION

### 3.1 Synthesis of Pelletized Carbon Supports

As described in section 2.5, hydrogenation reactions of bioderived building blocks are catalyzed by certain transition metals. In order to enhance the accessible surface area of the active metal species, high dispersion of the metal on a porous catalyst support is desirable. Owing to their highly tunable morphology and pore structure, activated carbons represent a class of porous materials that are excellent candidates as supports for metal-based catalyst<sup>84,85</sup>. In addition, the carbon support can enhance the performance and stability of the active metal by electron transfer from the metal particles to the support<sup>84</sup>.

Activated porous carbon materials with high surface area are already widely used in several applications such as gas storage and filtration, energy storage, water purification, and catalysis<sup>86</sup>. Synthesis methods based on physical activation, using CO<sub>2</sub> or steam, or chemical activation, using templating agents such as ZnCl<sub>2</sub> or KOH, yield primarily microporous structures<sup>87</sup>. However, catalytic conversion of larger molecules require a hierarchical pore network, in which the presence of the larger meso- or macropores provides rapid transport to and from the active sites in the smaller pores<sup>84</sup>. In search for novel carbon materials as supports for high-performance catalysts, efforts have been stepped up in academia to synthesize porous materials with increased surface area, which, in turn, provide higher accessibility of the active sites.

As mentioned in section 1.2, the present work aims at developing catalysts suitable for large-scale industrial applications in continuous flow systems. Since catalytic advancements in industry

are usually not achieved with catalyst powders, the catalysts were synthesized in pellet shapes instead of fine powders. The latter can cause a large pressure drop  $\Delta P$  in long packed-bed reactors, whereas pellets of uniform size provide the necessary bed porosity  $\varepsilon$  for a continuous flow through the packed-bed reactor, according to the Ergun equation<sup>88</sup>:

$$\frac{\Delta P}{L_R} = 150 \cdot \frac{(1 - \varepsilon)^2}{\varepsilon^3} \cdot \frac{\eta_L u_L}{d_s^2} + 1.75 \cdot \frac{1 - \varepsilon}{\varepsilon^3} \cdot \frac{\mu_L u_L^2}{d_s^2} \quad (3.1)$$

where  $L_R$  is the length of the packed bed,  $d_s$  is the equivalent spherical diameter of the particles (see section 4.2), and  $\eta_L$  and  $\mu_L$  are the dynamic and kinematic viscosity of the liquid solution that flows through the reactor with the superficial velocity  $u_L$ .

While commercial catalyst pellets are usually prepared with expensive technical extruders, this work employs an unconventional, but cheap, simple, and highly efficient methodology, combining food technology with scientific pore templating techniques: Pasta-shaped pellets are extruded in a common pasta machine, using altered compositions of the semolina-based dough to subtly tune the structural and morphological properties of the final porous carbon supports, such as surface area, pore size distribution, and mechanical cohesion.



**Figure 3-1:** Extrusion of the carbon support precursor through pasta machine. **left:** extrusion of uncut spaghetti shape; **right:** automatic pellet cutting during extrusion by rotating cutting knife

In order to develop a synthesis strategy of carbon supports aiming at optimal structural properties for the specific catalytic applications, three different templating approaches for the preparation of extruded pellets are developed, each of them aiming at different pore size distributions. The

support materials are compared in terms of the structural and morphological characteristics as well as performance of the final catalysts. To make the precursor dough extrudable, it requires a very specific consistency within a narrow window of the right viscoelasticity, moisture, and hardness of the dough. In addition to the processability of the precursor dough, specific properties are required for the final catalyst pellets produced from the support. Therefore, to evaluate and optimize the procedure for the development of each templating method, many parameters such as composition, heat pretreatment, mixing routine, and extrusion speed, have been adjusted iteratively with simultaneous catalytic experiments of the final catalysts produced from each step of the carbon support preparation.

As a proof of concept of the versatile catalyst shaping options, the pasta doughs have been extruded into several different shapes commonly used in industrial packed-bed reactors, including hollow cylinders with grooved shell (“*penne*”), wagon wheels (“*rotelle*”), and twisted trilobes (“*fusilli*”). However, for the sake of better comparability of the different templating techniques and due to the fact that some of the shapes are too large for proper catalytic performance testing in the available medium-sized (7.8 – 28.5 mm ID) packed-bed reactors, the catalyst synthesis is focused on solid cylindrical pellets with a diameter of 3 mm (“*spaghetti*”) and 5 mm (“*bigoli*”), which upon carbonization shrink to *ca.* 2.4 and 4 mm, respectively.

### 3.1.1 Salt-melt Templating with $\text{ZnCl}_2$ Solution

A recent approach by Rothe *et al.*<sup>89</sup> for the synthesis of highly porous carbon from a liquid-viscous precursor is based on the porogenic effect of salt melts and the eutectic system of glucose-urea. This methodology yields predominantly microporous materials with very high surface area. As Rothe *et al.*<sup>89</sup> synthesized the material as large, flat chunks of undefined shape (“*cookies*”), inapt for applications in packed-bed reactors, the present work revisits the proposed route, but aims at the synthesis of extruded support pellets of uniform shape and size, suitable for the use in a packed-bed reactor. For this reason, the preparation method and composition of the precursor mixture is adjusted to obtain extrudable dough. First, a mixture of glucose and urea with a molar ratio of 1:1.5 (mass ratio of 2:1) is heated to 90 °C (above the glass transition point of 74.3 °C) and stirred for 1 h, producing a homogeneous and highly viscous liquid<sup>89</sup>. To prevent recrystallization of the urea from the mixture in the following synthesis steps, a small amount of water is added to the mixture. In a second mixture, the porogenic salt melt is prepared at 90 °C, consisting of  $\text{ZnCl}_2 \cdot 1 \text{ H}_2\text{O}$ , together with additional urea to reach urea concentrations above the eutectic point, as described by Rothe *et al.*<sup>89</sup>. After mixing the two highly viscous mixtures together, glucose and microcrystalline cellulose powder (20  $\mu\text{m}$ ) are employed as the carbon

sources and stirred into the dough. In addition, the cellulose acts as filler which lends mechanical cohesion to the extruded pellet shape. Although this dough exhibits the right viscosity to be pressed through the extrusion screw, its elasticity is not high enough to retain its shape after extrusion and be sliced by the automatic cutting knife. Therefore, additional gluten is added to the dough to mimic the consistency of common pasta dough based on durum semolina, which is very rich in gluten and, thus, provides the typical viscoelastic consistency necessary for the extrusion step of pasta dough. The optimum composition of the precursor dough is found to be based on a 1:1.1 weight ratio of the porogenic agent  $\text{ZnCl}_2$  to the main carbon sources glucose and cellulose, as shown in Table 3-1.

**Table 3-1:** Composition of precursor dough for the  $\text{ZnCl}_2$  approach. MC: microcrystalline

	Component	Weight fraction	Weight (abs.)
<b>Mixture 1</b>	Glucose	16.4 wt%	200 g
	Urea	8.2 wt%	100 g
	Water	0.3 wt%	4 g
<b>Mixture 2</b>	$\text{ZnCl}_2$	32.9 wt%	400 g
	Water	4.3 wt%	53 g
	Urea	8.2 wt%	100 g
<b>Additives</b>	Cellulose (MC)	19.7 wt%	240 g
	Gluten	9.9 wt%	120 g
	<b>Total</b>	<b>100.0 wt%</b>	<b>1 217 g</b>

The extruded pellets are preheated at 100 °C overnight for drying and reactions between the monomer components of the precursor<sup>89</sup>. During this preheating phase, a complex browning process, known in food science as *Maillard* reaction, turns the viscous dough into a hardened crosslinked polymer<sup>89</sup>. The crosslinking reactions are assumed to occur mainly between the carbonyl group of glucose in the reducing form and the amino groups of urea. Afterwards, the pretreated precursor pellets were carbonized at 500 to 800 °C (2.5 K min<sup>-1</sup> heating rate; 1 h on final temperature) under  $\text{N}_2$  atmosphere. Subsequent washing in 1M HCl (2 × 30 min) and purging with water (30 min) removes the homogeneously distributed salt from the carbonized material and creates a highly microporous structure. The complete procedure of the carbon pellet synthesis on the  $\text{ZnCl}_2$  route is illustrated in the scheme of Figure 3-2.



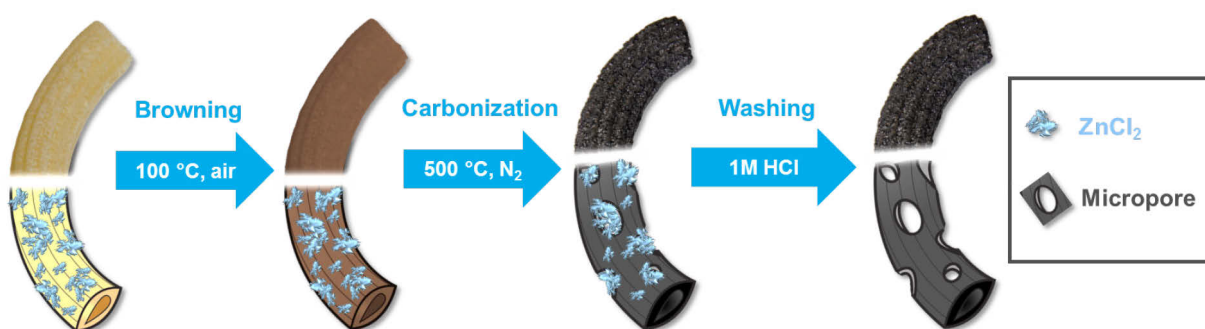


**Figure 3-2:** Scheme for the synthesis of porous carbon pellets on the  $\text{ZnCl}_2$  route

The precursor pellets in the several stages of the synthesis procedure of the carbon supports are shown in the first three pictures of Figure 3-3. The appearance of the final support is remarkably similar to the commercial  $\text{Ni/C-Al}_2\text{O}_3$  catalyst on the very right of Figure 3-3.



**Figure 3-3:** Precursor pellets of the carbon support prepared on the  $\text{ZnCl}_2$ –urea–glucose route after extrusion (**left**), after preheating at 100 °C (**second from left**), and final carbon support pellets after carbonization and washing (**third from left**), compared with commercial  $\text{Ni/C-Al}_2\text{O}_3$  catalyst extrudates (**right**)

From inductively coupled plasma (ICP) measurement, it can be seen that the applied washing procedure of the carbonized pellets considerably decreases the Zn content in the material, but is not capable of removing the Zn residue completely, as shown in Table 3-2. This is attributed to limited accessibility due to intercalation of Zn species within the carbon structure. Owing to the high amount of urea in the precursor mixture, high N-doping with a weight fraction of 13.0wt% is obtained on this route, as measured by combustion elemental analysis of the material after washing. The high N content in the carbon is expected to further increase the overall electron density at the Fermi level<sup>90</sup>, providing improved electronic conductivity and oxidation resistance, which can be beneficial for both catalytic activity and stability of the active metal.

**Table 3-2:** Elemental composition of pellets prepared on the  $\text{ZnCl}_2$  route, before ( $\text{C}_{\text{ZnCl-500}}$ ) and after ( $\text{C}_{\text{ZnCl-500L}}$ ) washing. *a*: measured by combustion elemental analysis; *b*: measured by inductively coupled plasma (ICP)

Sample	Procedure	Weight fraction [wt%]			
		C <sup>a</sup>	N <sup>a</sup>	H <sup>a</sup>	Zn <sup>b</sup>
$\text{C}_{\text{ZnCl-500}}$	Carbonized (500 °C)	48.1 ±2	8.3 ±1	2.6 ±1	24.0 ±2
$\text{C}_{\text{ZnCl-500L}}$	Carbonized (500 °C) + washed (HCl)	60.3 ±2	13.0 ±1	3.9 ±2	2.8 ±0.2

The porosity of the washed sample is investigated by nitrogen physisorption. The resulting isotherm, as well as the pore size distribution determined from the adsorption branch by the QSDFT model, is displayed in Figure 3-4.

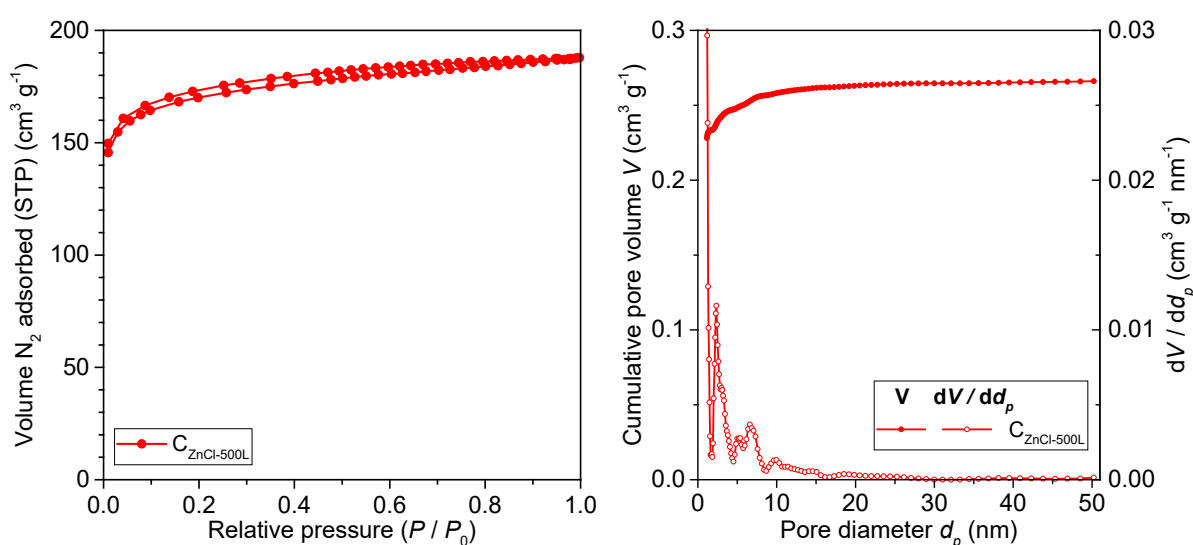


**Figure 3-4:**  $\text{N}_2$  physisorption isotherms (**left**) and pore size distribution (**right**) of carbon support pellets ( $2.4 \times 3.5$  mm) prepared on the  $\text{ZnCl}_2$  route after washing. Measurement conducted at 77.3 K. Calculation of pore size distribution based on QSDFT adsorption method on carbon with slit, cylindrical, and spherical pores.

The isotherm exhibits a typical Type I trend, according to the IUPAC classification of isotherms, with nearly complete pore filling at low relative pressure, which indicates adsorption on micropores<sup>91</sup>. The low slope of the adsorption and the desorption branch, together with minor hysteresis behavior in the medium pressure range, hints at a narrow pore network with a low contribution of small mesopores to the total pore volume ( $0.03 \text{ cm}^3/\text{g}$  of mesoporous volume, as compared to a total volume of  $0.27 \text{ cm}^3/\text{g}$ , according to QSDFT analysis). As can be seen from the pore size distribution in Figure 3-4 (right), practically no pores larger than 8 nm are present. The complete results of micro- and mesoporous volume, surface area, and average pore diameter, determined by the QSDFT, BET, and BJH methods, are summarized in Table 3-3.



**Table 3-3:** Nitrogen physisorption data of carbon support pellets ( $2.4 \times 3.5$  mm) prepared on the  $\text{ZnCl}_2$  route after washing.

Sample	Pore volume [ $\text{cm}^3/\text{g}$ ]				Specific surface area [ $\text{m}^2/\text{g}$ ]				Average pore size [nm]
	QSDFT adsorption			BJH ads.	QSDFT adsorption			BET	
	Micro	Meso	Total	Total	Micro	Meso	Total	Total	
	< 2 nm	2-50nm	$\leq 50\text{nm}$	$\lesssim 500\text{nm}$	< 2 nm	2-50nm	$\leq 50\text{nm}$		
$\text{C}_{\text{ZnCl-500L}}$	0.23	0.03	0.27	0.29	594	29	623	663	1.8

### 3.1.2 Hard Templating with NaCl Crystals

To complement the inherent microporosity of the carbonized material by additional large pores, NaCl powder, sieved to a particle size of  $< 250 \mu\text{m}$ , is employed as a hard templating agent in this section. As the carbon source, durum semolina was used, a coarse-grained durum wheat flour, which is the standard material for Italian pasta extrusion because it offers excellent extrusion properties due to the high content of gluten of  $>13\text{wt}\%$ , acting as a glue which lends viscoelasticity to the precursor dough. The optimum weight ratio of porogen to carbon source, that provides high surface area while retaining most of the cohesion in the final support material, was found to be 8:3, as shown in Table 3-4.

**Table 3-4:** Composition of precursor dough for the NaCl approach with a weight ratio of 8:3 for NaCl:semolina

Ingredient	Weight fraction	Weight (abs.)
Durum semolina	24.9 wt%	360 g
NaCl	66.4 wt%	960 g
Water	8.7 wt%	125 g
<b>Total</b>	<b>100.0 wt%</b>	<b>1 445 g</b>

After extrusion and drying overnight, the precursor pellets were carbonized at  $500^\circ\text{C}$  ( $3 \text{ K min}^{-1}$  heating rate; 1 h at  $500^\circ\text{C}$ ) under  $\text{N}_2$  atmosphere. Subsequent washing in 1M HCl ( $2 \times 30$  min) and purging with water (30 min) removes the salt crystals from the carbonized material, leaving behind large macropores to micron-sized voids.



**Figure 3-5:** Scheme for the synthesis of porous carbon pellets on the NaCl route

ICP measurement proves that the washing step removes the salt crystals almost completely, leaving behind only 0.2wt% of Na. The elemental composition of the pellets before and after washing is summarized in Table 3-5.

**Table 3-5:** Elemental composition of pellets prepared on the NaCl route, before ( $C_{\text{NaCl-500}}$ ) and after ( $C_{\text{NaCl-500L}}$ ) washing. *a*: measured by combustion elemental analysis; *b*: measured by IR elemental oxygen analysis; *c*: measured by inductively coupled plasma (ICP)

Sample	Procedure	Weight fraction [wt%]			
		C <sup>a</sup>	N <sup>a</sup>	H <sup>a</sup>	Na <sup>c</sup>
$C_{\text{NaCl-500}}$	Carbonized (500 °C)	49.3 ±2	3.5 ±0.5	2.9 ±1	17.1 ±2
$C_{\text{NaCl-500L}}$	Carbonized (500 °C) + washed (HCl)	65.3 ±2	4.1 ±0.5	3.3 ±1	0.2 ±0.1



**Figure 3-6:** Carbon precursor pellets synthesized on the NaCl route. **left:** placed in crucibles, ready for carbonization; **right:** after carbonization

The isotherm and pore size distribution (QSDFT), obtained from nitrogen physisorption measurement, is presented in Figure 3-7.

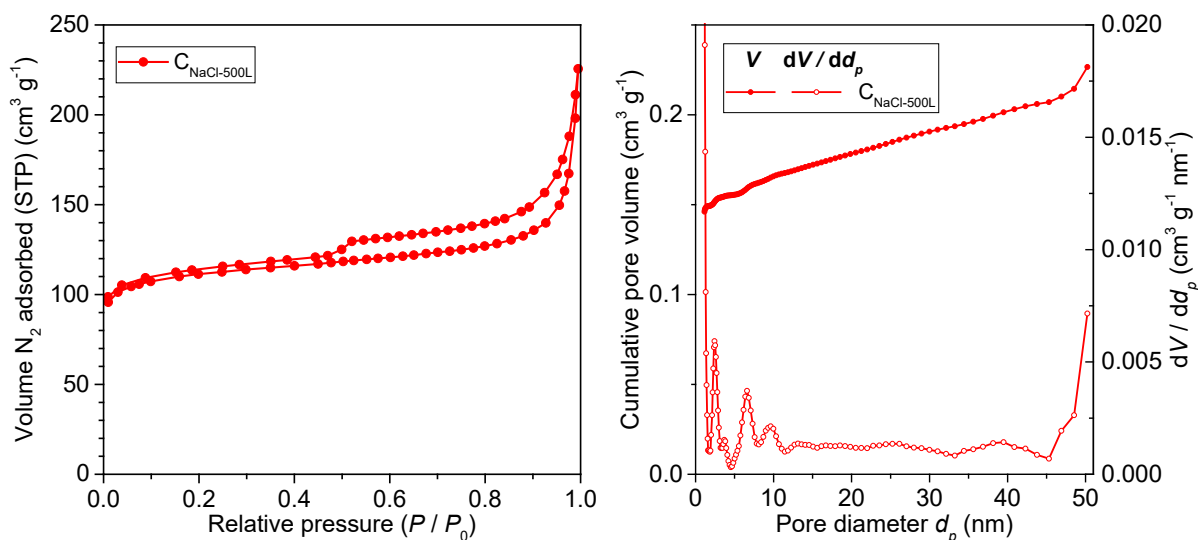


**Figure 3-7:** N<sub>2</sub> physisorption isotherms (**left**) and pore size distribution (**right**) of carbon support pellets (2.4 × 3.5 mm) prepared on the NaCl route after washing. Measurement conducted at 77.3 K. Calculation of pore size distribution based on QSDFT adsorption method on carbon with slit, cylindrical, and spherical pores.

In addition to an inherent microporous fraction of the carbon, indicated by the initial adsorption at low relative pressure, the uptake of nitrogen strongly increases at high relative pressure. Due to the absence of a saturation plateau, it can be assumed that nitrogen condenses into the large macropores. Furthermore, the delayed desorption branch is attributed to limited pore evaporation due to pore blocking or cavitation, which is likely to be caused by ink-bottle pores<sup>91</sup>. Compared with the micro- and macroporous share, the mesoporous contribution to the porosity is very low. The complete results of pore volume, surface area, and average pore diameter, determined by the QSDFT, BET, and BJH methods, are summarized for the washed sample in Table 3-6.

**Table 3-6:** Nitrogen physisorption data of carbon support pellets (2.4 × 3.5 mm) prepared on the NaCl route after washing.

Sample	Pore volume [cm <sup>3</sup> /g]				Specific surface area [m <sup>2</sup> /g]				Average pore size [nm]
	QSDFT adsorption			BJH ads.	QSDFT adsorption			BET	
	Micro	Meso	Total	Total	Micro	Meso	Total	Total	
	< 2 nm	2-50nm	≤ 50nm	≤ 500nm	< 2 nm	2-50nm	≤ 50nm		
C <sub>NaCl-500L</sub>	0.15	0.07	0.22	0.35	420	28	448	432	3.2

### 3.1.3 Hard Templating and Activation with ZnO Nanopowder

The two templating methods described in the previous subchapters either create predominantly large macropores and micron-sized voids (derived from the < 250 μm NaCl crystals) or additional microporosity (derived from the dissolved ZnCl<sub>2</sub>). To increase the diffusivity of reactants in

liquid-phase catalytic applications, a third approach is developed, which yields a larger mesopore fraction.

Mesoporous carbon is commonly synthesized *via* nanocasting with mesoporous SiO<sub>2</sub> as a hard template. This procedure entails the use of concentrated HCl for the SiO<sub>2</sub> etching process<sup>92</sup>. As a more sustainable alternative based on only cheap, abundant, and non-hazardous substances, Strubel *et al.*<sup>92</sup> proposed a templating strategy for the synthesis of hierarchically porous carbon powder from glucose, using ZnO nanopowder as the porogenic templating agent. This templating strategy, which was originally developed for energy storage applications, is customized in this work for the preparation of precursor dough that is extrudable through the pasta machine. The optimum composition of the precursor dough for the developed synthesis methodology is based on a 1:2 weight ratio of porogen to carbon source listed in Table 3-7.

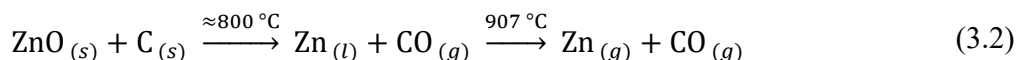
**Table 3-7:** Composition of precursor dough for the ZnO approach

<b>Ingredient</b>	<b>Weight fraction</b>	<b>Weight (abs.)</b>
Durum semolina	46.6 wt%	1 440 g
ZnO nanopowder	23.3 wt%	720 g
Urea	3.9 wt%	120 g
Glucose	3.9 wt%	120 g
Water	22.3 wt%	690 g
<b>Total</b>	<b>100.0 wt%</b>	<b>3 090 g</b>

To obtain a high viscoelasticity of the dough necessary for extrusion through the pasta machine, durum semolina is utilized as the carbon source because of its high gluten content of 13%. First, the semolina and ZnO nanopowder are mixed to create a homogeneous powder mixture. To retain the extrudability of the semolina dough, the decreased viscoelasticity of the dough, caused by the high amount of ZnO nanopowder, must be balanced. This is achieved by preparing a small amount of a highly viscous and adhesive mixture, consisting of urea, glucose, and 20% of the total water amount, which together is heated to 100 °C for 1 h. After mixing with the residual 80% water, the liquid mixture is stirred into the powder mixture at ca. 50 °C to create crumbly dough dry enough for the extrusion step.

After extrusion and drying overnight, the precursor pellets were exposed to high temperature (3 K min<sup>-1</sup> heating rate; 5 h at final temperature) under N<sub>2</sub> atmosphere, causing carbonization of the semolina and glucose, followed by carbothermal reduction of the ZnO to Zn<sup>0</sup> at ca. 800 °C<sup>92</sup>. The residual Zn can be removed from the carbon support after the heat treatment by leaching in

acidic solution. For this, the pellets are washed twice in 1M HCl solution and purged with water. Alternatively, heat treatment at 950 °C (above the boiling temperature of Zn at 907 °C) causes vaporization of the metal<sup>92</sup>.



The exact mechanisms involved in this chemical activation process are still up for debate, though it can be assumed that the carbon consumption by carbothermal reduction of ZnO at 800 °C leads to pore widening and opening, whereas the *in situ* formed liquid Zn can be intercalated between sheets of the carbon structure, leaving behind micropores upon vaporization above 907 °C.

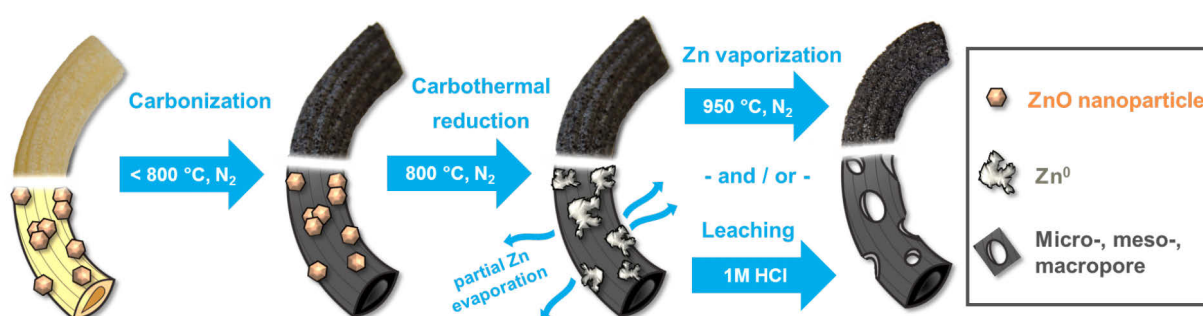


**Figure 3-8:** Scheme for the synthesis of porous carbon pellets on the ZnO route

Owing to the complete *in situ* template removal, a subsequent leaching step is not necessary, which is a unique feature, compared with other hard templating strategies. However, additional washing in HCl can still have a beneficial effect on the porosity of the material, as discussed in the following paragraph. As can be seen in Table 3-14, the major part of Zn is removed even during heat treatment at 800 °C, which leads to the conclusion that Zn slowly evaporates below the vapor pressure and diffuses through the pores. For heat treatment at an increased temperature of 950 °C, practically complete removal of Zn is obtained by vaporization, whereas washing of the pellets prepared at 800 °C did not facilitate complete removal, leaving behind 1.1wt% of Zn in the material.

**Table 3-8:** Elemental composition of pellets ( $2.4 \times 3.5$  mm) prepared on the ZnO route. *a*: measured by combustion elemental analysis; *b*: measured by elemental oxygen analysis; *c*: measured by inductively coupled plasma (ICP)

Sample	Procedure	Weight fraction [wt%]				
		C <sup>a</sup>	N <sup>a</sup>	H <sup>a</sup>	O <sup>b</sup>	Zn <sup>c</sup>
C <sub>ZnO-800</sub>	Carbonized (800 °C)	76.3 ±5	4.8 ±1	1.3 ±0.5	12.5 ±1	1.6 ±0.2
C <sub>ZnO-800L</sub>	Carb. (800 °C) + leached (HCl)	81.4 ±5	5.0 ±1	1.3 ±0.5	9.8 ±1	1.1 ±0.2
C <sub>ZnO-950</sub>	Carbonized (950 °C)	85.4 ±5	2.0 ±0.5	1.0 ±0.5	11.1 ±1	< 0.1
C <sub>ZnO-950L</sub>	Carb. (950 °C) + leached (HCl)	85.0 ±5	1.9 ±0.5	1.2 ±0.5	10.1 ±1	< 0.1

The porosity of the prepared samples is investigated by nitrogen physisorption measurements, as can be seen by the isotherms and pore size distribution diagrams of Figure 3-9. The obtained type IV isotherms exhibit hysteresis behavior between the adsorption and desorption branch due to capillary condensation in the mesopores. Furthermore, an extension of the hysteresis towards high relative pressure is observed with a late plateau, indicating complete filling of the mesopores<sup>91</sup>. This suggests the presence of additional large mesopores, which are considered beneficial for the mass transport in liquid-phase catalysis, especially within pellets in the size of several mm, as a narrow pore network without hierarchical interconnection can entail strong diffusion limitation within such large catalyst particles.

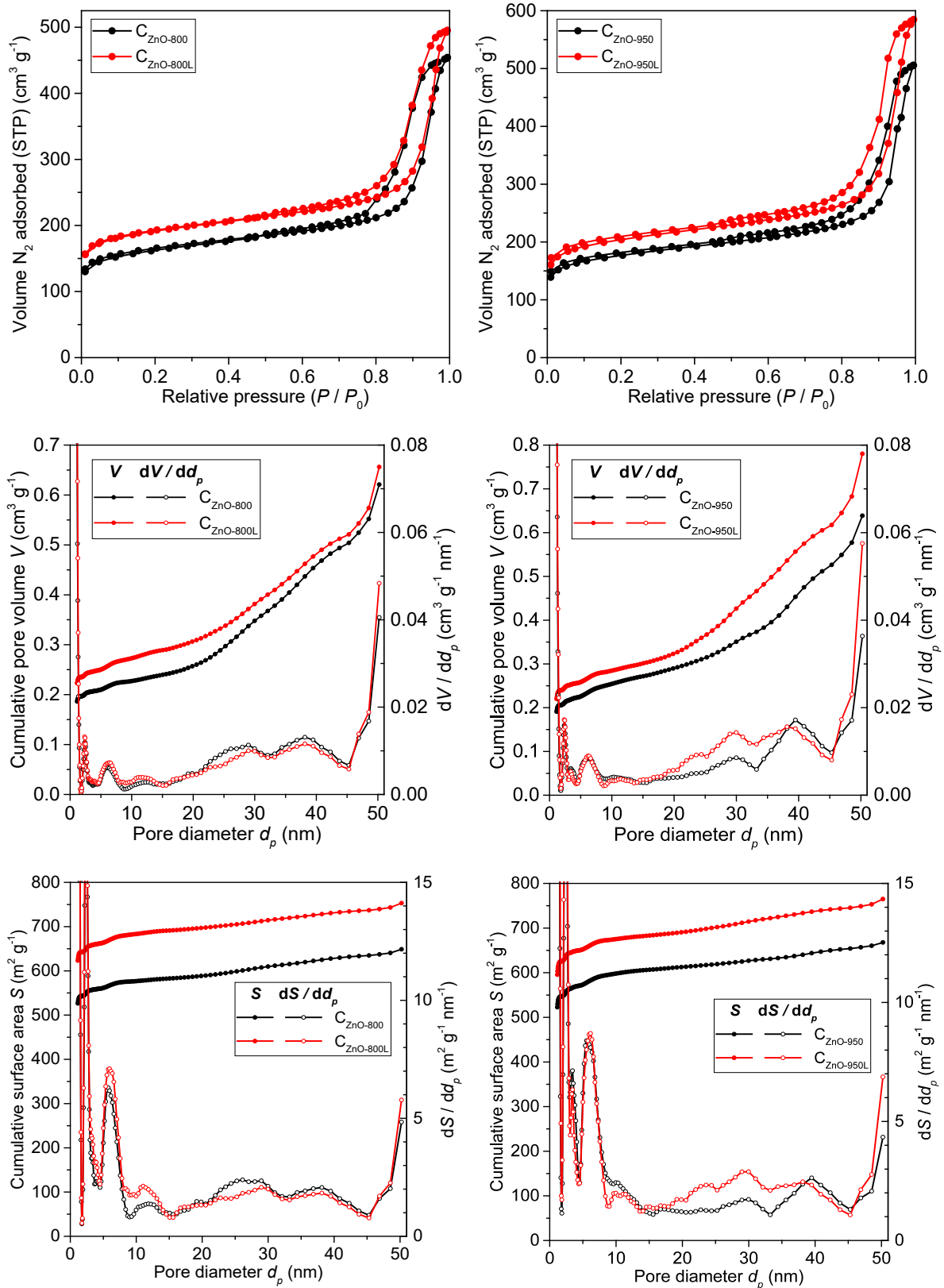


**Figure 3-9:** N<sub>2</sub> physisorption isotherms (**top**) and pore size distribution over volume (**middle**) and surface area (**bottom**) of carbon support pellets (2.4 × 3.5 mm) prepared on the ZnO route at 800 °C (**left**) and 950 °C (**right**), before and after leaching. Measurements conducted at 77.3 K. Calculation of pore size distribution based on QSDFT adsorption method on carbon with slit, cylindrical, and spherical pores.



Very large surface area is obtained for all specimens, with the  $C_{ZnO-950L}$  exhibiting the highest value of 756, calculated by QSDFT on the adsorption branch. Furthermore, all samples exhibit pore size distribution with a large fraction of mesopores between 20 and 45 nm in diameter. Above 45 nm, the cumulative pore volume is increasing progressively with increasing pore size – a trend that presumably continues through the macroporous range. In particular, the  $C_{ZnO-950L}$  pellets provide a very high contribution of mesopores ( $0.49 \text{ cm}^3/\text{g}$ ) to the total (micro- + meso-) pore volume ( $0.74 \text{ cm}^3/\text{g}$ ), which turns them into a promising support material for liquid-phase catalytic applications. The complete results of pore volume, surface area, and average pore diameter, determined by the QSDFT, BET, and BJH methods, are summarized in Table 3-9.

**Table 3-9:** Nitrogen physisorption data of carbon support pellets ( $2.4 \times 3.5 \text{ mm}$ ) prepared on the ZnO route at 800 and 950 °C, before and after leaching.

Sample	Pore volume [cm <sup>3</sup> /g]				Specific surface area [m <sup>2</sup> /g]				Average
	QSDFT adsorption			BJH ads.	QSDFT adsorption			BET	pore size
	Micro	Meso	Total	Total	Micro	Meso	Total	Total	[nm]
	< 2 nm	2-50nm	≤ 50nm	≤ 500nm	< 2 nm	2-50nm	≤ 50nm		≤ 500nm
C <sub>ZnO-800</sub>	0.20	0.39	0.59	0.70	544	99	643	627	4.5
C <sub>ZnO-800L</sub>	0.24	0.38	0.62	0.77	643	102	746	734	4.2
C <sub>ZnO-950</sub>	0.21	0.41	0.61	0.78	547	114	662	663	4.7
C <sub>ZnO-950L</sub>	0.24	0.49	0.74	0.91	627	129	756	769	4.7



**Figure 3-10:** Precursor pellets prepared on the ZnO route before and after carbonization



## 3.2 Incorporation of Metal Nanoparticles

In order to disperse the catalytically active metal nanoparticles on the surface of the porous support pellets, incipient wetness impregnation of the pellets with aqueous metal salt solutions is conducted. As the C<sub>ZnO-950L</sub> carbon pellets, presented in the previous subchapter, exhibit the best porosity-related properties of all synthesized catalyst pellets, they are used for most of the catalyst synthesis procedures presented in the following. Unless specified otherwise, “C” represents the C<sub>ZnO-950L</sub> pellets. To obtain the desired metal loading (metal weight fraction)

$$w_M = \frac{m_M}{m_{cat}} = \frac{m_M}{m_C + m_M} \quad (3.3)$$

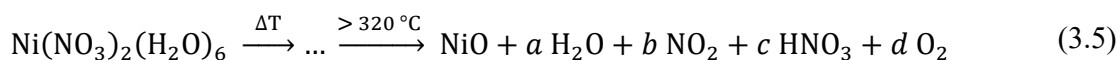
on the carbon support with the weight  $m_C$ , the weight of salt  $m_{salt}$  in the solution with a volume equivalent to the total pore volume of the support is set according to

$$m_{salt} = m_M \cdot \frac{M_{salt}}{M_M} = \frac{m_C}{1/w_M - 1} \cdot \frac{M_{salt}}{M_M} \quad (3.4)$$

with  $M_{salt}$  and  $M_M$  being the molar mass of the salt and the metal, respectively. This calculation presumes that the carbon support would not engage in chemical reactions during the nanoparticle synthesis steps, which, however, is not exactly the case, as is discussed later in this subchapter. After the solution had been drawn into the pores by capillary action, the pellets were dried at 60 °C overnight and subsequently exposed to heat treatment.

### 3.2.1 Nickel

For the synthesis of Ni nanoparticles on the surface of the porous carbon, Ni(NO<sub>3</sub>)<sub>2</sub>(H<sub>2</sub>O)<sub>6</sub> is applied as the precursor salt. According to Brockner *et al.*<sup>93</sup>, the thermal decomposition of *pure* Ni(NO<sub>3</sub>)<sub>2</sub>(H<sub>2</sub>O)<sub>6</sub> in N<sub>2</sub> atmosphere without the presence of a reducing agent proceeds via various partial decomposition steps, forming several intermediate hydroxide-oxide phases, which eventually transform into NiO at temperatures above 320 °C, accompanied by the release of gas:



To ensure complete decomposition of the salt on the carbon support, the impregnated pellets are exposed to a calcination temperature of 500 °C in N<sub>2</sub> atmosphere, which is maintained for 5 h. Finally, the pellets are reduced in a tubular oven under forming gas atmosphere (H<sub>2</sub>:N<sub>2</sub> 5:95) to obtain elemental metal nanoparticles. According to the literature, reduction of NiO is observed to start occurring at around 262 °C in 10% H<sub>2</sub> atmosphere<sup>93</sup>. To achieve complete reduction of the

NiO particles even in 5% H<sub>2</sub> atmosphere, the reduction temperature is set in the present synthesis for 5 h to 450 °C, depending on the batch. The complete procedure of Ni nanoparticle synthesis is summarized in the scheme of Figure 3-11. The respective metal loadings of the final catalysts obtained from different concentrations of the solutions, are determined by inductively coupled plasma (ICP) and listed in Table 3-10.



**Figure 3-11:** Scheme for the Ni nanoparticle incorporation on the support pellets

**Table 3-10:** Elemental composition of carbon support pellets ( $2.4 \times 3.5$  mm) prepared on the ZnO route ( $C_{ZnO-950L}$ ) and catalysts supported on the pellets with different Ni loadings (Ni/ $C_{ZnO-950L}$ , abbreviated by Ni/C). *a*: measured by combustion elemental analysis; *b*: measured by inductively coupled plasma (ICP)

Sample	Weight fraction [wt%]				
	C <sup>a</sup>	N <sup>a</sup>	H <sup>a</sup>	Zn <sup>b</sup>	Ni <sup>b</sup>
<b>C<sub>ZnO-950L</sub></b>	85.0 ±5	1.9 ±0.5	1.2 ±0.5	< 0.1	—
<b>5wt% Ni/C</b>	78.2 ±5	2.0 ±0.5	1.2 ±0.5	< 0.1	5.0 ±0.5
<b>21wt% Ni/C</b>	71.1 ±5	2.1 ±0.5	1.1 ±0.5	< 0.1	21.3 ±1
<b>29wt% Ni/C</b>	72.6 ±5	2.3 ±0.5	1.1 ±0.5	< 0.1	29.1 ±1

From the N<sub>2</sub> physisorption results presented in Figure 3-12 it can be seen that the loadings of 5wt% and 21wt% of Ni do not significantly diminish the porous properties. On the contrary, the total specific surface area even increased, according to the numbers given in Table 3-11. Considering the weight increase of the pellets by addition of Ni, it can be concluded that the absolute pore volume of the 21wt% Ni/C pellets remained on the same level or even slightly increased, compared with the support pellets. In contrast, the 29wt% specimen exhibits strongly reduced adsorption capacity, leading to the assumption that the high amount of Ni fills the pore volume to a considerable extent and possibly blocks the access to sections of the pore network.

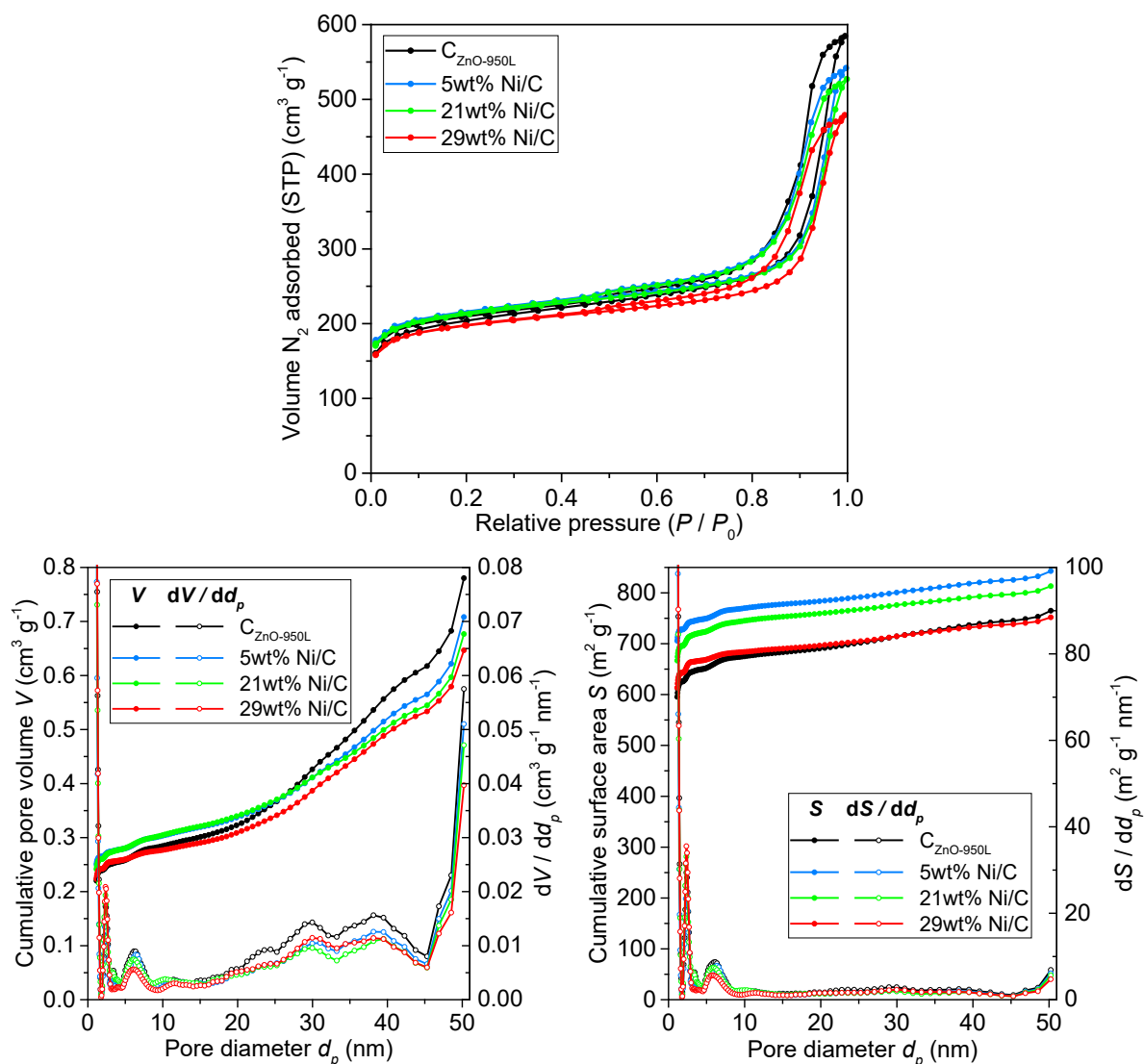


**Figure 3-12:** N<sub>2</sub> physisorption isotherms (**top**) and pore size distribution over volume (**bottom left**) and surface area (**bottom right**) of the C<sub>ZnO-950L</sub> carbon support pellets (2.4 × 3.5 mm), compared to catalyst pellets based on the C<sub>ZnO-950L</sub> support with incorporated Ni nanoparticles of different loading. Measurements conducted at 77.3 K. Calculation of pore size distribution based on QSDFT adsorption method on carbon with slit, cylindrical, and spherical pores.

**Table 3-11:** Nitrogen physisorption data of the C<sub>ZnO-950L</sub> carbon support pellets (2.4 × 3.5 mm) compared to catalyst pellets based on the C<sub>ZnO-950L</sub> support with incorporated Ni nanoparticles of different loading

Sample	Pore volume [cm <sup>3</sup> /g]				Specific surface area [m <sup>2</sup> /g]				Average pore size [nm]
	QSDFT adsorption			BJH ads.	QSDFT adsorption			BET	
	Micro	Meso	Total	Total	Micro	Meso	Total	Total	
	< 2 nm	2-50nm	≤ 50nm	≲ 500nm	< 2 nm	2-50nm	≤ 50nm	≲ 500nm	
C <sub>ZnO-950L</sub>	0.24	0.49	0.74	0.91	627	129	756	769	4.7
5wt% Ni/C	0.26	0.40	0.67	0.84	725	109	835	818	4.1
21wt% Ni/C	0.26	0.38	0.64	0.82	697	108	805	804	4.1
29wt% Ni/C	0.24	0.37	0.62	0.74	644	101	745	750	4.0

As the increase in pore volume and surface area of the 21wt% pellets occurs primarily in the microporous range, it is concluded that additional micropores are formed in the carbon structure to a large extent during the nanoparticle synthesis procedure. Such an activation process of the carbon is most likely induced by the presence of an oxidant. Here, the highly oxidative  $\text{Ni}(\text{NO}_3)_2$  as well as intermediate oxide phases such as  $\text{Ni}_2\text{O}_3$  presumably play a major part. Under the assumption that, per 1 mol of  $\text{Ni}(\text{NO}_3)_2$ , 1 mol of C engages in carbothermal reduction towards NiO, a carbon loss of 4.3wt% (relating to the total weight of the final 21wt% Ni/C catalyst) is expected, according to equation (3.5). In addition, a large part of the as-formed NiO undergoes carbothermal reduction, as can be concluded by the distinct  $\text{Ni}^0$  peaks in the XRD diffraction pattern of the 21wt% Ni/C precursor before the  $\text{H}_2$ -assisted reduction step, presented in Figure 3-13. According to the relative peak areas, it is expected that *ca.* 30% of the total NiO are transformed into metallic  $\text{Ni}^0$ , inducing another 1.2wt% of carbon loss. Therefore, a total carbon loss of 5.5wt% is observed, relating to the total weight of the final 21wt% Ni/C material, which is equivalent to a total carbon loss of 6.5wt%, relating to the total weight of the  $\text{C}_{\text{ZnO-950L}}$  precursor.

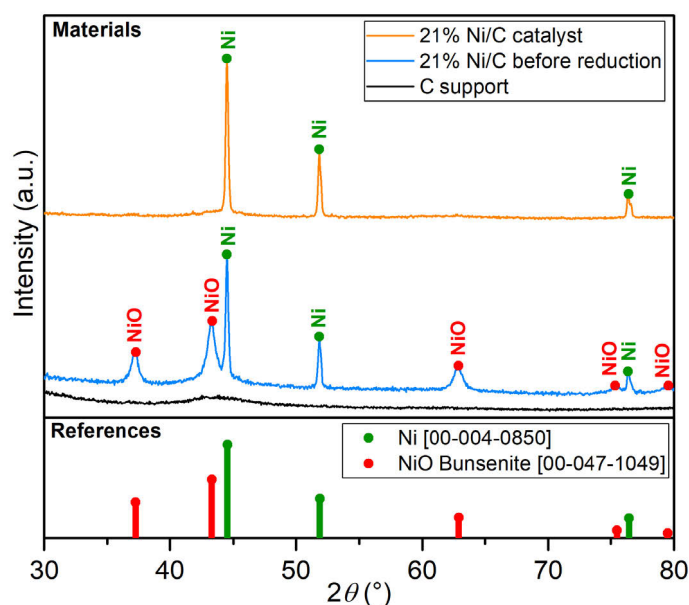


**Figure 3-13:** XRD diffractograms of the  $\text{C}_{\text{ZnO-950L}}$  carbon support, the “21wt% Ni/C” precursor before reduction, and the final 21wt% Ni/C catalyst

The mean crystallite sizes  $\bar{d}_{\text{NiO}}$  and  $\bar{d}_{\text{Ni}}$  of the 21wt% Ni/C precursor before reduction was calculated according to the Scherrer equation:

$$\bar{d} = \frac{K \lambda}{FWHM \cos(\theta)} \quad (3.6)$$

where  $K = 0.88$  is the spherical shape factor,  $\lambda = 1.54 \text{ \AA}$  is the  $K_\alpha$  wavelength of Cu produced by the X-ray source,  $\theta$  is the Bragg angle, and  $FWHM$  is the angular line broadening (“full width at half maximum”) of the peaks. The mean size was found to be 13 nm and 30 nm for the crystalline domains of NiO and  $\text{Ni}^0$ , respectively, which has been calculated by the average of the three mean crystallite sizes calculated at the peak positions  $[44.50^\circ; 51.85^\circ; 76.40^\circ]$  and  $[37.30^\circ; 43.35^\circ; 62.90^\circ]$  for  $\text{Ni}^0$  and NiO, respectively. In analogy, for the final 21wt% Ni/C catalyst (after  $\text{H}_2$ -assisted reduction), an average  $\text{Ni}^0$  crystallite size of 29 nm has been determined.

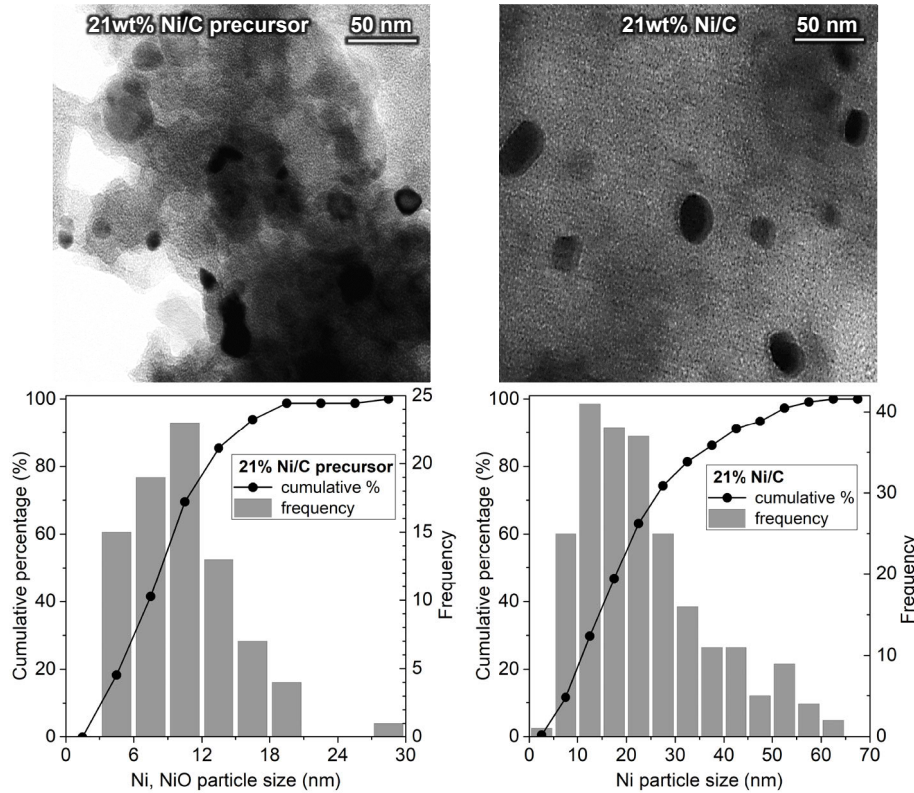


**Figure 3-14:** TEM images (**top**) and particle size distribution (**bottom**) of the 21wt% Ni/C pellets before (**left**) and after (**right**) reduction.

The size distribution of the  $\text{Ni}^0$  and NiO particles on the precursor (before  $\text{H}_2$ -assisted reduction) as well as the catalyst (after  $\text{H}_2$ -assisted reduction) is determined from a number of  $n > 100$  particles detected on several TEM images of each specimen, as shown in Figure 3-14. Since in terms of catalytic activity, the crucial geometric dimension of the active metal particles is their surface area, the mean particle size is determined based on the mean surface area. The surface-weighted (SW) mean particle size

$$\bar{d}_{sw} = \sqrt{\frac{\bar{s}_{sphere}}{\pi}} = \sqrt{\frac{\sum_{i=1}^n d_i^2}{n}} \quad (3.7)$$

of the final 21wt% Ni/C catalyst (after reduction) is calculated to 27 nm, which is close to the value of 29 nm that has been determined for the Ni<sup>0</sup> crystallites from the peak shapes in Figure 3-13. The surface-weighted mean particle size in the precursor before reduction is calculated to 11 nm, while for the crystallite size of the predominant NiO phase, a value of 13 nm was determined. Accordingly, the reduction of the NiO entails recrystallization with strong particle growth. The numbers are summarized in Table 3-12. For transformation between volume and surface area, the Sauter mean diameter (SMD) is included as well:

$$\bar{d}_{SMD} = 6 \frac{\sum V}{\sum S} = \frac{\sum_{i=1}^n d_i^3}{\sum_{i=1}^n d_i^2} \equiv \frac{\bar{d}_{VW}^3}{\bar{d}_{SW}^2} \quad (3.8)$$

**Table 3-12:** Analysis of Ni and NiO nanoparticle and crystallite size of the reduced 21wt% Ni/C catalyst and of its precursor before reduction; *a*: determined from particle size distribution on TEM images; *b*: determined as average value of three mean crystallite sizes calculated from the three main peaks in the XRD diffractogram

Sample	Mean particle size <sup>a</sup> [nm]		Crystallite size <sup>b</sup> [nm]
	Surface-weighted	Sauter	
21wt% Ni/C			
precursor (bef. red.)	11	15	13 (NiO); 30 (Ni <sup>0</sup> )
catalyst (after red.)	27	38	29 (Ni <sup>0</sup> )

As can be seen from the TEM images in Figure 3-15, the high Ni loadings of 21 and 29wt% entail metal nanoparticles of increased size, compared with the low loading of 5wt% Ni. For the 5wt% Ni/C sample, well-dispersed nanoparticles with a mean (surface-weighted) size of 12 nm are observed on the TEM images. As a large fraction of the particles is present in the low nm range (Figure 3-15 bottom left), they cannot be properly identified by XRD due to indistinctive peak broadening, which leads to a presumably overestimated mean crystallite size of 22 nm. For the 29wt% sample, most particles do not considerably change in size, as compared to the 21wt% catalyst. However, a few large insular particles of > 100 nm are observed, which account for a large part of the total Ni amount and, therefore, considerably increase the mean (surface-weighted) size to 34 nm and decrease the dispersion and active surface area. In Table 3-13, the numbers are summarized and compared to the crystallite sizes determined from XRD.



**Table 3-13:** Analysis of Ni nanoparticle and crystallite size of catalyst pellets with different Ni loadings (Ni/C<sub>ZnO-950L</sub>, abbreviated by Ni/C); *a*: determined from particle size distribution on TEM images; *b*: determined as average value of three mean crystallite sizes calculated from the three main peaks in the XRD diffractogram

Sample	Mean particle size <sup>a</sup> [nm]		Crystallite size <sup>b</sup> [nm]
	Surface-weighted	Sauter	
5wt% Ni/C	12	21	22 (Ni <sup>0</sup> )
21wt% Ni/C	27	38	29 (Ni <sup>0</sup> )
29wt% Ni/C	34	66	43 (Ni <sup>0</sup> )

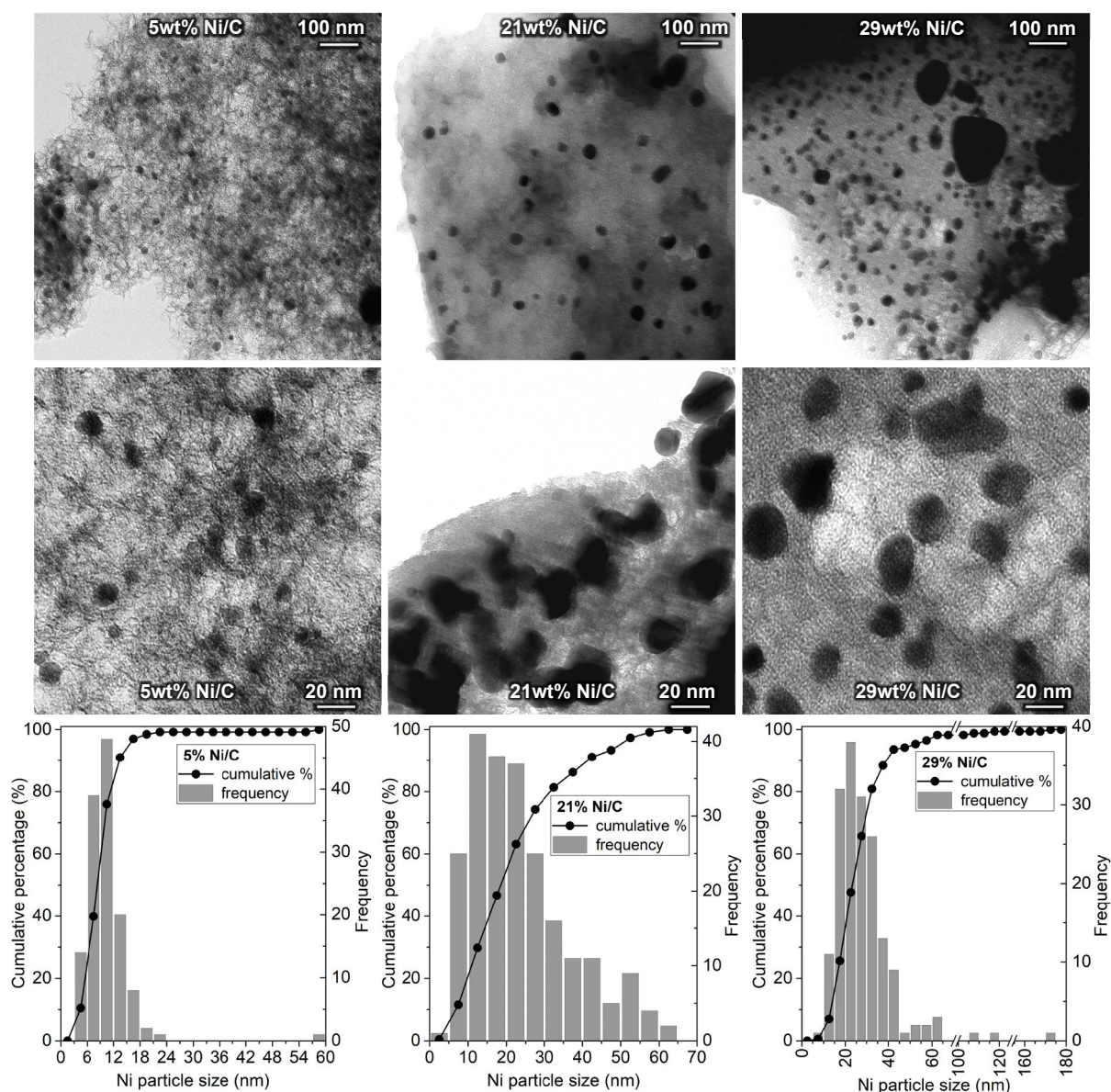


**Figure 3-15:** TEM images in low (**top**) and high (**middle**) magnification and particle size distribution (**bottom**) of the 5wt%, 21wt%, and 29wt% Ni/C catalyst.

The SEM images of the cross section of the 21% Ni/C pellets prove the homogeneous distribution of Ni nanoparticles along the inner surface of the catalyst pellets, as shown in Figure 3-16.

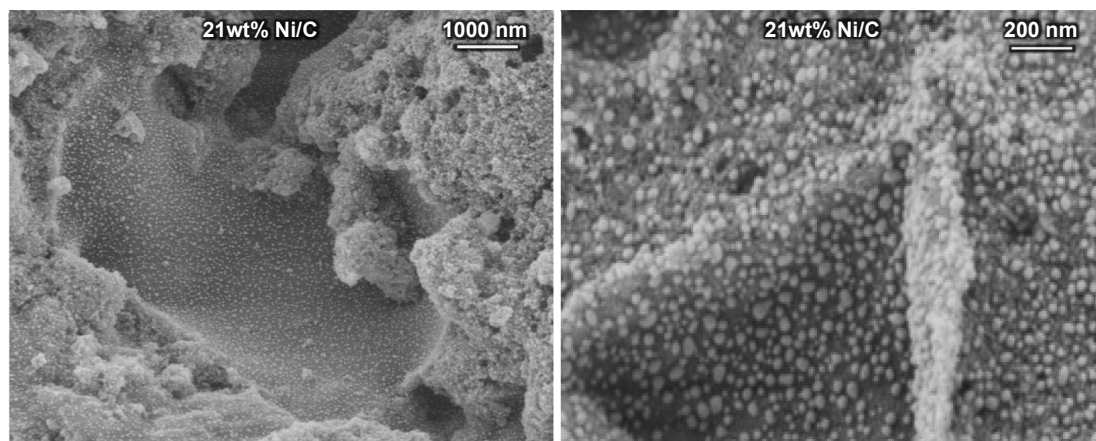


**Figure 3-16:** SEM images of the cross-section surface of the 21wt% Ni/C catalyst pellet

### 3.2.2 Platinum

Pt nanoparticles have been synthesized in an analogous manner to the presented methodology for Ni nanoparticle incorporation. The parameters of the applied heating programs are summarized in Table 3-14.

**Table 3-14:** Ni and Pt salt, used for incipient wetness impregnation, and applied heat treatment programs for metal nanoparticle synthesis on the supports. The heat treatment of each calcination and reduction step was preceded by 0:30 waiting time and 1:00 preheating at 90 °C (3 K min<sup>-1</sup>)

Metal	Metal salt	Calcination (N <sub>2</sub> )			Reduction (H <sub>2</sub> :N <sub>2</sub> 5:95)		
		Heating rate [K min <sup>-1</sup> ]	Final temp. [° C]	Hold [h:mm]	Heating rate [K min <sup>-1</sup> ]	Final temp. [° C]	Hold [h:mm]
Ni	Ni(NO <sub>3</sub> ) <sub>2</sub> (H <sub>2</sub> O) <sub>6</sub>	3	500	5:00	3	450	5:00
Pt	Pt(NH <sub>3</sub> ) <sub>4</sub> (NO <sub>3</sub> ) <sub>2</sub>	3	350	4:00	3	350	4:00

For all prepared Pt loadings (0.5, 0.8, and 2.7wt%), slightly diminished porosity is observed in N<sub>2</sub> physisorption measurements, as can be seen from the lower adsorbed N<sub>2</sub> amount and the lower cumulative pore volume in Figure 3-17. In particular, a continuous decrease of microporous volume and surface area with increasing loading is observed, according to the physisorption data provided in Table 3-15.



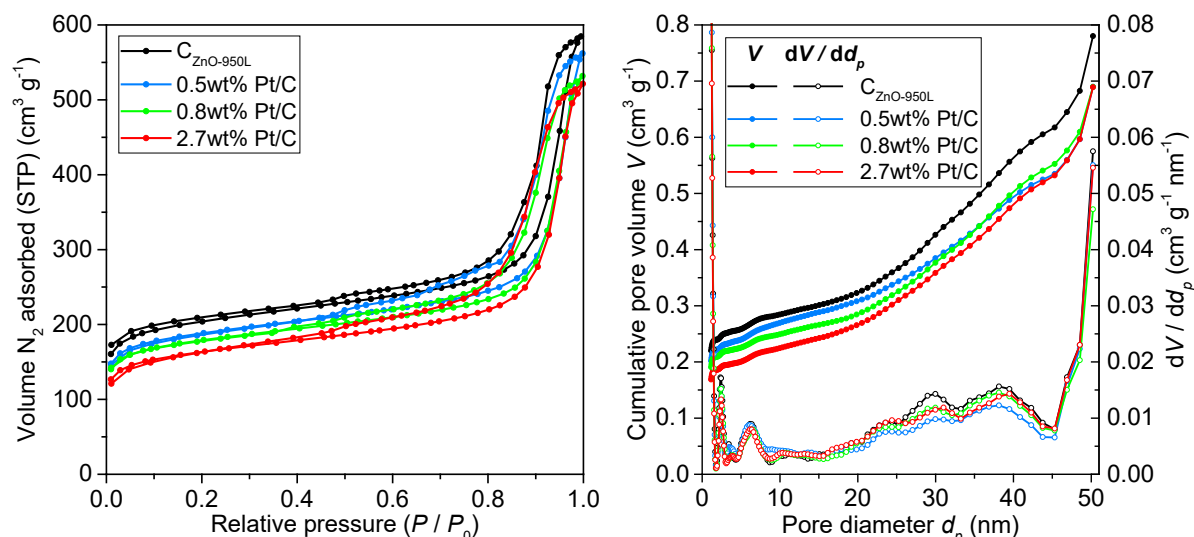


**Figure 3-17:** N<sub>2</sub> physisorption isotherms (**left**) and pore size distribution (**right**) of the C<sub>ZnO-950L</sub> carbon support pellets (2.4 × 3.5 mm), compared to catalyst pellets based on the C<sub>ZnO-950L</sub> support with incorporated Pt nanoparticles of different loading. Measurements conducted at 77.3 K. Calculation of pore size distribution based on QSDFT adsorption method on carbon with slit, cylindrical, and spherical pores.

**Table 3-15:** Nitrogen physisorption data of the C<sub>ZnO-950L</sub> carbon support pellets (2.4 × 3.5 mm) compared to catalyst pellets based on the C<sub>ZnO-950L</sub> support with incorporated Pt nanoparticles of different loading

Sample	Pore volume [cm <sup>3</sup> /g]				Specific surface area [m <sup>2</sup> /g]				Average pore size [nm]
	QSDFT adsorption			BJH ads.  Total	QSDFT adsorption			BET  Total	
	Micro	Meso	Total		Micro	Meso	Total		
	< 2 nm	2-50nm	≤ 50nm		≈ 500nm	< 2 nm	2-50nm		≤ 50nm
C <sub>ZnO-950L</sub>	0.24	0.49	0.74	0.91	627	129	756	769	4.7
0.5wt% Pt/C	0.22	0.42	0.65	0.87	594	118	711	708	4.9
0.8wt% Pt/C	0.21	0.44	0.65	0.82	557	116	673	673	4.9
2.7wt% Pt/C	0.19	0.46	0.65	0.81	492	118	610	611	5.3

**Table 3-16:** Analysis of Pt nanoparticle size distribution of catalyst pellets with different Pt loadings (Pt/C<sub>ZnO-950L</sub>, abbreviated by Pt/C), determined from particle size distribution on TEM images

Sample	Mean particle size [nm]	
	Surface-weighted	Sauter
<b>0.5wt% Pt/C</b>	4.9	7.0
<b>0.8wt% Pt/C</b>	5.2	6.8
<b>2.7wt% Pt/C</b>	4.9	8.6

From the TEM images and the particle size distribution shown in Figure 3-18, it can be seen that the procedure of all three loadings (0.5, 0.8, and 2.7wt%) yield dispersed Pt particles with a mean (surface-weighted) size of 5.2 to 5.6 nm. However, it should be noted that due to the resolution

limitation of the device, particles in the size of  $< 1$  nm remain undetected. The numbers are summarized in Table 3-16.

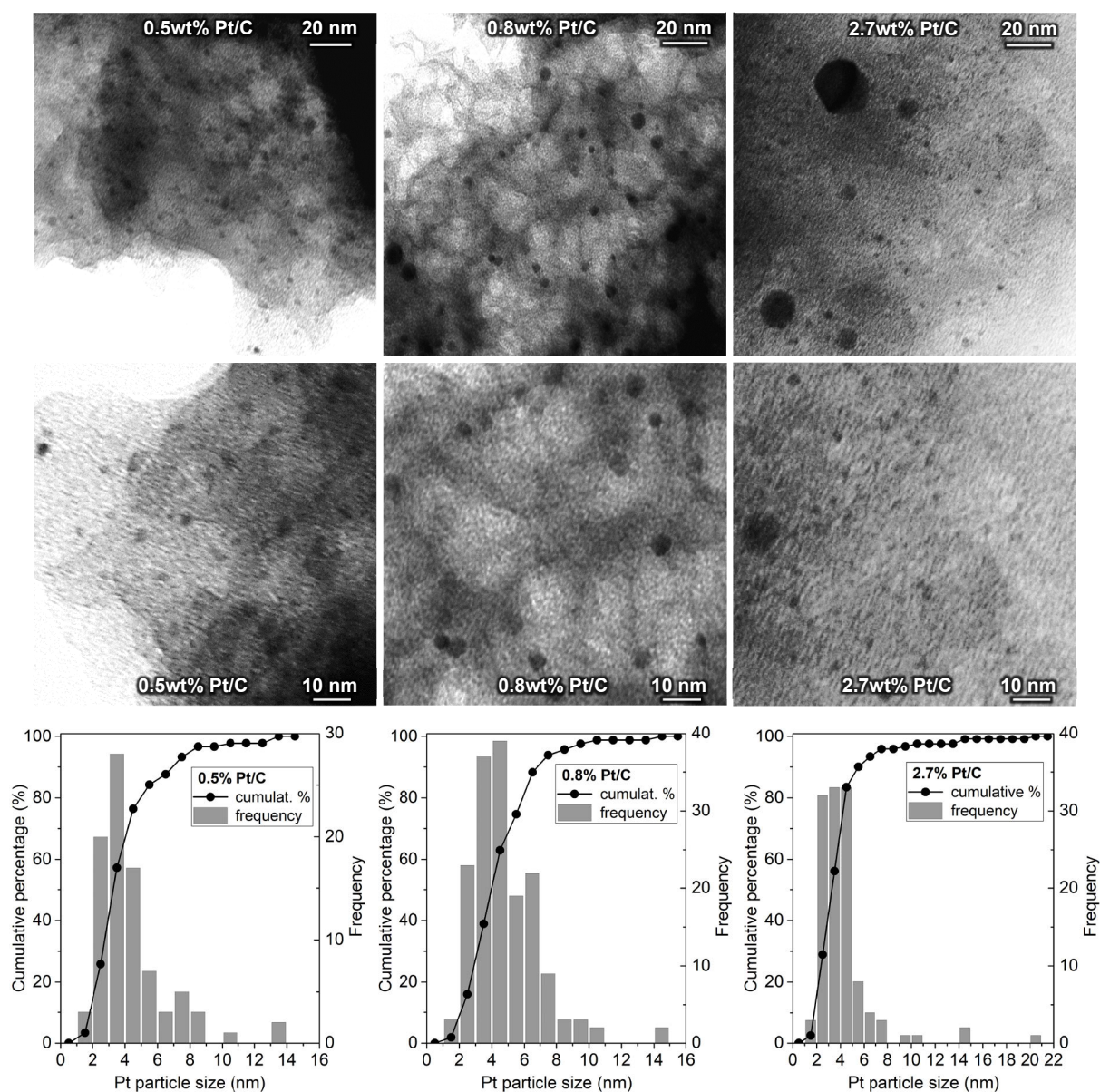


**Figure 3-18:** TEM images in low (**top**) and high (**middle**) magnification and particle size distribution (**bottom**) of the 0.5wt%, 0.8wt%, and 2.7wt% Pt/C catalyst.

### 3.3 Solid Acid Catalyst

#### 3.3.1 Characterization

##### 3.3.1.1 Surface Acidity

To investigate the surface acidity on the granular crosslinked polystyrene sulfonate (PSS) acquired from AppliChrom, Böhm titration was performed. In this back titration technique, the

density of acidic sites is indirectly determined by measuring the basicity of the analyte solution that contains an excess of base<sup>95,96</sup>. Due to the strong dilute base (NaOH), this technique is able to determine the total amount of acid sites, including those of weak acidity. The density of acid sites is calculated to a value of  $3.22 \text{ eq kg}^{-1}$ . The exact procedure and calculation is provided in Appendix A.2.2.8.

### 3.3.1.2 Porosity

To examine the porosity of the polystyrene sulfonate material,  $\text{N}_2$  physisorption has been conducted. However, due to the high density of sulfo groups, the sulfonated polystyrene does not allow for proper  $\text{N}_2$  physisorption results. Therefore, the neutral form of the crosslinked polystyrene granules (PS) has been investigated before the sulfonation step instead. As can be seen from the isotherm and pore size distribution (QSDFT adsorption) in Figure 3-19, it exhibits a very large mesoporous fraction, which facilitates a very large total pore volume of  $0.90 \text{ cm}^3/\text{g}$ , as summarized in Table 3-17.

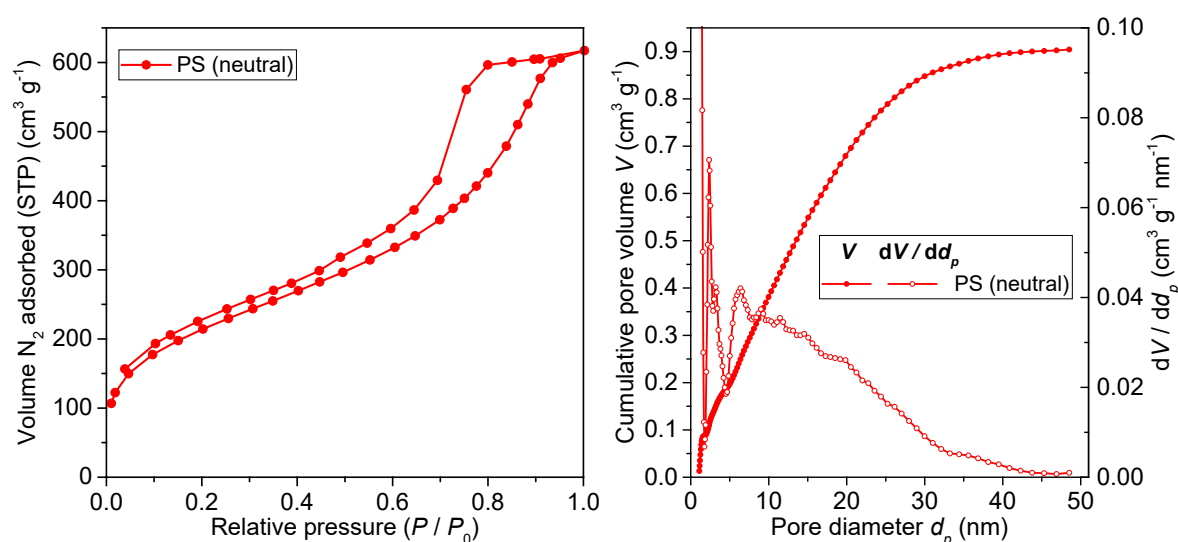


**Figure 3-19:**  $\text{N}_2$  physisorption isotherms (**left**) and pore size distribution (**right**) of granular (1-5mm) polystyrene (“PS”) before sulfonation (“neutral”). Measurement conducted at 77.3 K. Calculation of pore size distribution based on QSDFT adsorption method on carbon with slit, cylindrical, and spherical pores.

However, due to strong swelling of the resin in presence of water and other solvents, it is possible that the porosity during liquid-phase catalytic operation differs strongly from the porosity observed during nitrogen physisorption.

**Table 3-17:** Nitrogen physisorption data of granular (1-5mm) polystyrene before sulfonation (“neutral”).

Sample	Pore volume [cm <sup>3</sup> /g]				Specific surface area [m <sup>2</sup> /g]				Average pore size [nm]
	QSDFT adsorption			BJH ads.	QSDFT adsorption			BET	
	Micro	Meso	Total	Total	Micro	Meso	Total	Total	
	< 2 nm	2-50nm	≤ 50nm	≤ 500nm	< 2 nm	2-50nm	≤ 50nm		
PS (neutral)	0.09	0.81	0.90	0.94	147	467	614	767	4.9

## 3.4 Solid Base Catalyst

In the present work, an Al<sub>2</sub>O<sub>3</sub>-type material with 10wt% ZrO<sub>2</sub> is used as a base catalyst for the conversion of glucose, as presented in chapter 5.1.2. The morphology of the material, which is present as extruded cylindrical shapes of 1.6 mm diameter and average length of 3 mm, is examined in the following subchapter.

### 3.4.1 Characterization

#### 3.4.1.1 Porosity

N<sub>2</sub> physisorption has been performed on the 10wt% ZrO<sub>2</sub>-Al<sub>2</sub>O<sub>3</sub> material. As can be seen from the isotherm and pore size distribution (NLDFT adsorption) in Figure 3-20, the material exhibits a purely mesoporous morphology with no contribution from the mesoporous range and (presumably) the macroporous range. From the NLDFT model, a narrow pore size range of 7 to 30 nm is determined.

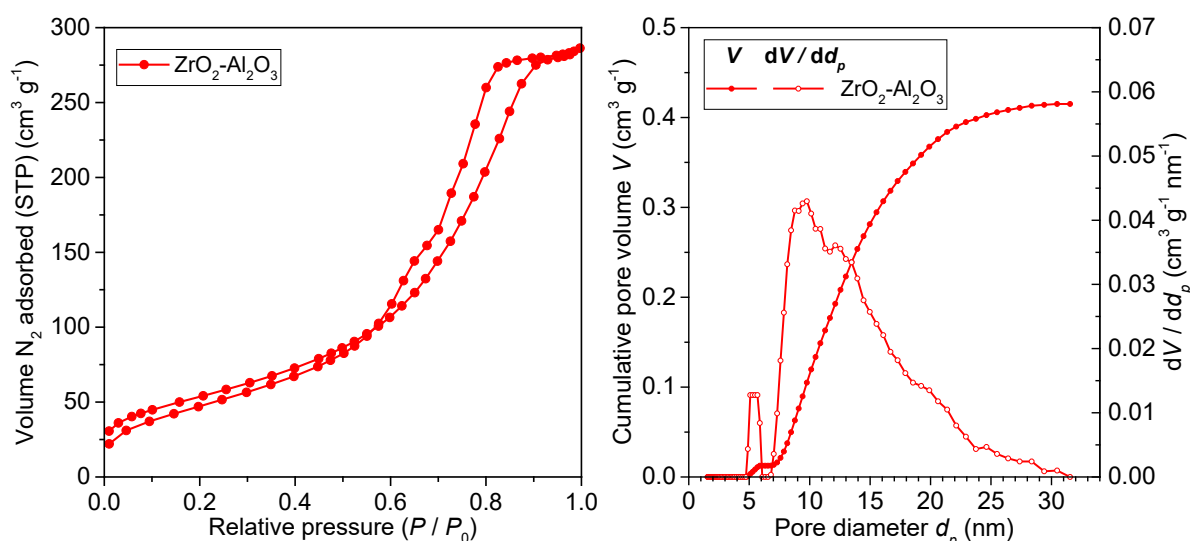


**Figure 3-20:** N<sub>2</sub> physisorption isotherms (**left**) and pore size distribution (**right**) of 10wt% ZrO<sub>2</sub>-Al<sub>2</sub>O<sub>3</sub> (1.6 × 3 mm). Measurement conducted at 77.3 K. Calculation of pore size distribution based on NLDFT adsorption method on “zeolite” with cylindrical and spherical pores.

Furthermore, a total, *i.e.* meso-, pore volume of 0.41 cm<sup>3</sup>/g and total surface area of 201 m<sup>2</sup>/g has been determined, as summarized in Table 3-18.

**Table 3-18:** Nitrogen physisorption data of 10wt% ZrO<sub>2</sub>-Al<sub>2</sub>O<sub>3</sub> (1.6 × 3 mm).

Sample	Pore volume [cm <sup>3</sup> /g]				Specific surface area [m <sup>2</sup> /g]				Average pore size [nm]
	NLDTF adsorption			BJH ads. Total	NLDTF adsorption			BET Total	
	Micro	Meso	Total		Micro	Meso	Total		
	< 2 nm	2-32nm	≤ 32nm		< 2 nm	2-32nm	≤ 32nm		
PS (neutral)	0.00	0.41	0.41	0.44	0	201	201	194	4.5



# 4

## REACTOR DESIGN

### 4.1 Continuous Flow Set-up

In order to investigate the catalytic performance of the prepared materials in flow experiments under varied conditions, a continuous flow set-up has been planned and built. It can accommodate several interchangeable packed-bed reactors of different sizes, thus allowing for operation from small lab size to scaled-up experiments in the liter scale.

As shown on the pictures of Figure 4-1, constant volumetric flow of reactant solution (1) is provided by an HPLC pump (2) (Knauer Azura P 4.1S pump with 50 mL/min ceramic piston pump head). Hydrogen gas from the high pressure line is throttled by a forward pressure regulator to an intermediary pressure of *ca.* 90 bar and introduced into a mass flow controller (Brooks Instruments SLA5850), which is calibrated to a hydrogen flow of up to 60 mL/min (STP) and controlled by a computer interface. A check valve (3) prevents backflow of the reactant solution through the hydrogen feed line and, therefore, potential damage of the sensitive controlling unit.

To maximize the dissolution of hydrogen in the liquid, the gas flow is injected and dispersed into the liquid by a nozzle (4) consisting of a Tee piece with a 0.3 mm orifice. A preheating unit (5) heats the feed to the desired reaction temperature. Owing to the two individually controlled heating sections consisting of heating bands and thermocouples winded around the reactor, isothermal conditions inside the reactor can be ensured. Three additional thermocouples, attached along the outer wall of the reactor (6), facilitate precise monitoring of the temperature development.





Figure 4-1: Implemented continuous flow set-up with large packed-bed reactor (OD1.5inch)



Furthermore, to check for potential radial temperature gradients inside the large reactors, the temperature is constantly monitored *in situ* in the middle of the catalyst bed by a temperature probe that is connected through a Tee piece at the outlet (7). The outlet flow is cooled by a cooling coil which is immersed into a reservoir of cooling water (8). Depending on the necessary cooling capacity, determined by the heat capacity rate of the outlet flow and the volatility of the product compounds, the cooling water is either stagnant or connected to the water tap and drain to provide a steady flow of cooling agent.

The desired system pressure is manually set by a back pressure regulator. A potential pressure drop in the system is noticeable as the difference of pressure indicated by the HPLC pump and pressure indicated by the manometer (9) prior to the back pressure regulator (10). After release to atmospheric pressure, the product solution is collected in a bottle (11).

A safety manifold (12) prior to the reactor inlet ensures safe operation. It connects the system to a safety relief valve (13) and a rupture disk (14) that bursts at 130 bar.

The reactors, the high pressure piping, and most of the equipment units are made from stainless steel 316L. The pressure-resistant connections between the equipment units and the piping are established by Swagelok® tube fittings, American National Pipe Thread (NPT) connections, and HPLC fittings. Even though the operation conditions of the experiments usually do not exceed 80 bar and 260 °C, the set-up could be operated at up to 95 bar, limited by the mass flow controller of the hydrogen feed. For reactions without hydrogen feed, the set-up is capable of safe operation at up to 290 bar (at room temperature) and up to 450 °C (at 225 bar), according to the pressure and temperature ratings provided by the manufacturer of the tubing and instrumentation<sup>98,99</sup>.

The main equipment units as well as instrumentation and controlling devices are presented in the piping and instrumentation diagram of Figure 4-2.

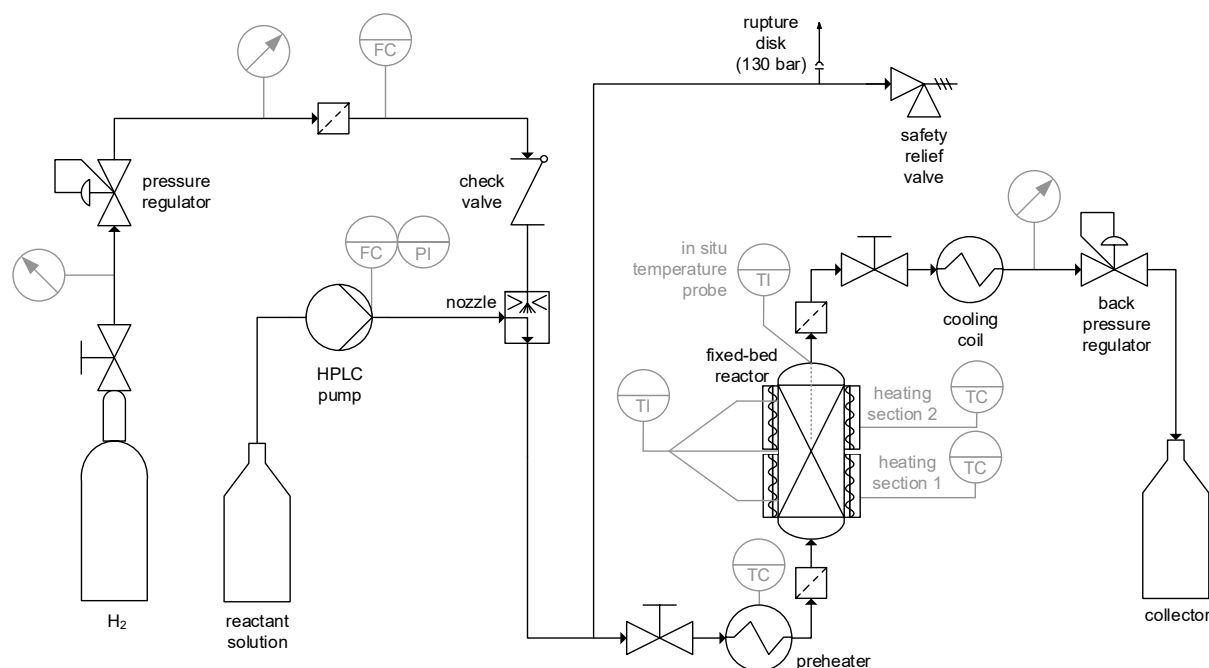


**Figure 4-2:** Piping and instrumentation diagram (P&ID) of the continuous flow set-up. FC: flow control; PI: pressure indication; TI/TC: temperature indication/control

The present flow setup is designed to provide optimal performance for the investigated three-phase (G-L-S) hydrogenation reactions. For this, the operation mode of the catalytic reactor is of particular importance. Due to the greater distance of the actual concentrations in the solution from the chemical equilibrium, tubular packed-bed reactors provide kinetic advantages, such as accelerated reaction rates, shorter reaction time, and higher selectivity, compared with gradient-free continuously stirred reactors such as bubble columns. To cover several stages of the development of catalyzed processes, starting from preliminary lab scale to scaled-up experiments, several packed-bed reactors of different sizes are built and employed for the catalytic experiments. Their dimensions are listed in Table 4-1.

**Table 4-1:** Dimensions of packed-bed reactors used with the flow set-up, compared with the particle size of the synthesized  $2.4 \times 3.5$  mm catalyst pellets

Reactor	Outer diameter [mm]	Inner diameter [mm]	Length [mm]	Volume [mL]	$d_R/d_S$	$L_R/d_S$
<b>OD11mm</b>	11.0	7.8	300	14.3	2.4	91
<b>OD1inch_1</b>	25.4	21.2	80	28.2	6.4	24
<b>OD1inch_2</b>	25.4	21.2	400	141.0	6.4	121
<b>OD1.5inch</b>	38.1	28.5	800	512.1	8.7	242

The set-up has been further adjusted over time to fit the current requirements of the specific catalytic process. To provide a very large cooling capacity in case of high reactant flow rates of up to 50 mL/min through the large reactor (OD1.5inch), an additional heat exchanger has been built, consisting of 10 windings of the cooling coil, immersed into flowing cooling water, as shown in Figure 4-3 (left). On the other hand, when using the small OD11mm reactor with flow rates of < 10 mL/min, the large cooling coil and the large outlet tubing are oversized and would cause strong dispersion of the flow. Therefore, to minimize the dead volume downstream of the reactor, a separate, downsized outlet incl. cooling coil has been built from 1/16" tubing, presented in Figure 4-3 (right).



**Figure 4-3:** Size adjustments of the continuous flow set-up. **left:** heating coil with high cooling capacity. **right:** Downsized set-up with OD11mm reactor and decreased dead volume in the outlet

## 4.2 Flow Dispersion

In order to facilitate catalytic performance that is not diminished by dispersion of the flow inside the packed-bed reactor, it is desirable to obtain plug flow behavior. This can be assumed if the following two criteria are fulfilled.

According to Mears, radial dispersion is negligible if the catalyst particles are sufficiently small, compared with the inner reactor diameter  $d_R^{100}$ :

$$\frac{d_R}{d_s} > 8 \quad (4.1)$$

with the equivalent spherical diameter of the  $2.4 \times 3.5$  mm cylindrical pellets:

$$d_s = \sqrt{d_{cyl} L_{cyl} + d_{cyl}^2/2} = 3.3 \text{ mm} \quad (4.2)$$

Furthermore, according to Gierman, axial dispersion inside the reactor bed will not occur if the following criterion is satisfied, based on the Bodenstein number  $Bo$  and the reaction order  $n$  in reactant<sup>101</sup>:

$$\frac{L_R}{d_s} > \frac{8}{Bo} n \ln \frac{1}{1-X} \quad (4.3)$$

with common values for the right side of the inequality ranging between 25 and 100 in liquid-solid packed-bed reactions<sup>102</sup>.

As can be seen from the two columns on the right of Table 4-1, the criteria are fulfilled for the largest reactor, but not for the small ones, suggesting concentration gradients for the latter inside the catalyst bed due to large void channels, on which the liquid can bypass the catalyst. However, conducting experiments in an early stage of the catalyst development on a scale that fulfills the criteria would consume a lot of material and is therefore not practical. On the other hand, crushing the pellets into powder is not considered a desirable solution for the catalyst screening either, as this procedure could disguise potential influence of mass transfer limitations inside the pellets and, therefore, change the nature of the catalytic behavior.

As the criterion by Mears describes the effect of the preferential trickle flow through the voids close to the reactor wall rather than in the middle of the reactor due to the high bed porosity near the reactor wall<sup>100</sup>, it is assumed that this effect can be reduced to a minimum when filling the voids between the pellets with non-porous inert material of smaller particle size that fulfills the criterion. To estimate how well the voids can be filled, three transparent quartz tubes with an ID of 7 mm were filled with the  $2.4 \times 3.5$  mm catalyst pellets. Subsequently, one of the tubes was filled on top with SiC (840-1190  $\mu\text{m}$ ), while the second was filled with pure HCl-washed sea sand (100-315  $\mu\text{m}$ ). After softly shaking and tapping on the tubes, the sand easily trickled down the tube, filling the large voids entirely without accumulating at the bottom or displacing the pellets from the bottom towards the top of the tube, as can be seen in Figure 4-4. In contrast, the SiC did not decently fill the empty spaces, but settled at the bottom of the tube, pushing the pellets upwards without efficiently decreasing the bed porosity.



**Figure 4-4:** Three quartz tubes (ID 7 mm) filled with  $2.4 \times 3.5$  mm catalyst pellets. **middle:** subsequently filled with SiC (840-1190  $\mu\text{m}$ ); **bottom:** subsequently filled with pure HCl-washed sea sand (100-315  $\mu\text{m}$ )

The result of this test suggests that the insertion of sand into the reactor, subsequent to the filling with catalyst pellets, could be highly beneficial for preventing or reducing radial dispersion of the flow even in the ID7.8mm reactors (OD11mm and OD12mm). As the length of the OD11mm reactor is greater by a factor of 91 than the equivalent spherical diameter of the pellets, the reactor is expected to fulfill the criterion for negligible axial dispersion under most catalytic conditions and hydrodynamic states that occur inside the reactor. Based on these assumptions, it can be concluded that the reaction in the OD11mm reactor, filled with catalyst pellets plus sea sand, proceeds under *quasi* plug-flow for most operation conditions. This hypothesis is strongly supported by the catalytic results presented in section 5.2.



# 5

## CATALYST PERFORMANCE

In order to obtain a good understanding of the catalyst behavior for the several steps of a valorization chain, it is necessary to map the catalytic performance of the several reaction steps individually under ideal reaction conditions before determining suitable parameters for the process integration. As outlined in Figure 5-1, the present work comprises all reaction steps involved in the valorization of the hexoses glucose and fructose towards the platform molecules 2,5-dimethylfuran (DMF) and  $\gamma$ -valerolactone (GVL). For the conversion of the sugars towards 5-hydroxymethylfurfural (HMF) and levulinic acid (LA), highlighted in grey color, catalysts with solid acid and base sites are applied, while for the hydrogenation reactions of the intermediates, highlighted in green color, the prepared metal-based carbon-supported catalysts are employed.

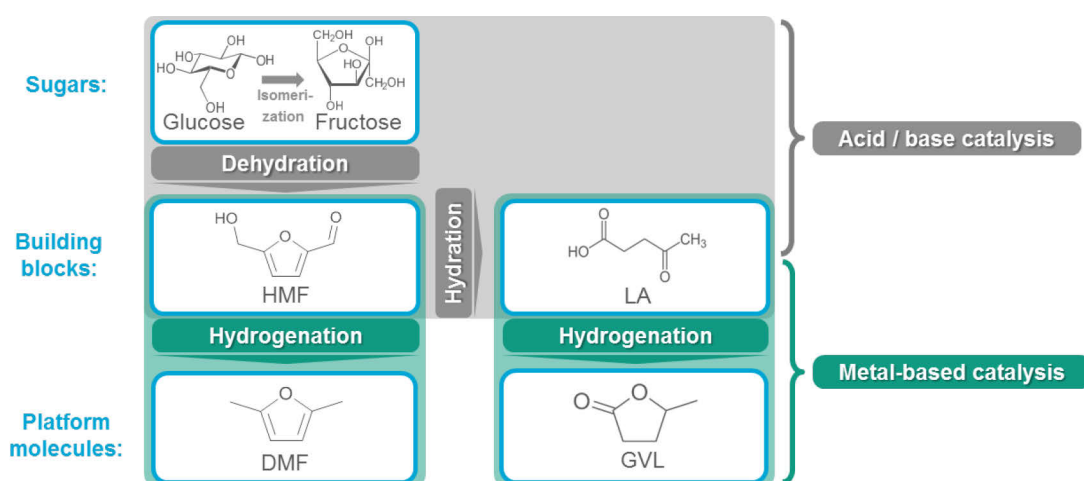


**Figure 5-1:** Reaction scheme of catalyzed processes presented in this section

In analogy to the catalyst design in chapter 3 with the focus on a new synthesis methodology of highly active Ni/C and Pt/C hydrogenation catalyst pellets, the catalytic results presented in this chapter set the focus on the performance of the prepared catalysts in the hydrogenation reactions of HMF and LA, presented in subchapter 5.2 and 5.3, respectively.

As the carbon pellets prepared on the ZnO route (C<sub>ZnO</sub>) exhibit the best properties as a catalyst support, the major part of the hydrogenation experiments is conducted over catalysts supported on C<sub>ZnO</sub>. Therefore, these catalysts are denominated in the following by Ni/C and Pt/C instead of the long names Ni/C<sub>ZnO</sub> and Pt/C<sub>ZnO</sub>, whereas the Ni-based catalysts supported on the other two routes presented in chapter 3 are denominated by their complete names Ni/C<sub>ZnCl</sub> and Ni/C<sub>NaCl</sub>, respectively.

In the spirit of green chemistry, the catalytic experiments in this research focus on the use of non-hazardous and cheap solvents that are bioderived or widely available in nature. As water and ethanol – without doubt two of the greenest solvents available<sup>50</sup> – complement one another in their solubility of the different classes of molecules involved in the presented valorization scheme (carbohydrates, polar organic molecules, nonpolar organic molecules), they are chosen as solvents for the flow chemistry experiments in the following sections.

Throughout all experiments, the conversion  $X$  of reactant is determined by the ratio of consumed reactant to total introduced reactant:

$$X = \frac{N_{react}^0 - N_{react}}{N_{react}^0} \text{ (product sample)}; \quad X = \frac{\dot{N}_{react}^0 - \dot{N}_{react}}{\dot{N}_{react}^0} \text{ (flow)} \quad (5.1)$$

The space time, a common measure for the contact time of the reactant with the catalyst, is defined in this section as the ratio  $\tau_w$  of total catalyst weight to reactant *mass* flow rate, according to the following equation:

$$\tau_w = \frac{m_{cat}}{\dot{m}_{react}^0} \left[ \frac{g_{cat} \text{ h}}{g_{react}} \right] \quad (5.2)$$

The yield of a product  $i$  describes the fraction of reactant that has been transformed into that specific molecule. For reaction networks that involve C-C bond cleavage (or linkage), it is practical to define the yield  $Y_i$  with respect to the C equivalents of the substances:

$$Y_i = \frac{\nu_i N_i}{\nu_{react} N_{react}^0} \text{ (product sample)}; \quad Y_i = \frac{\nu_i \dot{N}_i}{\nu_{react} \dot{N}_{react}^0} \text{ (flow)} \quad (5.3)$$



where  $v_i$  represents the number of C atoms per molecule  $i$ . In analogy, the selectivity  $S_i$  of a product  $i$  is defined as the C-based product fraction that is present in this specific molecule  $i$ :

$$S_i = \frac{v_i N_i}{\sum_j v_j N_j} = \frac{v_i N_i}{v_{react} (N_{react}^0 - N_{react})} = \frac{Y_i}{X} \quad (\text{product sample}) \quad (5.4)$$

## 5.1 Valorization of Sugars

In order to cover the whole upgrading scheme of the cellulose-derived monosaccharides glucose and fructose towards the value-added DMF and GVL, presented in Figure 5-1, this section is dedicated to preliminary results on the catalytic performance of fructose and glucose conversion towards HMF and LA, the reactant molecules of the hydrogenation processes that are presented in the subchapters 5.2 and 5.3 and form the core of the catalysis part of this work.

### 5.1.1 Dehydration of Fructose

In this section, the results of the acid-catalyzed fructose dehydration experiment are presented. As presented in subchapter 2.4.2.1, solid Brønsted acids, in particular sulfonated polystyrene materials, have been identified in the literature as suitable catalysts for the selective conversion of fructose towards HMF. The present work aims at providing a basis for an integrated valorization process of sugar dehydration towards HMF, followed by immediate hydrogenation towards DMF, preferably in a single bicatalytic reactor with mixed bed of solid acid and metal-based catalysts. Since the prepared Ni/C catalysts exhibit low activity for the HMF hydrogenation process at temperatures below 130 °C, presented in section 5.2, Amberlyst-15 is not considered a suitable option due to its temperature instability above 130 °C. Instead, a highly crosslinked granular (1-5mm) sulfonated polystyrene resin is used for the fructose dehydration, as its strong divinylbenzene crosslinking allows for operation at higher temperature. As presented in subchapter 3.3.1.2., this predominantly mesoporous material exhibits a surface area of 614 m<sup>2</sup>/g and a pore volume of 0.90 cm<sup>3</sup>/g, determined from N<sub>2</sub> physisorption measurement and QSDFT analysis on the adsorption branch.

For a 0.1M fructose in H<sub>2</sub>O reactant solution, HMF yield of 21.4% and 13.0% has been obtained at 150 °C (space time of 3.5 g<sub>cat</sub> h g<sub>fru</sub><sup>-1</sup>) and 130 °C (space time of 7.1 g<sub>cat</sub> h g<sub>fru</sub><sup>-1</sup>), respectively, as can be seen in Figure 5-2. In addition to the HMF yield, a large part of the as-formed HMF is consumed in the subsequent formation of LA, which is strongly increased at longer space times. At comparable conversion range, operation at 150 °C provides higher yield of

HMF over LA. The highest HMF selectivity (50.4%) was obtained at 150 °C in the medium conversion range (42.3%). Including the valuable consecutive products LA (20.7%) and formic acid (13.4%), a total carbon-based product selectivity of 84.5% was reached at this point.

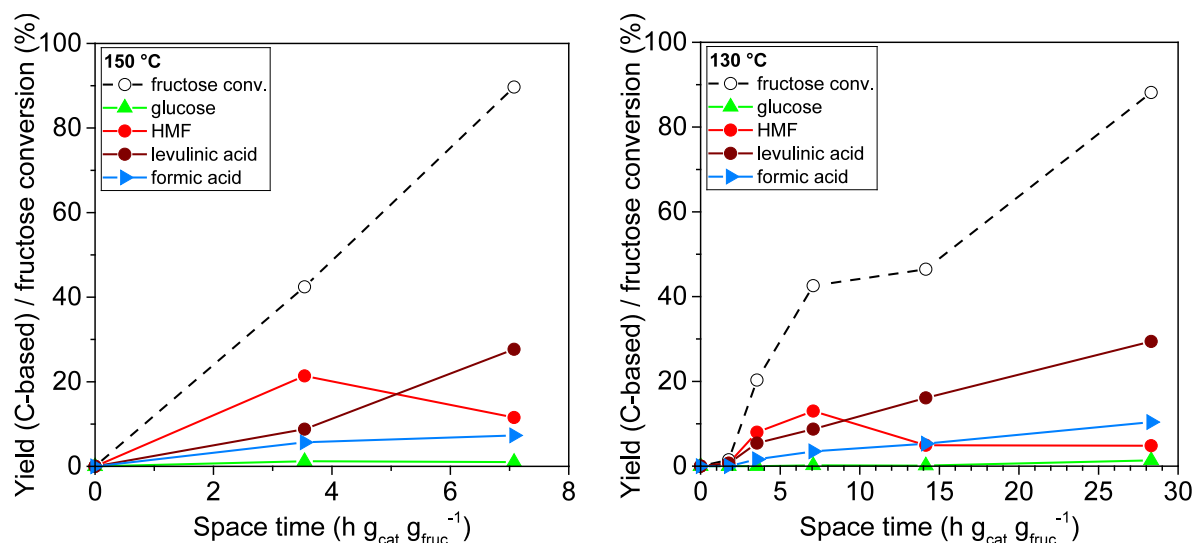


**Figure 5-2:** Product yields for the conversion of fructose over granular (1-5mm) sulfonated polystyrene-divinylbenzene, as a function of space time. Conditions: 0.1M fructose in H<sub>2</sub>O reactant solution, 150 °C (left) and 130 °C (right)

Even though higher total product yields could be reached by increasing the space time to values beyond those presented in Figure 5-2, it is not very suitable when aiming at the selective production of HMF, as longer exposure to the catalyst strongly favors the conversion of HMF towards LA and, therefore, decreases the HMF selectivity. This kinetic behavior points out the potential for an integrated process with short distances between the acid and metal sites, thus facilitating the immediate hydrogenation of the produced HMF and kinetically hindering the reaction towards LA<sup>29</sup>.

## 5.1.2 Conversion of Glucose

### 5.1.2.1 Solid base catalysis

As mentioned in section 2.4.2.2, efficient conversion of the stable pyranoside ring structure of glucose over heterogeneous catalysts still poses a big challenge. Since for Brønsted solid acids very low activity is observed for both of the two possible isomerization pathways<sup>30</sup>, an alumina material with 10wt% ZrO<sub>2</sub> is used in this section, as its basicity, combined with additional Lewis acid sites, promises higher catalytic activity for the isomerization<sup>44</sup>. The purely mesoporous catalyst exhibits a surface area of 201 m<sup>2</sup>/g and mesopore volume of 0.41 cm<sup>3</sup>/g, determined from N<sub>2</sub> physisorption measurement and NLDFT (adsorption) analysis, as presented in subchapter

3.4.1.1. It is present in extruded cylindrical shapes of 1.6 mm diameter and average length of 3 mm and is used in this section for continuous flow operation a packed-bed reactor.

Due to the high solubility of the sugars in water (in contrast to ethanol) and the hydrothermal stability of the  $\text{ZrO}_2\text{-Al}_2\text{O}_3$  material, water is a suitable green solvent for the glucose isomerization and is therefore used in this section.

As can be seen from Figure 5-3 (left), the observed conversion of glucose is highly dependent on the operation temperature, increasing from 35.8% at 125 °C to nearly complete conversion (99.2%) at 170 °C, using a 0.1M glucose reactant solution and space time of 3.3 h  $\text{g}_{\text{ZrO}_2} \text{g}_{\text{gluc}}^{-1}$ . High selectivity (49.0%) towards a mixture of (predominantly) fructose and (minor fractions of) mannose is observed at 125 °C, as shown in Figure 5-3 (right).

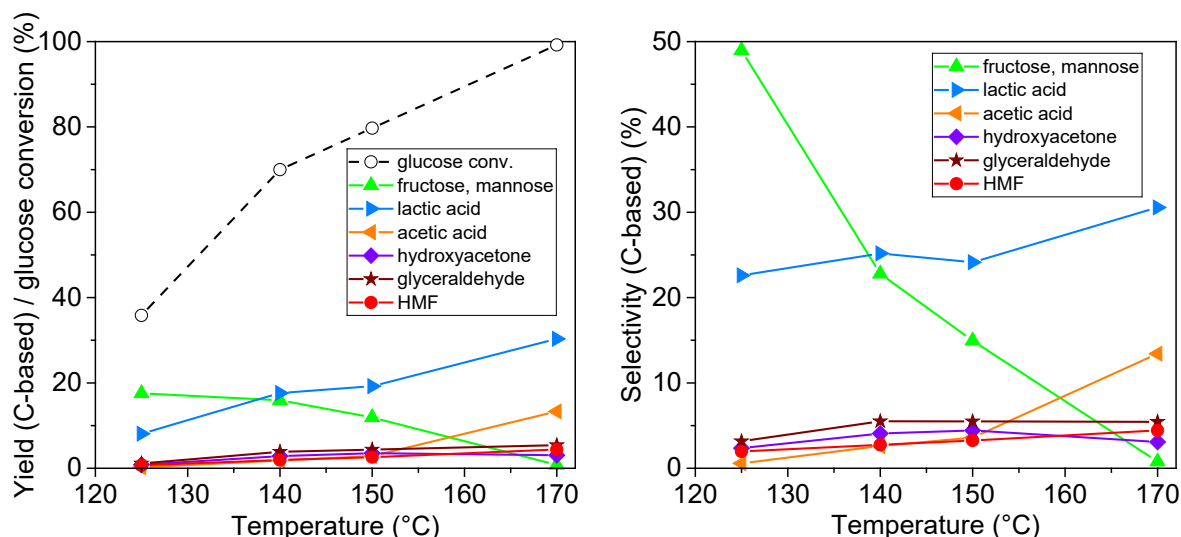


**Figure 5-3:** Product yields (**left**) and selectivities (**right**) for the conversion of glucose over 10wt%  $\text{ZrO}_2\text{-Al}_2\text{O}_3$  ( $1.6 \times 3$  mm), as a function of temperature. Conditions: 0.1M glucose in  $\text{H}_2\text{O}$  reactant solution, space time of 3.3 h  $\text{g}_{\text{ZrO}_2} \text{g}_{\text{gluc}}^{-1}$ , 25 bar

The obtained fructose + mannose yield of 17.5% with a glucose conversion of 35.8% is on a similar level as reported by Qi *et al.*<sup>44</sup> for a comparable catalytic system with glucose in water solutions over  $\text{ZrO}_2$ , which provided yields of 17.4% for fructose, no specification for mannose, and 7.7% for HMF, with a total glucose conversion of 41.6%. However, Qi *et al.*<sup>44</sup> were employing much higher temperature of 200 °C with additional microwave irradiation. Compared with the  $\text{ZrO}_2$  catalyst used by Qi *et al.*<sup>44</sup>, the present 10wt%  $\text{ZrO}_2\text{-Al}_2\text{O}_3$  catalyst exhibits relatively low activity in the acid-catalyzed dehydration of fructose to HMF, providing HMF yield of only up to 4.4% at the highest operation condition of 170 °C, as presented Figure 5-3 (left).

At temperature higher than 125 °C, all three sugar isomers appear to be very prone to competing decomposition reactions towards a variety of low molecular compound, with highest

yield for lactic and acetic acid and low yields of < 5% for hydroxyacetone and glyceraldehyde. Due to the high yield of C<sub>3</sub> products, it is assumed that the present base sites hydrolyze the C<sub>3</sub>-C<sub>4</sub> bond of the C<sub>6</sub> sugars. While base sites are known to promote the isomerization reaction between glucose, fructose, and mannose *via* the 1,2-enediol mechanism shown previously in Figure 2-6, they can also facilitate aldol condensation as well as the inverse reaction, the retro-aldol reaction of the transient C<sub>6</sub> enediol towards the transient propenetriol, which is isomerized towards the aldose glyceraldehyde or the ketose dihydroxyacetone, in analogy to the glucose-fructose isomerization<sup>103</sup>, as presented in Figure 5-4.

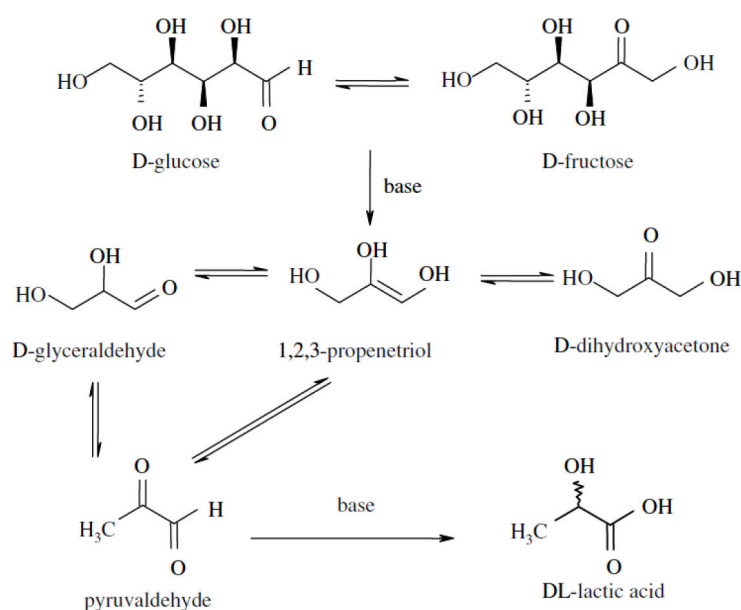


**Figure 5-4:** Decomposition of glucose and fructose by base-catalyzed *retro*-aldol reaction. Adapted from Onda *et al.*<sup>103</sup>.

Further base-catalyzed dehydration and hydration reactions produce the observed high yields of lactic acid of up to 30.3% at 170 °C in the presented temperature study of Figure 5-3 (left). Even though lactic acid is a valuable commodity chemical with high demand in the food, pharmaceuticals, and polymer industry<sup>103</sup>, the retro-aldol reaction is detrimental to high yields for the HMF production scheme presented in Figure 5-1. The trend of product composition over space time, shown in Figure 5-5, confirms the high instability of the as-formed fructose and mannose for longer exposure to the catalyst at the high temperature of 150 °C.

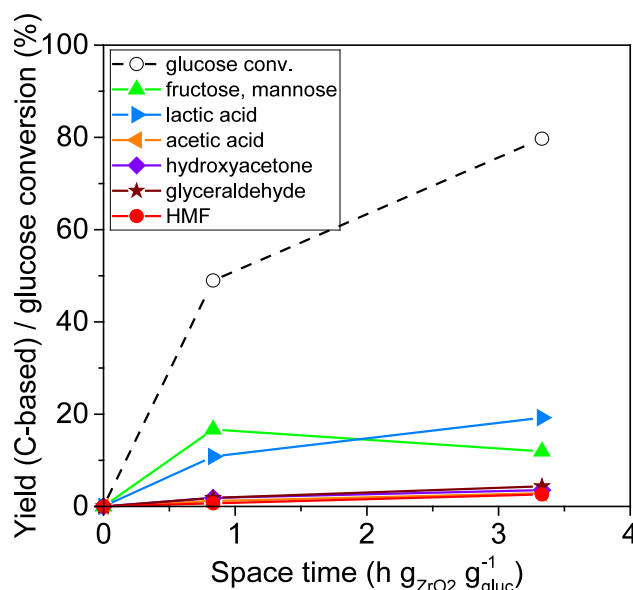


**Figure 5-5:** Product yields for the catalytic conversion of glucose over 10wt% ZrO<sub>2</sub>-Al<sub>2</sub>O<sub>3</sub> (1.6 × 3 mm), as a function of space time. Conditions: 0.1M glucose in H<sub>2</sub>O reactant solution, 150 °C, 25 bar.

Although the activity and yield of fructose production and subsequent HMF production would presumably be strongly enhanced by the addition of Cl<sup>-</sup>, *e.g.* a water/[HMIM]Cl mixture, as reported in the literature<sup>48</sup>, the use of salts and ionic liquids does not comply with the spirit of the present approach, which prioritizes on the development of sustainable processes with greener solvents.

#### 5.1.2.2 Combined solid base and acid catalysis

The previously presented catalytic system still offers potential for enhancement of the reactivity without employing less green approaches. Since the 10wt% ZrO<sub>2</sub>-Al<sub>2</sub>O<sub>3</sub> catalyst exhibits very low activity for the subsequent dehydration of fructose to HMF, it was complemented by the polystyrene sulfonate (PSS) material, in order to shift the chemical equilibrium of the isomers towards the production of fructose and prevent re-isomerization of the fructose.

From the previous experiments in the sections 5.1.1 and 5.1.2.1, it was estimated that for the 10wt% ZrO<sub>2</sub>-Al<sub>2</sub>O<sub>3</sub> ca. three times the volume is needed for the 10wt% ZrO<sub>2</sub>-Al<sub>2</sub>O<sub>3</sub>, compared with the PSS. To obtain a 75:25 vol.% catalyst packing, the reactor was filled with the two catalysts gradually along the reactor axis according to Figure 5-6, starting from 100% of the ZrO<sub>2</sub>-Al<sub>2</sub>O<sub>3</sub> material at the inlet to 0% at the outlet.

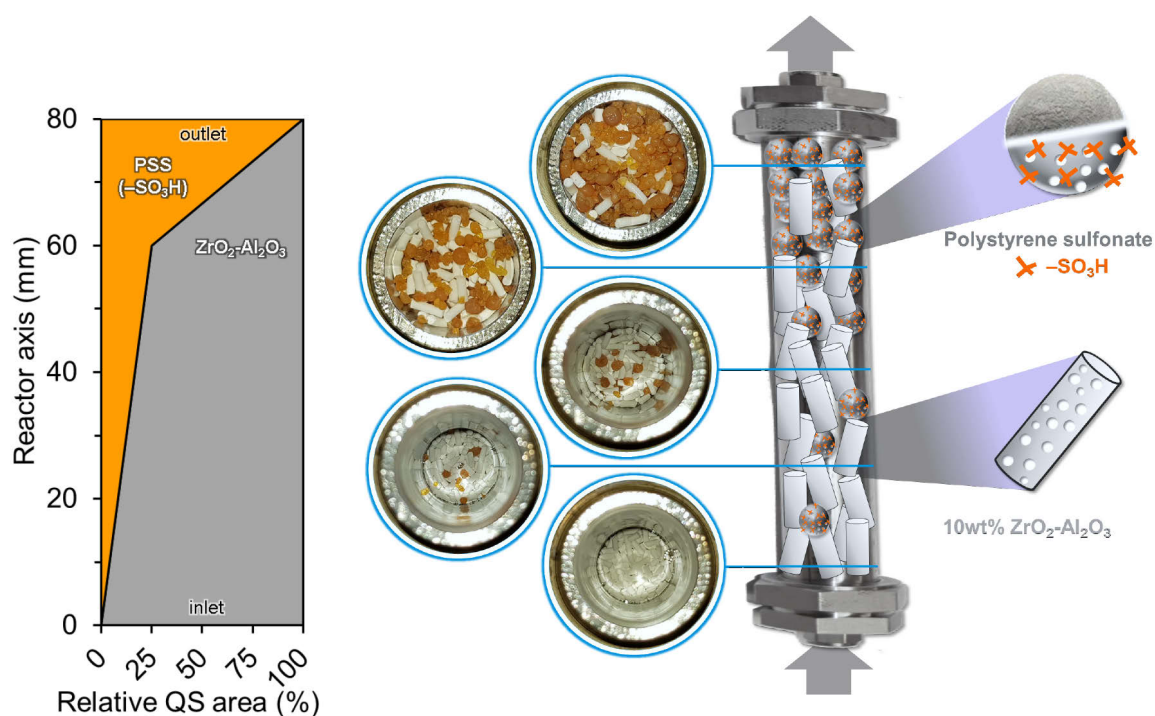


**Figure 5-6:** Bed packing of bicatalytic reactor with 10wt%  $\text{ZrO}_2\text{-Al}_2\text{O}_3$  (1.6×3 mm) and granular (1-5mm) polystyrene sulfonate (“PSS”). Packed bed consists of 75vol.%  $\text{ZrO}_2\text{-Al}_2\text{O}_3$  and 25vol.% PSS. Dimensions of “OD1inch\_1” reactor (see section 4.1): 21×80 mm (ID×L), cross-sectional (“QS”) area of bed 352 mm<sup>2</sup>. **left:** profile of relative QS areas of the catalysts along reactor axis; **middle:** photos of several cross-sections, taken during bed packing; **right:** scheme of catalyst distribution.

To favor the isomerization of glucose over the hydrolysis, which was observed in section 5.1.2 especially at high temperatures, the reaction was operated at lower temperatures in this section. At 130 °C, C-based yields were obtained of 14.8% for fructose (with traces of mannose), 1.7% for HMF, and 0.9% for LA, along with the hydrolysis byproducts glyceraldehyde, hydroxyacetone, and lactic acid, as can be seen in Figure 5-7 at space time of 1.6 h  $\text{g}_{\text{ZrO}_2} \text{g}_{\text{gluc}}^{-1}$  for the base catalyst and 2.4 h  $\text{g}_{\text{PSS}} \text{g}_{\text{gluc}}^{-1}$  for the acid catalyst. Due to the low concentration of the intermediate fructose, product yields of HMF and LA were not achieved above this level. Instead, longer space times favor the base-catalyzed hydrolysis of the as-formed fructose and, therefore, entail even lower yields of HMF and LA.

The extent of sugar hydrolysis was strongly reduced at 110 °C, facilitating 15.1% yield of for fructose (with traces of mannose) in the experiment presented in Figure 5-8 (space time of 3.3 h  $\text{g}_{\text{ZrO}_2} \text{g}_{\text{gluc}}^{-1}$  and 4.9 h  $\text{g}_{\text{PSS}} \text{g}_{\text{gluc}}^{-1}$ ). However, due to the low temperature, hardly any activity is observed for the fructose dehydration, resulting in HMF and LA yields of below 1%.

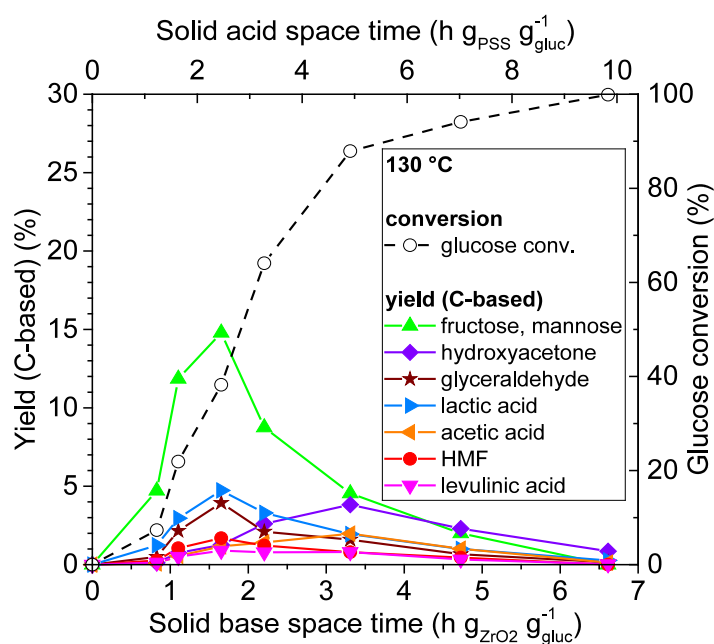


**Figure 5-7:** Product yields for the catalytic conversion of glucose in a bicatalytic reactor with 10wt%  $\text{ZrO}_2\text{-Al}_2\text{O}_3$  ( $1.6 \times 3$  mm) and granular (1-5mm) sulfonated polystyrene-divinylbenzene, as a function of space time. Conditions: 0.1M glucose in  $\text{H}_2\text{O}$  reactant solution, 130 °C, 20 bar.

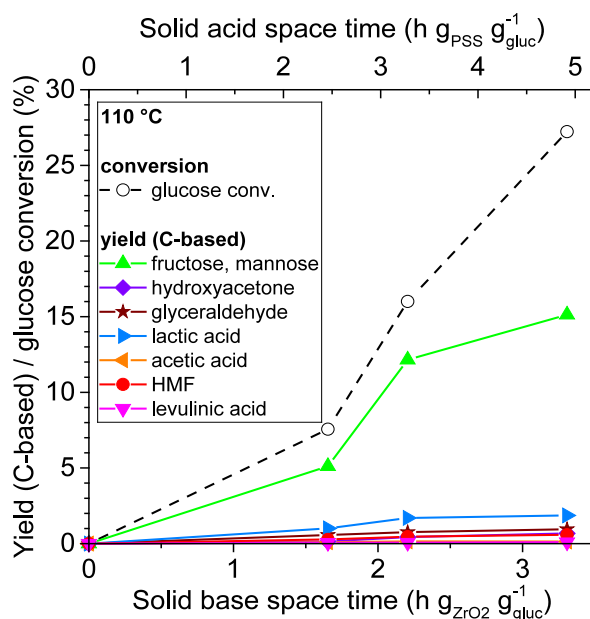


**Figure 5-8:** Product yields for the catalytic conversion of glucose in a bicatalytic reactor with 10wt%  $\text{ZrO}_2\text{-Al}_2\text{O}_3$  ( $1.6 \times 3$  mm) and granular (1-5mm) sulfonated polystyrene-divinylbenzene, as a function of space time. Conditions: 0.1M glucose in  $\text{H}_2\text{O}$  reactant solution, 110 °C, 20 bar.

## 5.2 Hydrodeoxygenation of 5-Hydroxymethylfurfural

In this section, the selective hydrogenation of HMF to DMF over the prepared metal-based catalysts supported on porous carbon is presented. As mentioned in the introduction of chapter 5, this section focuses on the experiments with the Ni/C<sub>ZnO</sub> catalysts, which are abbreviated in the following by Ni/C.

In addition to the definitions of conversion, selectivity, and yield in section 5.1.2, the following quantities are used in this section and the following section 5.3:

The space time  $\tau_w$  is defined for the metal-based catalysts (Ni/C and Pt/C) as the ratio of *metal* weight  $m_{Ni}$  to the reactant mass flow rate, according to the following equation:

$$\tau_w = \frac{m_{Ni}}{\dot{m}_{HMF}^0} = \frac{w_{Ni} m_{Ni/C}}{\dot{m}_{HMF}^0} \quad \left[ \frac{g_{Ni} \text{ h}}{g_{HMF}} \right] \quad (5.5)$$

Furthermore, the Ni time yield  $NTY_i$  (and Pt time yield  $PTY_i$ ) is a measure to describe how much product  $i$  is formed per time unit and catalyst weight, while the *total* Ni time yield  $NTY_{tot}$  (and *total* Pt time yield  $PTY_{tot}$ ) describes the conversion of reactant per time unit and metal amount:

$$NTY_i = \frac{Y_i}{\tau_N} ; \quad NTY_{tot} = \frac{X}{\tau_N} \quad \left[ \frac{\text{mol}_i \text{ h}}{\text{mol}_{Ni}} \right] \quad (5.6)$$

where the space time  $\tau_N$  is used in its molar definition:

$$\tau_N = \frac{N_{Ni}}{\dot{N}_{HMF}^0} = \frac{w_{Ni} m_{Ni/C}}{\dot{N}_{HMF}^0 M_{Ni}} \quad \left[ \frac{\text{mol}_{Ni} \text{ h}}{\text{mol}_{HMF}} \right] \quad (5.7)$$

According to GC analysis of the HMF hydrodeoxygenation product solutions, the reaction proceeds via two parallel reaction pathways. Primary hydrodeoxygenation of the hydroxy group of HMF yields the intermediate 5-methylfurfural (5-MF), whereas primary carbonyl reduction of HMF produces 2,5-bis(hydroxymethyl)furan (BHMF), as summarized in Figure 5-9.



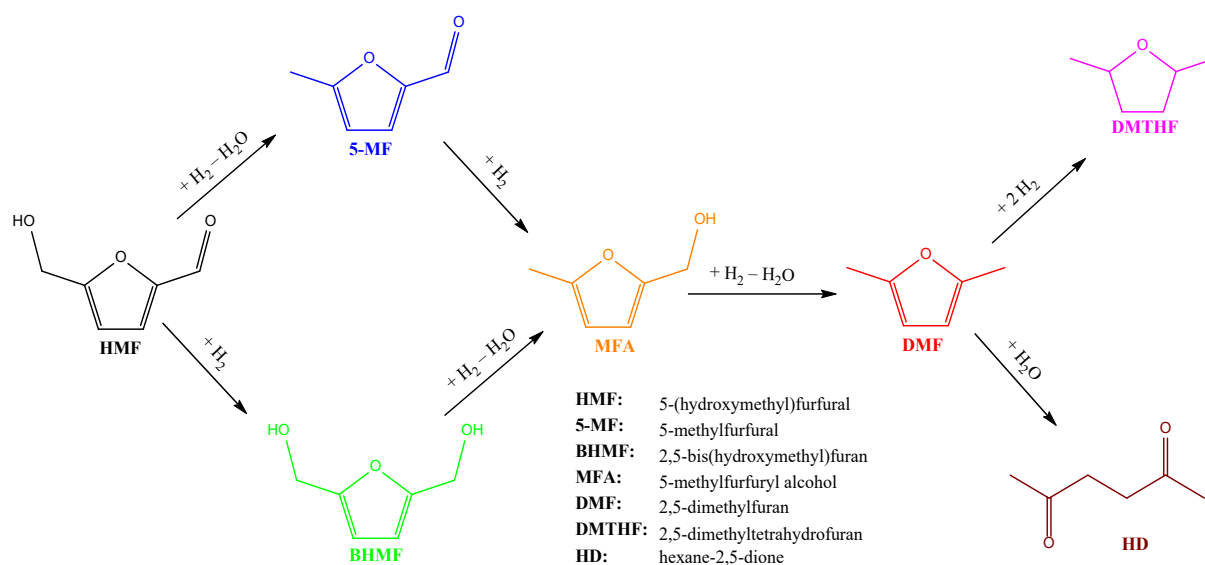


**Figure 5-9:** Reductive steps of HMF deoxygenation to DMF and consecutive reactions

The subsequent reduction step provides 5-methylfurfuryl alcohol (MFA), which is eventually deoxygenated to DMF. Depending on the catalytic system, subsequent saturation of the furanic ring towards 2,5-dimethyltetrahydrofuran (DMTHF) and hydrolysis towards hexane-2,5-dione (HD) can occur, which will be discussed in the following.

Due to the insolubility of the nonpolar DMF in water, water is not a suitable option as a solvent for a kinetic investigation of this reaction. Although DMF was obtained in a preliminary experiment using water as the solvent, DMF accumulates inside the catalytic bed for a long time before being flushed out of the system as droplets, making a steady state kinetic analysis practically impossible.

Therefore, ethanol is used as the solvent, which readily dissolves all involved species. However, as has been observed, ethanol chemically engages in several steps of the reaction, forming additional intermediates on parallel pathways by reacting with the oxygen-containing groups of the reactant and of the intermediates. In particular, the formyl groups of the furanic aldehydes appear to be very prone to acetalization in the presence of ethanol. Furthermore, the hydroxymethyl groups of the furanic alcohols can readily undergo etherification towards the concentration equilibrium with the ethoxymethyl group. As a result, the two parallel hydrogenation pathways of HMF towards DMF, observed for reactions in non-reactive solvents, are complemented by several side reactions, constituting a complex reaction network that involves formation and conversion of acetals and ethers.

The observed molecules are summarized and arranged into a proposed reaction scheme in Figure 5-10, based on GC-MS analysis of the obtained product solutions. For the sake of clarity,

in this work the acetals of HMF, 5-MF (5-methylfurfural), and EMF (5-ethoxymethylfurfural) are denoted as HMF-Ac, 5-MF-Ac, and EMF-Ac, respectively. Their correct IUPAC nomenclature is included in Figure 5-10.

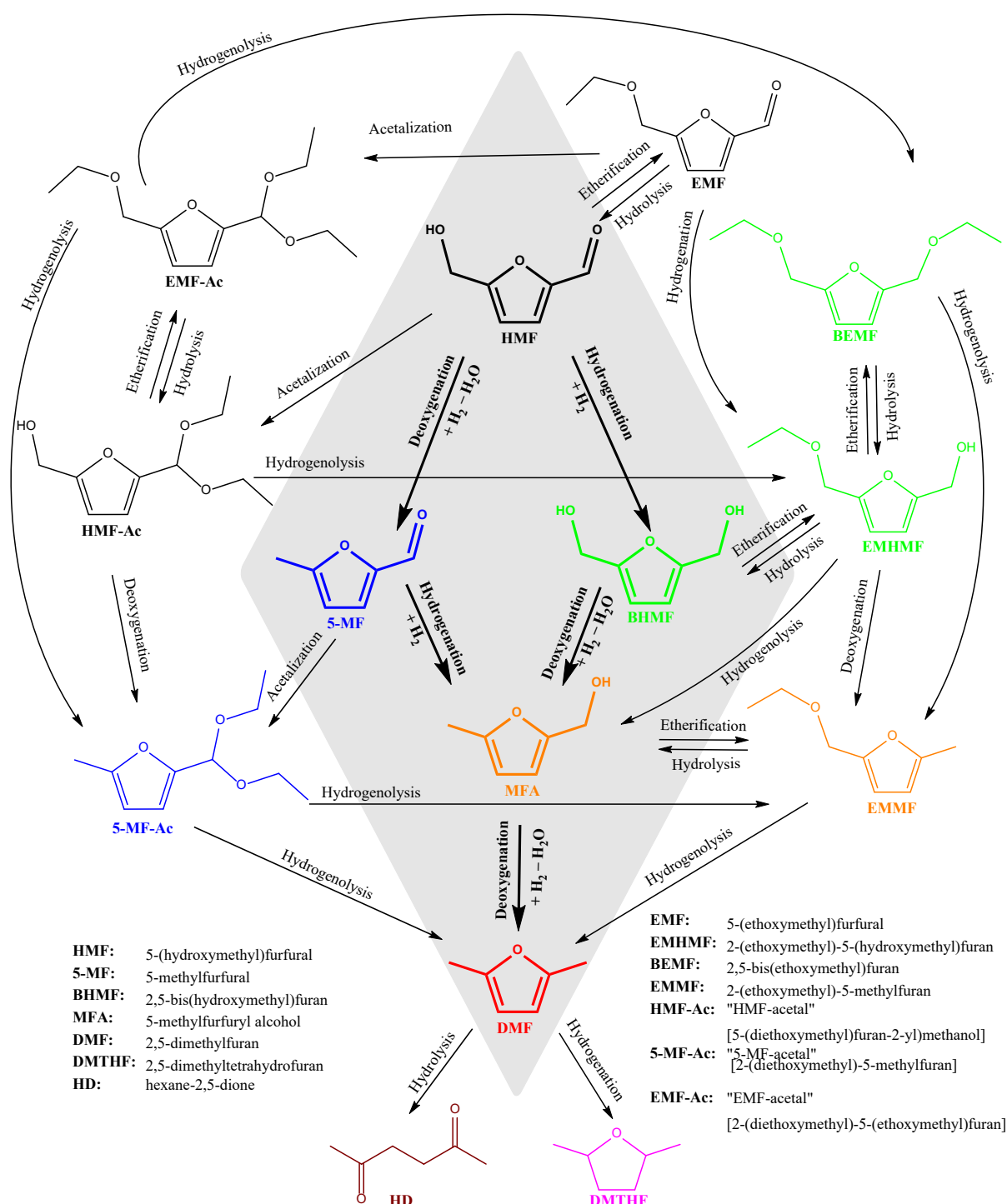


**Figure 5-10:** Proposed reaction scheme for HMF hydrodeoxygenation in ethanol, including the main hydrogenation steps (highlighted in grey), parallel side reactions with the solvent, and consecutive reactions of DMF. This scheme is deduced from GC-MS analysis.

In addition to the two parallel reduction pathways of HMF, highlighted by the grey diamond in Figure 5-10, the HMF derivatives EMF, HMF-Ac, and EMF-Ac now offer additional pathways for the reductive steps. The distribution of the products and intermediates is presented over space time in Figure 5-11 for the pelletized 21wt% Ni/C<sub>ZnO</sub> catalyst (2.4 × 3.5 mm), which was synthesized as described in section 3. According to the procedure described in the end of section 4.2, the high voidage between the catalyst pellets in the reactor bed was filled with ultrapure sea sand to prevent trickle flow of the liquid reactant solution. Despite the variety of additional parallel reactions, a DMF yield of 80.5% (99.0% HMF conversion) is obtained at a space time of 2.66 h g<sub>Ni</sub> g<sub>HMF</sub><sup>-1</sup>.

It is noteworthy that the intermediates are present primarily as ethers and acetals (represented as triangles and stars in the diagrams), with only minor quantities of alcohol and aldehyde intermediates (represented as dots). Particularly, an initial increase of HMF-Ac is observed at around 0.1 h g<sub>Ni</sub> g<sub>HMF</sub><sup>-1</sup>, followed by a prominent peak concentration of EMHMF at 0.33 h g<sub>Ni</sub> g<sub>HMF</sub><sup>-1</sup>. The total mole balance of all quantified components, represented by the grey line in Figure 5-11 (left), adds up to 96-99% of the HMF concentration in the reactant. As traces of furanic dimers were observed in several product samples, the missing 1-4% yield is attributed to the formation of humins, *i.e.* oligo- or polymerized furanic monomers.

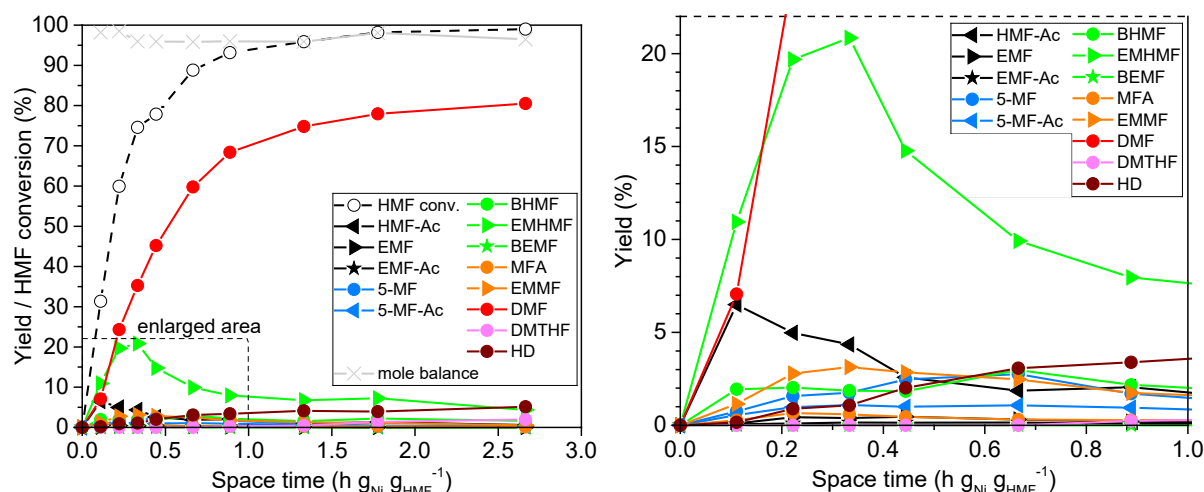


**Figure 5-11:** Effect of space time on yield in HMF hydrogenation over 21wt% Ni/C (2.4 × 3.5mm). Conditions: 0.1M HMF in EtOH reactant solution, 150 °C, 20 bar H<sub>2</sub> pressure, H<sub>2</sub>:HMF 7.5:1; **left:** whole range of investigated space time; **right:** enlarged section for low space time

To understand on which routes of the complex reaction network the molecules are preferentially formed and converted, a solution of 25 mmol L<sup>-1</sup> HMF, 5-MF, BHMf, and MFA has been prepared and heated to 150 °C for 1 h without exposure to H<sub>2</sub>, both in an empty reactor and filled with the 21wt% Ni/C catalyst to compare the influence of the catalyst to the purely thermal effect.

The reason for this is that, by eliminating the possible reduction steps, the influence of etherification and acetalization can be investigated more clearly.

In contrast to all catalytic reduction experiments, this screening has been conducted in batch mode inside a closed vessel, as in the absence of  $H_2$  polymerization was expected to occur and, therefore, clogging and damage of the continuous flow system would have been possible. Indeed, a high loss of monomers is observed in this experiment. As can be seen in Figure 5-12, the four reactants exhibit a loss of 2-10% and 5-40% in the blank reactor without catalyst and in the catalyzed system, respectively. The formed humins settled as yellowish insoluble powder on the catalyst surface and the reactor wall.

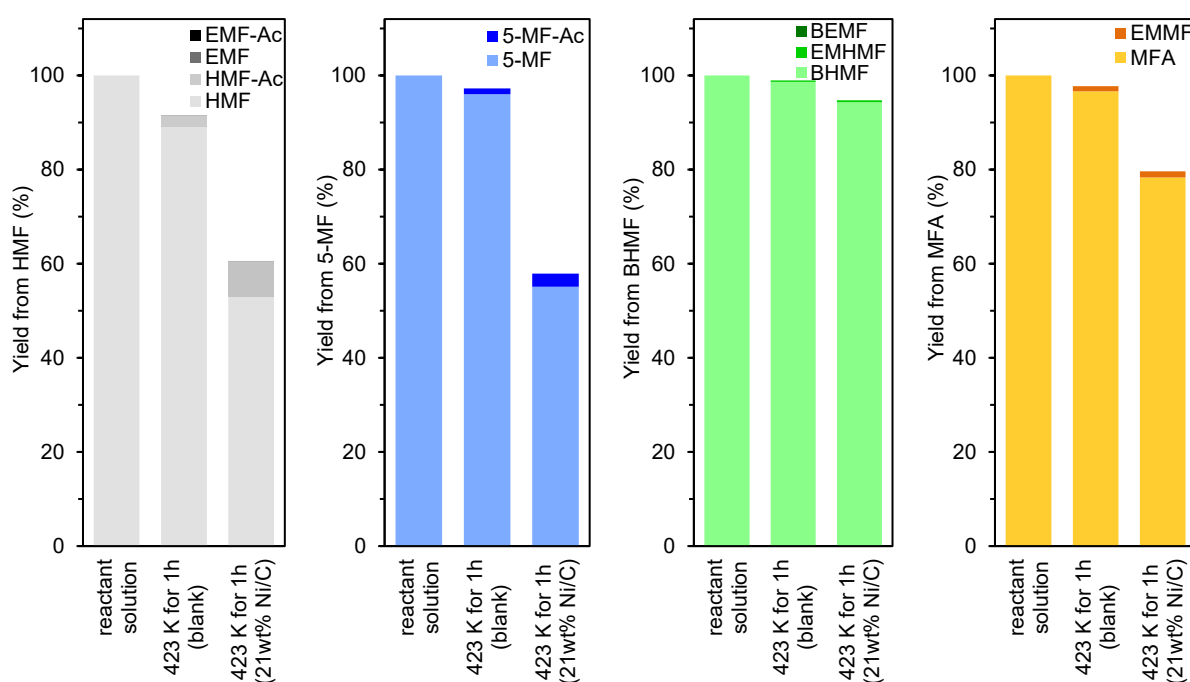


**Figure 5-12:** Reaction of HMF, 5-MF, BHMF, and MFA in ethanol solution and absence of  $H_2$ . Initial concentration 14 mL reactant solution: 25 mmol  $L^{-1}$  in HMF, 5-MF, BHMF, and MFA in ethanol. Conditions: 1.12  $g_{cat}$  (0.23  $g_{Ni}$ ), 1 h reaction time at 150 °C (equivalent to space time of 1.33 h  $g_{Ni} g_{HMF}^{-1}$  in continuous flow hydrogenation)

As shown in Figure 5-12 (left), a considerable fraction of HMF is converted to HMF-Ac in the uncatalyzed system and – to a much higher extent – in the presence of the Ni/C catalyst, whereas the formation of EMF and EMF-Ac remain on negligible level. This trend is in accordance with the observed initial increase of HMF-Ac in the hydrogenation experiment presented in Figure 5-11, which indicates that a large fraction of HMF undergoes primary acetalization. To estimate the contributions of the parallel HMF conversion routes, the yields of the four possible consecutive intermediates 5-MF, BHMF, HMF-Ac, and EMF are compared at the lowest space

time measured ( $0.11 \text{ h g}_{\text{Ni}} \text{ g}_{\text{HMF}}^{-1}$ ). At low conversion, their yields  $Y_i(\tau)$  are approximately proportional to their formation rates  $r_i^f$ , according to the following equation:

$$Y_i = \int r_i^f d\tau \stackrel{x_0 \approx 0}{\approx} r_i^f(\tau_0) \tau_0, \quad \tau_0 = 0.11 \text{ h g}_{\text{Ni}} \text{ g}_{\text{HMF}}^{-1} \quad (5.8)$$

The high yield of HMF-Ac (6.5%), in comparison to the other three intermediates (2.8% total) listed in Table 5-1, confirms that the HMF conversion proceeds in major part *via* acetalization of HMF. It proves the dominance of the acetal formation with subsequent hydrogenolysis over initial reductive steps and ether formation.

**Table 5-1:** Yields of four intermediates of HMF conversion over 21wt% Ni/C ( $2.4 \times 3.5 \text{ mm}$ ) at lowest space time ( $0.11 \text{ h g}_{\text{Ni}} \text{ g}_{\text{HMF}}^{-1}$ ). Conditions: 0.1M HMF in EtOH reactant solution,  $150^\circ \text{C}$ , 20 bar  $\text{H}_2$  pressure,  $\text{H}_2\text{:HMF}$  7.5:1.

	5-MF	BHMF	HMF-Ac	EMF
<b>Initial yield [%]</b>	0.8	1.9	6.5	0.1

According to the third diagram from the left in Figure 5-12, BHMF is inert to etherification towards EMHMF and BEMF. However, EMHMF exhibits a high transient yield of up to 21% in the hydrogenation experiment of Figure 5-11, which is therefore likely to be the result of hydrogenolysis of the as-formed HMF-Ac. This hypothesis is supported by the space time shift of the concentration maxima of the two compounds. Although traces of BEMF are observed in the catalytic system, it only reaches yields of  $\ll 1\%$  and is therefore not expected to be a major product of EMHMF conversion. Instead, a small share of EMHMF undergoes hydrolysis towards BHMF, which would explain the late increase of BHMF concentration despite the low HMF concentration – in addition to the initial increase due to primary carbonyl reduction of the HMF.

Subsequent deoxygenation of the two hydroxymethyl groups of BHMF yields the product DMF. Alternatively, the hydroxymethyl group of EMHMF can be deoxygenated, producing EMMF, which is in accordance with its concentration maximum over space time slightly after EMHMF. In addition, EMMF can also be produced via hydrogenolysis of 5-MF-Ac, which, in turn, derives from HMF by acetalization of the formyl group and deoxygenation of the hydroxy group, passing either through 5-MF or HMF-Ac as intermediates. Subsequently, EMMF is likely to undergo direct hydrogenolysis towards DMF.

To set the focus on the reductive steps of the reaction network, the derivatives of the furanic aldehydes and alcohols are grouped together, *i.e.* “HMF derivatives” (HMF-Ac, EMF, and EMF-Ac), “5-MF + derivatives” (5-MF and 5-MF-Ac), “BHMF + derivatives” (BHMF, EMHMF, and

BEMF), and “MFA + derivatives” (MFA and EMMF). In Figure 5-13, the DMF selectivity and Ni time yield (NTY) are plotted over space time. Furthermore, the selectivity and Ni time yield of the intermediates as well as the two observed consecutive products DMTHF – produced by overhydrogenation – and hexanedione (HD) – produced by DMF hydrolysis – are included in this figure.

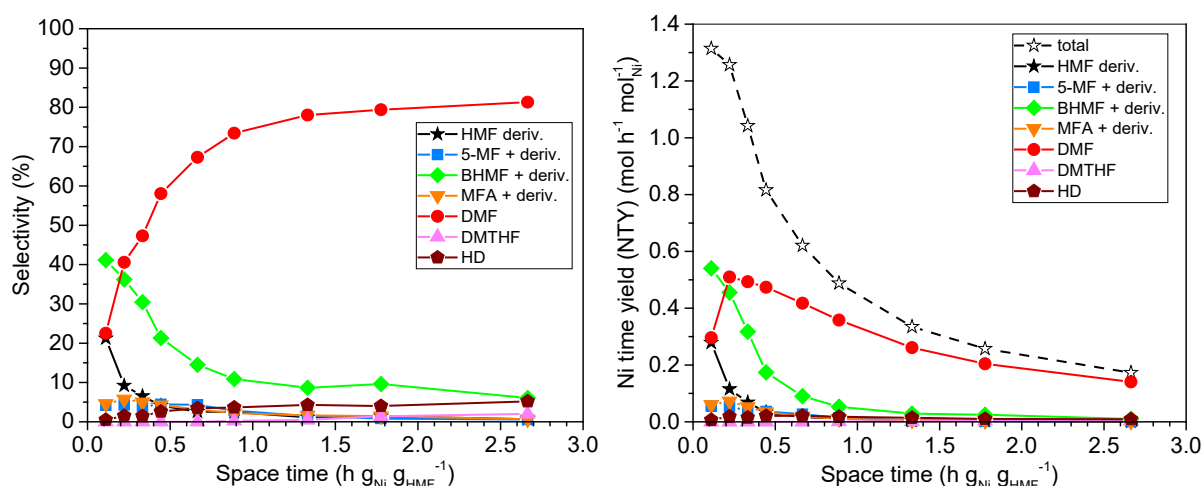


**Figure 5-13:** Effect of space time on selectivity (**left**) and Ni time yield (**right**) in HMF hydrogenation. Conditions: 0.1M HMF in EtOH reactant solution, 21wt% Ni/C (2.4 × 3.5 mm), 150 °C, 20 bar H<sub>2</sub>, H<sub>2</sub>:HMF 7.5:1

Regarding the DMF selectivity of 81.3% (99.0% HMF conversion), achieved for a long exposure to the catalyst of 2.66 h g<sub>Ni</sub> g<sub>HMF</sub><sup>-1</sup>, in contrast to 2.0% selectivity for the subsequent saturation of the furanic ring towards DMTHF, the 21% Ni/C pellets exhibit excellent catalytic properties for the selective hydrodeoxygenation of HMF. Longer space times would not be beneficial as they favor the undesired consecutive reactions towards DMTHF and HD (5.1% at 2.66 h g<sub>Ni</sub> g<sub>HMF</sub><sup>-1</sup>), which proceed slowly, but are gradually increasing over space time. The maximum Ni time yield obtained for DMF production is 0.51 mol<sub>DMF</sub> h<sup>-1</sup> mol<sub>Ni</sub><sup>-1</sup> (±0.84 g<sub>DMF</sub> h<sup>-1</sup> g<sub>Ni</sub><sup>-1</sup>) with 59.9% HMF conversion, whereas at a higher space time of 1.8 h g<sub>Ni</sub> g<sub>HMF</sub><sup>-1</sup>, a Ni time yield of 0.21 mol<sub>DMF</sub> h<sup>-1</sup> mol<sub>Ni</sub><sup>-1</sup> (±0.35 g<sub>DMF</sub> h<sup>-1</sup> g<sub>Ni</sub><sup>-1</sup>) is achieved with 98.2% HMF conversion and 79.4% DMF selectivity.

After an induction period of *ca.* 5 h, the catalyst exhibits high stability in terms of HMF conversion within the complete operation period of 35 h time on stream (thereof 33 h monitored in Figure 5-14). At 150 °C, 20 bar H<sub>2</sub> pressure, and space time of 1.33 h g<sub>Ni</sub> g<sub>HMF</sub><sup>-1</sup>, HMF conversion remains relatively stable, reaching values between 95.5% and 97.3%. However, the DMF selectivity of 78.0% (95.9% HMF conversion) at 5 h time on stream, providing a Ni time yield of 0.26 mol<sub>DMF</sub> h<sup>-1</sup> mol<sub>Ni</sub><sup>-1</sup>, drops down to 66.7% (96.3% HMF conversion) within a period of 12 h due to inhibited conversion of BHMF and EMMF.

Regarding the subsequent stabilization of the product distribution until termination of the experiment, the preceding decrease in conversion of “BHMF + derivative” is not attributed to a gradual deactivation of the active metal species, which would likely cause gradual drop in activity over the whole range of operation time. In fact, the trend of BHMF and EMHMF yield over time on stream proceeds inversely to the trend of HD yield, as can be seen in Figure 5-14 (right). As discussed in detail in the following paragraph, the hydrolysis of DMF to HD, on the other hand, is catalyzed by acids<sup>104</sup>, suggesting initial presence of acid sites on the carbon support and gradual deactivation of the active sites within the first 17 h of operation.

Confirming the hypothesis of decreasing acidic properties of the catalyst surface over time on stream, Böhm titration reveals a loss of acid sites of the 21wt% Ni/C from 0.48 eq kg<sup>-1</sup> to 0.43 eq kg<sup>-1</sup> over 35 h of operation, as calculated and described in detail in Appendix A.2.2.8. Regarding the oxygen content of 10wt% that has been measured for the carbon support, the material is likely to possess oxygen-containing acid surface sites which are commonly found on activated carbon<sup>105</sup>. However, the effect of acidity is also attributed to the presence of traces of Lewis-acidic Zn species as residues from the preparation step of the support, in which ZnO was employed as the porogenic templating agent. Even though the catalyst only lost 8% of its initial acidity during the catalytic operation according to the Böhm titration in Appendix A.2.2.8, it is presumed that predominantly the more accessible Zn species underwent leaching, which led to deactivation of the catalyst's acidity within the first 15 h time on stream.

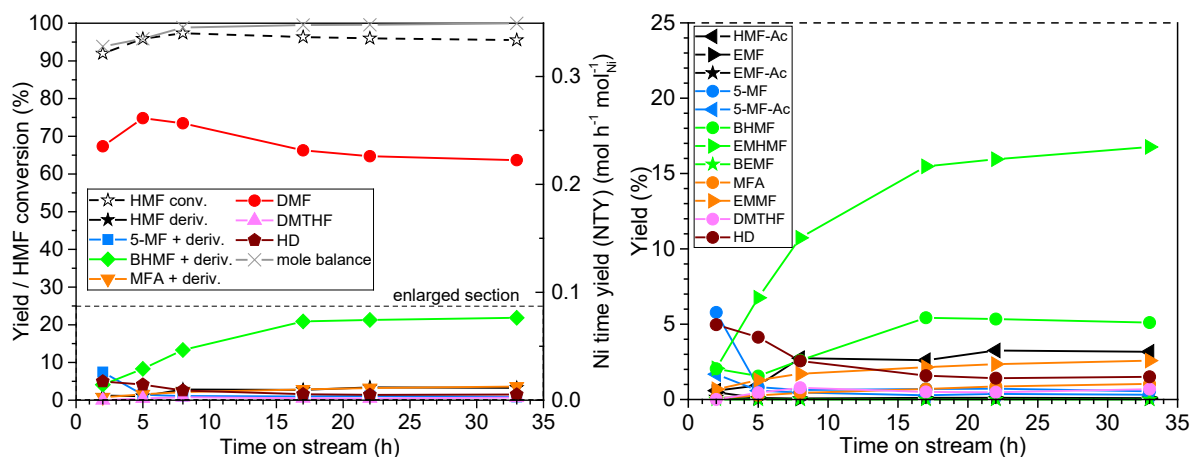


**Figure 5-14:** Time-on-stream evolution of yield and Ni space time in HMF hydrogenation. **left:** intermediate derivatives of same reduction level grouped together; **right:** derivatives displayed separately in enlarged diagram. Conditions: 0.1M HMF in EtOH reactant solution, 21wt% Ni/C (2.4 × 3.5mm), space time of 1.33 h g<sub>Ni</sub> g<sub>HMF</sub><sup>-1</sup>, 150 °C, 20 bar H<sub>2</sub> pressure, H<sub>2</sub>:HMF 7.5:1

The acid sites on the surface of the carbon pellets are capable of adsorbing the furanic oxygen and hydrolyzing the ring via dissociative proton transfer<sup>106</sup>. This acid-catalyzed ring scission primarily occurs on the furanic ring of DMF where no oxygen-containing side groups are present, which



would preferably be adsorbed<sup>106</sup>. On this pathway, the high observed yield of hexane-2,5-dione (HD; up to 5.0%) is produced. However, also BHMF can undergo acid-catalyzed ring opening to a low extent, yielding 1-hydroxy-2,5-hexanedione<sup>107</sup>. Both hydrolysates can undergo further hydrogenation steps towards several C<sub>6</sub> compounds, of which several compounds were detected in traces. As their formation appears only within the first few hours of time on stream and is therefore of little importance for the catalytic system after the initial period, those products are not quantified in this work, which is the reason for the incomplete mole balance during the first few hours, calculated by the sum of all quantified compounds (incl. the reactant) and represented by the grey line in Figure 5-14 (left). As for all further measurements the mole balance closes to 96-100%, it is not shown in all other diagrams for the sake of clarity.

In several studies on the HMF hydrodeoxygenation over several metal-based catalysts (in non-alcoholic solvents that do not engage in parallel condensation reactions with the reactant), the deoxygenation of BHMF is identified as the rate determining step since the deoxygenation of the formyl group generally proceeds slowly, favoring the hydrogenation of HMF towards BHMF over the parallel branch of deoxygenation towards 5-MF.

However, the deoxygenation of BHMF and its ethers is known to be promoted by the presence of acidic sites on bifunctional catalysts<sup>106,108</sup>, which explains the very low initial yield of the diol and its ether, as shown in Figure 5-14 (right), followed by a steady increase along advancing deactivation of acid sites over time on stream, and finally resulting in a period of stabilized concentration after the catalyst has lost its bifunctional character. As has been stated in the literature, Zn<sup>2+</sup> species on the surface of activated carbon are capable of adsorbing ether and hydroxy groups and inducing deoxygenation reactions via hydrogen spillover in cooperation with adjacent metal sites, such as Pd, Ru, and Ni<sup>108,109</sup>.

The increased conversion of the furanic alcohols and ethers with concurrent increased DMF yield observed in Figure 5-14 during the acidic operation period strongly support the assumption of acid-promoted deoxygenation of the hydroxy groups. Interestingly, the gradual decrease of initial acidity of the catalyst leads to a temporary maximum in DMF selectivity of 73.3% at 5-8 h TOS. Prior to the maximum, the acidity, which promotes the cleavage of the furanic ring of DMF towards HD, appears to be too strong. On the other hand, after the DMF maximum, the acidity drops to a level that does not effectively promote the rate determining steps of BHMF and EMHMF conversion anymore. This instance gives an indication that mild acidity of the catalyst on a controlled level can be very favorable to the reaction, while still not substantially affecting



the product selectivity through catalyzed consecutive hydrolysis reactions, facilitated by *in situ* formed water, according to equation (5.9).

Furthermore, by promoting the deoxygenation of the hydroxy groups of HMF and BHMF, the acidic properties of the catalyst effectively turn the hydrogenation of 5-MF into the kinetically slower step, albeit for a very temporary period of only a few hours before the extensive deactivation of the acid sites. This causes an increased 5-MF yield of up to 5.8% (7.5% incl. 5-MF-Ac) with concurrent low BHMF yield of 2.0% (4.1% incl. EMHMF), which is only encountered at the very beginning of the catalyst's lifetime.

According to the overall stoichiometric equation of HMF hydrodeoxygenation to DMF:



a minimum factor of 3 is needed for the molar hydrogen gas feed under stoichiometric conversion of HMF. However, when setting the feed stream to a H<sub>2</sub>:HMF molar ratio of only 3:1, not enough hydrogen is provided and the hydrogenation reaction is strongly inhibited, as can be seen in Figure 5-15 (right). As in the outlet of the set-up a hydrogen flow rate of almost 50%, compared with the inlet hydrogen flow rate, was measured, the introduced hydrogen is certainly not completely consumed. Accordingly, the decrease in hydrogenation activity is caused by insufficient chemisorption onto the active metal surface.

Furthermore, a slightly increased concentration of acetaldehyde acetal (5.1 mmol L<sup>-1</sup>, which is equivalent to 5.1% of the introduced HMF concentration of 100 mmol L<sup>-1</sup>), denoted as “acetal” in Figure 5-15 (right), is observed in the product stream. As acetal is produced via oxidation of ethanol towards the aldehyde and subsequent acetalization, this indicates that, to a low extent, the shortage of available hydrogen triggers transfer hydrogenation with the solvent acting as a reducing agent. The increased 5-MF concentration and concurrent decreased BHMF concentration suggest that the hydrogenation of the formyl group is particularly sensitive to limited hydrogen supply, indicating a higher partial order in hydrogen for the carbonyl reduction.

When increasing the hydrogen supply towards an excess factor of 1.5 (H<sub>2</sub>:HMF molar ratio of 4.5:1) at constant space time, the reactivity is slightly improved, whereas an excess factor of at least 2.5 (H<sub>2</sub>:HMF = 7.5:1) is necessary for maximum activity. Regarding the constant low acetal concentration of 3.4 mmol L<sup>-1</sup> under hydrogen-saturated conditions, transfer hydrogenation is not expected to have a strong influence on the reduction of the reactant. Since chemisorbed hydrogen

is sufficiently available at this point, further increase of the hydrogen flow hardly improves the reactivity and is therefore not necessary.

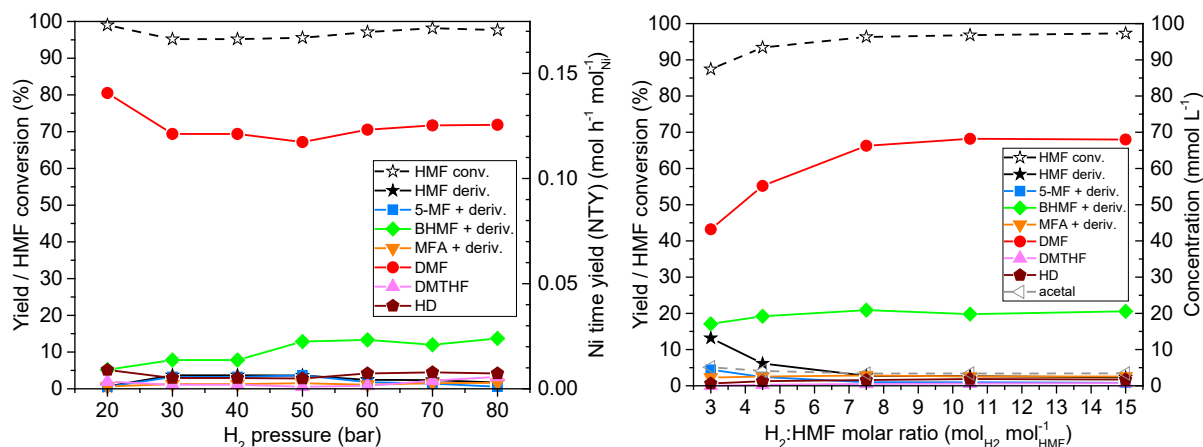


**Figure 5-15:** Effect of H<sub>2</sub> pressure (**left**) and H<sub>2</sub>:HMF molar ratio (**right**) on yield and Ni time yield in HMF hydrogenation. Conditions: 0.1M HMF in EtOH reactant solution, 21wt% Ni/C pellets (2.4 × 3.5mm), 150 °C, space time of 2.66 (**left**) and 1.33 (**right**) h g<sub>Ni</sub> g<sub>HMF</sub><sup>-1</sup>, H<sub>2</sub>:HMF 7.5:1 (**left**), 20 bar H<sub>2</sub> (**right**)

Interestingly, at H<sub>2</sub>:HMF = 7.5:1, H<sub>2</sub> pressure higher than 20 bar did not increase the reactivity, as shown in Figure 5-15 (left), indicating that the reaction proceeds in a partial order of 0 in hydrogen. Quite on the contrary, operation at 20 bar provides the highest DMF yield of 80.5% (99.0% HMF conversion), while operation in the range from 30 to 80 bar delivers yields on a stable level between 67.2% and 71.9%. It is hypothesized that this trend is caused by the increased hydrogen adsorption onto the metal surface at high pressure to such an extent that it is displacing the adsorption and reaction of the reactant and intermediates, especially of BHMf and EMHMF, which are more abundant at the higher pressure range.

According to Figure 5-16, a decrease of reaction temperature inhibits the hydrogenolysis of HMF-Ac as well as the conversion of BHMf and EMHMF, leading to very low DMF yield of down to 25.6% at 110 °C for a space time of 1.33 h g<sub>Ni</sub> g<sub>HMF</sub><sup>-1</sup>, while HMF conversion remains on a high level of 93.7%.

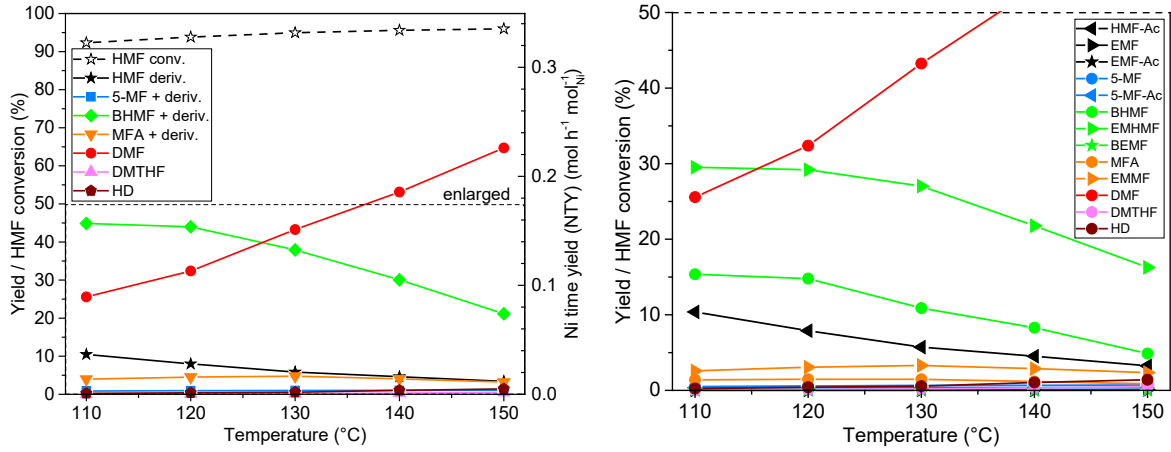


**Figure 5-16:** Effect of temperature on yield and Ni time yield in HMF hydrogenation. **left:** derivatives of same reduction level grouped together; **right:** derivatives displayed separately in enlarged scale of low yield. Conditions: 0.1M HMF in EtOH reactant solution, 21wt% Ni/C pellets ( $2.4 \times 3.5$ mm), space time of  $1.33 \text{ h g}_{\text{Ni}} \text{ g}_{\text{HMF}}^{-1}$ , 20 bar  $\text{H}_2$ ,  $\text{H}_2$ :HMF 7.5:1

Due to the complex reaction network and the fact that differential kinetic behavior cannot be observed at such high conversions, exact calculation of the intrinsic activation energy is not possible based on the produced results. However, a calculation of an approximate value for the activation energy based on an integral approach is presented in the following. This model uses the following simplifications: Due to the fast and almost complete consumption of HMF and HMF-Ac, their further conversion is neglected. In addition, all side reactions apart from the two main branches are neglected, resulting in two separate unbranched reaction pathways of  $\text{BHMF} \rightarrow \text{MFA} \rightarrow \text{DMF} \rightarrow \text{DMTHF/HD}$  on the one hand and  $\text{EMHMF} \rightarrow \text{EMMF} \rightarrow \text{DMF} \rightarrow \text{DMTHF/HD}$  on the other hand, in which the consumption of BHMF and EMHMF are assumed to be the respective rate determining steps. To estimate the conversion of the two compounds BHMF and EMHMF, their yields are transformed into a model system for conversions  $X_i^h$  of these compounds as “hypothetical” reactants, according to the following equations:

$$X_{\text{BHMF}}^h = 1 - \frac{Y_{\text{BHMF}}}{Y_{\text{BHMF}}^{\text{cu}}} , \quad X_{\text{EMHMF}}^h = 1 - \frac{Y_{\text{EMHMF}}}{Y_{\text{EMHMF}}^{\text{cu}}} \quad (5.10)$$

in which the  $Y_i^{\text{cu}}$  represent “cumulative” yields, including all intermediates and products that have been produced in the HMF hydrogenation experiment on either of the pathways, passing through BHMF or EMHMF. They can be regarded as integrated formation rates and are connected to their differential terms by:

$$dY_i^{\text{cu}} = r_i^f d\tau \quad (5.11)$$

The cumulative yields can be calculated by:

$$Y_{BHMF}^{cu} = Y_{BHMF} + Y_{MFA} + z \cdot (Y_{DMF} + Y_{DMTHF} + Y_{HD}) \quad (5.12)$$

$$Y_{EMHMF}^{cu} = Y_{EMHMF} + Y_{EMMF} + (1 - z) \cdot (Y_{DMF} + Y_{DMTHF} + Y_{HD}) \quad (5.13)$$

where  $z$  represents the fraction of products that have been formed on the BHMF branch. This factor is estimated by the ratio of present intermediates of the two pathways:

$$z = \frac{Y_{BHMF} + Y_{MFA}}{Y_{BHMF} + Y_{MFA} + Y_{EMHMF} + Y_{EMMF}} \quad (5.14)$$

The transformed hypothetical conversions, shown versus temperature in Figure 5-17 (left), are remarkably similar for BHMF and EMHMF, suggesting that their consumption via hydrogenolysis involves very comparable kinetics. In order to estimate the apparent activation energy of the hydrogenolysis reaction, first, Arrhenius behavior of the rate coefficient is assumed:

$$k(T) = A e^{-\frac{E_a}{RT}} \quad (5.15)$$

Rearrangement into point-slope form yields the following term for the activation energy:

$$E_a = -R \frac{\Delta \ln k(T)}{\Delta(T^{-1})} \quad (5.16)$$

As this temperature study is not conducted in the low conversion range, proportionality between space time and conversion cannot be implied. Instead, when assuming a partial order of 0 in hydrogen and 1 in the concentration of BHMF and EMHMF, respectively, the consumption rate can be expressed by:

$$r_i = k_i(T) C_i = k_i(T) C_{i0} (1 - X_i^h), \quad i = BHMF, EMHMF \quad (5.17)$$

in which “0” constitutes the hypothetical start of the reaction. The rate expression leads to the differential balance of the molar flow:

$$dX_i^h = k_i(T) C_{i0} (1 - X_i^h) \frac{dm_{Ni}}{\dot{N}_{i0}} \quad (5.18)$$

Integration over space time in its common definition  $\tau = m_{Ni}/\dot{N}_{i0}$  along the reactor axis provides the following solution for the hypothetical conversion:

$$\ln\left(\frac{1}{1-X_i^h}\right) = k_i(T) C_{i0} \tau \quad (5.19)$$

Accordingly, the activation energy can be calculated from the conversion in the temperature range of 110 to 150 °C by linear regression from the following expression, as shown in Figure 5-17 (right):

$$E_{a,i} = -R \frac{\Delta \ln k_i(T)}{\Delta(T^{-1})} = -R \frac{\Delta \ln\left(\ln\left(\frac{1}{1-X_i^h}\right)\right)}{\Delta(T^{-1})} \quad (5.20)$$

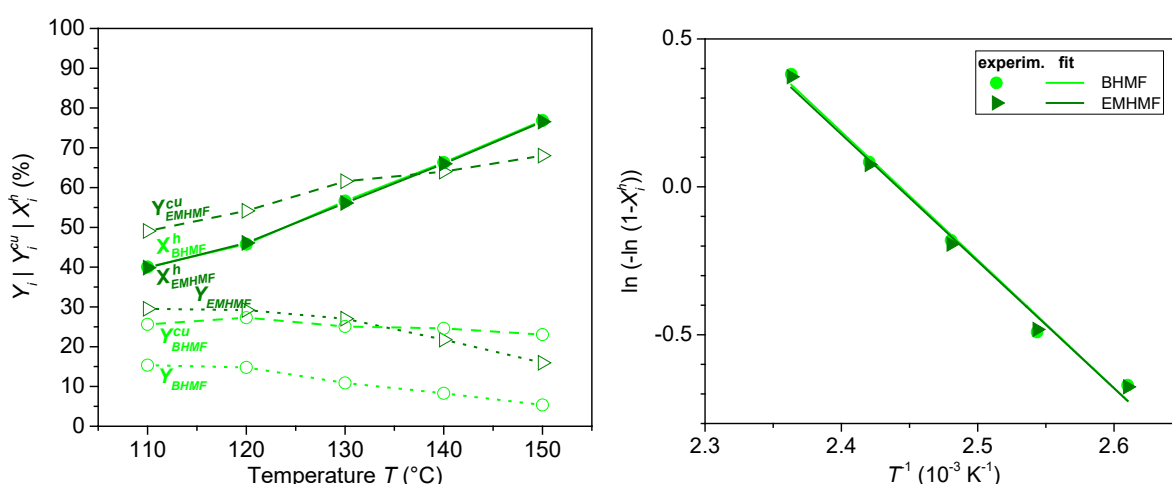


**Figure 5-17:** Yield, cumulative yield, and hypothetical conversion of BHMf and EMHMF over temperature. Conditions according to Figure 5-16

Eventually, from the linear regression, the apparent activation energy for the hydrogenolysis of BHMf and of EMHMF is calculated to 36.0 and 35.7 kJ mol<sup>-1</sup>, respectively.

As has been shown, the predominant hydrogenation routes involve chemical reactions with ethanol, influencing the activity of the overall reaction in several ways. On the one hand, ethanol as a reactive solvent accelerates the consumption of HMF *via* acetal formation at the carbonyl group, while on the other hand, the ethoxy groups seem to act as protecting groups at least to some extent, slightly inhibiting the further reduction step. However, both the hydrogenolysis of the ethoxymethyl group and the deoxygenation of the hydroxymethyl group proceed slowly on a similar level in absence of an acid catalyst and constitute the rate determining step for the respective pathway.

Interestingly, the formation of the *cis* isomer of DMTHF is very dominant (>95%) over the production of the *trans* isomer. This stereoselective reaction is attributed to the fact that after

adsorption of the planar furanic species to the metal surface and the subsequent hydrogenation step, the as-formed dihydrofuran ring is reactive on such a high level that the residual double bond residing at the metal surface is likewise saturated before the molecule can desorb and re-adsorb from the other side<sup>110,111</sup>.

Although some studies suggest the possibility of an alternative pathway to the formation of DMTHF, involving hydrogenation of HD to hexane-2,5-diol (HDL) and further intramolecular condensation to DMTHF<sup>112,113</sup>, as illustrated in Figure 5-18, it is not believed to be the main cause of DMTHF formation in this work due to the assumed low acidity in the present catalyzed system after several hours of time on stream. Moreover, even though this alternative route can also proceed stereoselectively towards *cis*-DMTHF, which can cause a preferential orientation of the chiral centers at the hydroxy groups of HDL, the *cis* selectivity remains below 90%<sup>113</sup>. The extent of *cis* selectivity depends on the type of acid catalyst<sup>113</sup>, but is in any case lower than the nearly complete *cis* selectivity (<95%) observed in the present work and other works in which direct furanic ring saturation of DMF is reported<sup>110</sup>.

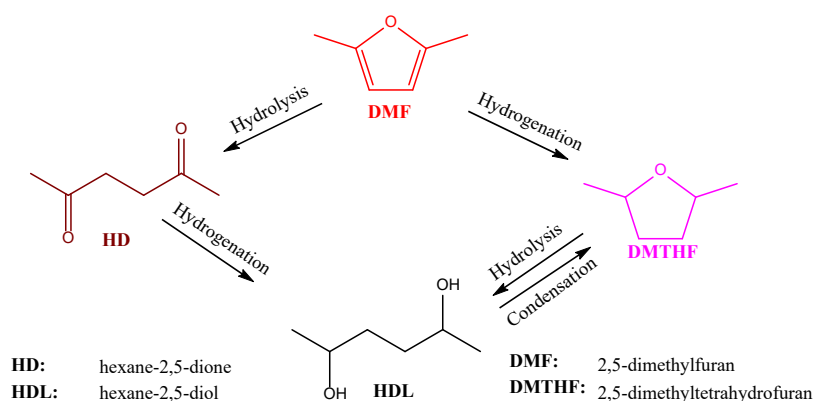


**Figure 5-18:** Possible pathways for the formation of DMTHF and hexane-2,5-diol from DMF

According to N<sub>2</sub> physisorption analysis, the 21wt% Ni/C catalyst exhibits hardly any change of the porous structure over the whole operation period of 35 h time on stream. As can be seen from Figure 5-19, the N<sub>2</sub> adsorption behavior and, accordingly, the pore size distribution determined from QSDFT on the adsorption branch, are very congruent.

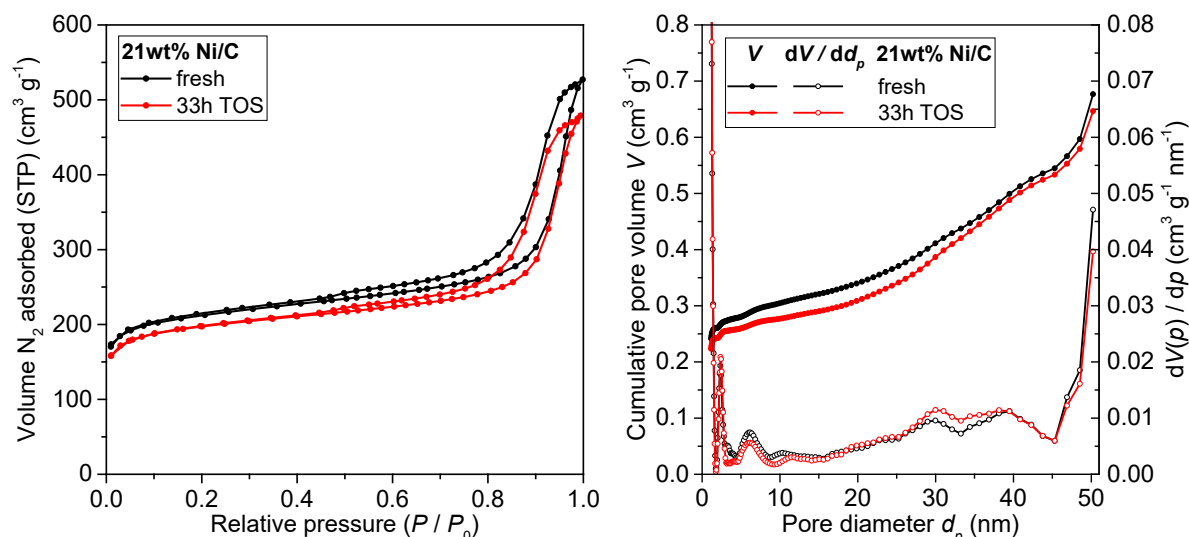


**Figure 5-19:** N<sub>2</sub> physisorption isotherms (**left**) and pore size distribution (**right**) of the 21wt% Ni/C catalyst before reaction and after 35 h time on stream. Measurements conducted at 77.3 K. Calculation of pore size distribution based on QSDFT adsorption method on carbon with slit, cylindrical, and spherical pores.

Furthermore, the total pore volume and surface area in the micro- to mesoporous range remained nearly constant, exhibiting very little decrease from 0.64 to 0.62 cm<sup>3</sup>/g and 805 to 758 m<sup>2</sup>/g, respectively, as summarized in Table 5-2. This is in accordance with the stable catalytic activity that has been observed within the whole window of operation time, as previously presented in Figure 5-15 (right).

It should be mentioned that the 35 h TOS specimen for the N<sub>2</sub> physisorption measurement consisted of a mixture of pellets that had previously been randomly distributed along the reactor axis during catalytic operation and, therefore, represent average characteristics of the used catalyst pellets that might exhibit gradients in their properties, as the involvement in catalytic reactions - and therefore the influence on potential erosion - of the material is dependent on the location inside the reactor. However, the unaltered porosity of the average specimen indicates that erosion doesn't occur anywhere in the reactor to a considerable degree.

**Table 5-2:** Nitrogen physisorption data of the 21wt% Ni/C catalyst before reaction and after 35 h time on stream of HMF hydrodeoxygenation reaction in EtOH.

Sample	Pore volume [cm <sup>3</sup> /g]				Specific surface area [m <sup>2</sup> /g]				Average pore size [nm]
	QSDFT adsorption			BJH ads.  Total	QSDFT adsorption			BET  Total	
	Micro	Meso	Total		Micro	Meso	Total		
	< 2 nm	2-50nm	≤ 50nm		≤ 500nm	< 2 nm	2-50nm		≤ 50nm
21wt% Ni/C									
fresh	0.26	0.38	0.64	0.82	697	108	805	804	4.1
35 h TOS	0.24	0.38	0.62	0.76	651	107	758	757	4.0

To examine the effect of Ni loading on the catalytic activity, in a further experiment, both Ni loading of the catalyst and HMF concentration of the reactant solution is reduced, compared with the previous experiment, to facilitate operation with similar volumetric flow rates of the reactant inside the reactor. In Figure 5-20, the product composition from a 0.05M HMF reactant solution is shown versus space time (left) and temperature (right), using a 16wt% Ni loading on the pelletized carbon support. Trends similar to the results over the previously presented 21wt% Ni/C catalyst with a 0.1M HMF solution (previously presented in Figure 5-11 for space time and Figure 5-16 for temperature) are observed. However, particularly at lower space time, the catalytic system with the 21wt% Ni/C performs better in terms of product yield, whereas the results seem to align for high space time.

Several aspects are assumed to contribute to the observed difference in activity, all connected to the dispersion of the flow of reactant solution inside the reactor. First, the voids between the catalyst pellets of the 21wt% Ni/C reactor were filled with sea sand (as presented in section 4.2), which has not been done for the 16wt% Ni/C reactor. Second, the lower reactant concentration in the experiment with the 16wt% Ni/C reactor (0.05 mol L<sup>-1</sup>, compared with 0.1 mol L<sup>-1</sup> in the 21wt% Ni/C experiment) reduces the residence time of the solution inside the reactor at the same space time (referring to the weight of Ni), which is assumed to amplify the effect of unreacted solution bypassing the catalyst pores through the void channels. In addition, it is assumed that the higher hydrogen gas feed in the 16wt% Ni/C experiment (H<sub>2</sub>:HMF molar ratio of 15:1, compared with 7.5:1 in the 21wt% Ni/C experiment) intensifies this effect by increasingly displacing the liquid solution and, therefore, rapidly pushing the unreacted solution through the reactor without providing intensive contact with the catalyst.

In contrast, for the 21wt% Ni/C experiment, increase of the hydrogen gas feed to a H<sub>2</sub>:HMF molar ratio of 15:1 did not affect the product composition, compared to 7.5:1, as shown earlier in



Figure 5-15 (right). This instance proves the effective prevention of a trickle flow and reduction of axial dispersion of the solution inside the reactor by closing the large void channels of the catalyst bed with sand.

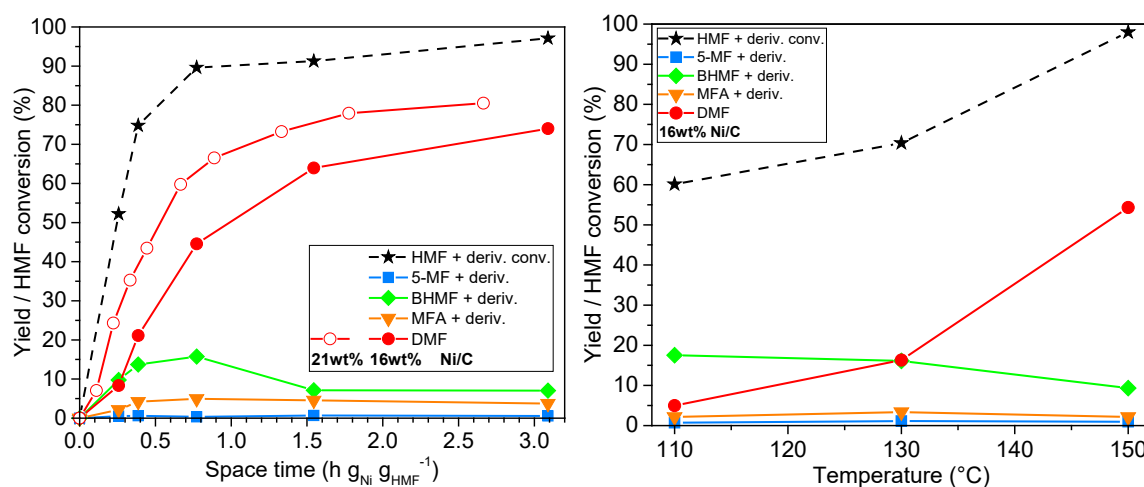


**Figure 5-20:** Effect of space time (**left**) and temperature (**right**) on conversion and yield in HMF hydrogenation over 16wt% Ni/C catalyst pellets ( $2.4 \times 3.5$ mm). Conditions: 0.05M HMF in EtOH reactant solution, 20 bar H<sub>2</sub>, H<sub>2</sub>:HMF 15:1; **left**: 150 °C, compared to DMF yield over 21wt% Ni/C from 0.1M HMF solution with H<sub>2</sub>:HMF 7.5:1; **right**: space time of 0.77 h g<sub>Ni</sub> g<sub>HMF</sub><sup>-1</sup>

The 16wt% Ni/C catalyst exhibits very high sensitivity to temperature in the conducted temperature study presented in Figure 5-20 (right). Increase in temperature from 110 to 150 °C enhances the DMF yield from 5.0% to 54.3%, using a low space time of 0.77 h g<sub>Ni</sub> g<sub>HMF</sub><sup>-1</sup> and 20 bar H<sub>2</sub> pressure. The high concentration of the intermediate BHMF and its ether derivative EMHMF along with very low concentrations of 5-MF and 5-MF-Ac reveal the conversion of BHMF and its derivate as the kinetically limiting steps and confirm the trend previously observed for the 21wt% Ni/C catalyst.

After 35 h of time on stream, the Ni loading of the catalyst with an initial loading of 21wt% Ni decreased to 17wt%. The 16wt% Ni/C variant undergoes a decrease in Ni loading to a similar degree, exhibiting 13wt% after 30 h time on stream. Accordingly, leaching of the metal particles is a main cause of the observed mild deactivation, provoked by the fact that Ni is slightly above hydrogen in the activity series of metals and is therefore prone to leaching under acidic conditions<sup>114</sup>.

**Table 5-3:** Ni loading of 21 and 16wt% Ni/C before and after HMF hydrogenation reaction in EtOH. *a*: measured by inductively coupled plasma (ICP)

Sample	Ni weight fraction <sup>a</sup> [wt%]	
	fresh	used
<b>21wt% Ni/C</b>	21.3 ±1	17.2 ±1 (35 h TOS)
<b>16wt% Ni/C</b>	16.4 ±1	13.4 ±1 (30 h TOS)

In addition, for the 21wt% Ni/C catalyst, an increase in average crystallite and particle size due to Ostwald ripening can be observed. With the mean crystallite size increasing from 29 to 35 nm over 35 h TOS of HMF hydrogenation in EtOH, as calculated from the XRD diffractogram and presented in Table 5-4, the diminishing metal dispersion is assumed to also contribute to the catalyst deactivation, albeit not to a large extent since only low decrease in activity was observed over the whole operation period, as previously presented in Figure 5-14.

**Table 5-4:** Ni crystallite size of the 21wt% Ni/C catalyst before and after 35 h TOS of HMF hydrogenation in EtOH; *a*: determined as average value of three mean crystallite sizes calculated from the three main peaks in the XRD diffractogram

Sample	Crystallite size <sup>a</sup> [nm]
<b>21wt% Ni/C</b>	
fresh	29 (Ni <sup>0</sup> )
35 h TOS	35 (Ni <sup>0</sup> )

## 5.3 Hydrogenation of Levulinic Acid

In this subchapter, the prepared Ni/C<sub>ZnO</sub> and Pt/C<sub>ZnO</sub> catalyst pellets are employed for the hydrogenation of LA. As the hydrogen source, both molecular hydrogen and formic acid are used.

### 5.3.1 External Molecular Hydrogen

For the direct hydrogenation of LA, hydrogen is continuously introduced into the reactant solution of 0.1M LA in water, providing a H<sub>2</sub>:LA molar ratio of 5:1, *i.e.* 5× the amount necessary for stoichiometric conversion of LA to GVL. To investigate the influence of temperature, the reaction is performed over a 2.7% Pt/C catalyst within a temperature range from 100 to 260 °C. LA conversion and yield and selectivity of products and intermediates are shown in Figure 5-21.

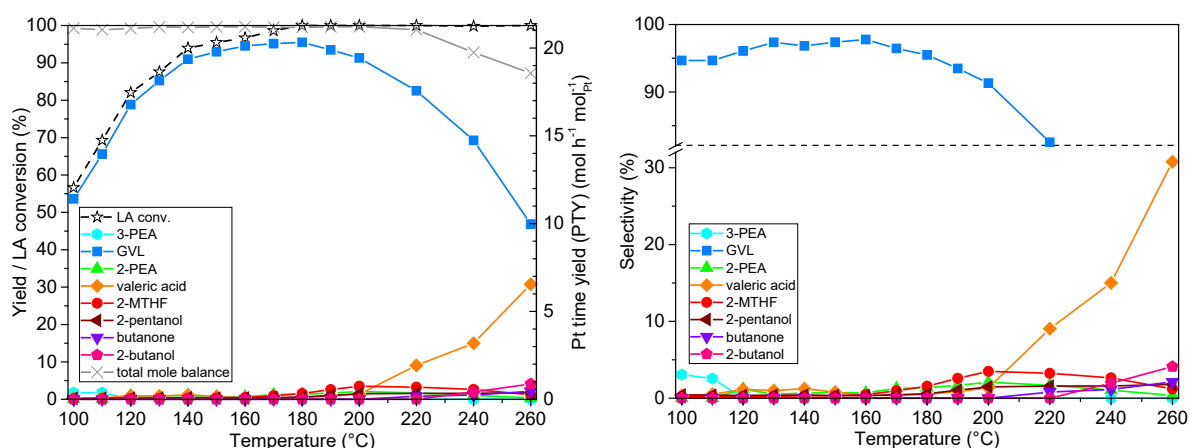


**Figure 5-21:** Effect of temperature on conversion, yield, and Pt time yield (**left**) as well as selectivity (**right**) in LA hydrogenation over 2.7wt% Pt/C (2.4 × 3.5mm). Conditions: 0.1M LA in H<sub>2</sub>O, space time of 0.079 h g<sub>Pt</sub> g<sub>LA</sub><sup>-1</sup>, 50 bar H<sub>2</sub>, H<sub>2</sub>:LA 5:1

Excellent GVL selectivity of >94% is observed in the range of 100 to 180 °C, with a maximum of 97.8% (95.2% LA conversion) at 160 °C, while LA conversion gradually increases from 56.6% at 100 °C towards complete conversion (>99.9%) at 180 °C. In the regime between 140 and 180 °C, a plateau of both high activity and high product stability is obtained, which offers optimum conditions for selective GVL production in high yield. As temperatures higher than 180 °C facilitate consecutive reactions of the product, further increase of reaction temperature decreases the GVL yield. At 240 and 260 °C, the gap in the total mole balance of quantified components suggests that low molecular gases are formed as a result of overhydrogenation of the C<sub>5</sub> species<sup>115</sup>.

The small fraction of 3-pentenoic acid (3-PEA) detected in the low temperature range of 100 to 120 °C with lower LA conversion indicates that the formation of GVL from LA passes through  $\gamma$ -hydroxyvaleric acid (GHVA) with subsequent dehydration to 3-PEA as intermediates, which is in

agreement to the findings of Al-Naji *et al.*<sup>81</sup>. As they were using supports with acid sites ( $\text{ZrO}_2$  and  $\gamma\text{-Al}_2\text{O}_3$ ), the dehydration step was promoted<sup>81</sup>, causing concentrations of 3-PEA higher than it is observed in the present work over the Pt/C catalyst with very low acidity. Owing to the fact that throughout all experiments 3-PEA was only detected at temperatures below 120 °C, the assumed ring closing mechanism subsequent to the dehydration step appears to proceed promptly at 120 °C and higher, thus 3-PEA is a transient state of direct ring condensation of GHVA towards GVL rather than a stable intermediate.

Since no traces of angelica lactones are detected at any point of the LA hydrogenation experiments in this work, a second possible pathway reported in the literature<sup>67</sup> for the GVL formation from LA *via* primary ring condensation to  $\alpha$ -angelica lactone (AAL) is expected to play a minor role. This is in agreement with the work of Abdelrahman *et al.*<sup>116</sup>, who reported that the presence of  $\text{H}_2$  strongly promotes the route of primary hydrogenation towards GHVA. However, it is hypothesized that the introduction of acid sites into the carbon support could strengthen the importance of this pathway by promoting the ring condensation step. Based on the obtained results in the present LA hydrogenation experiment, a reaction scheme is proposed in Figure 5-22, including the assumed consecutive reactions towards the observed byproducts that are discussed in the following.

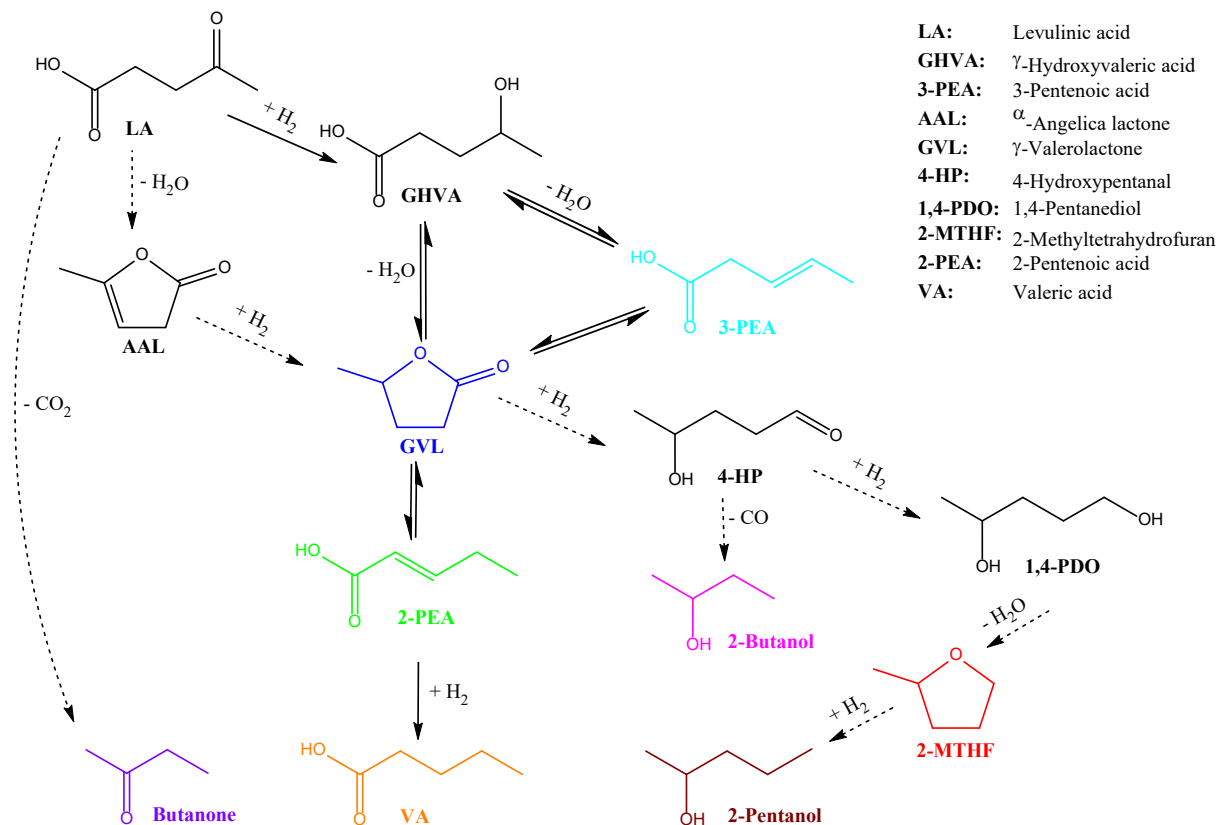


**Figure 5-22:** Suggested reaction scheme of LA hydrogenation, including parallel and consecutive reactions to byproducts

At high temperatures, valeric acid is identified as the main consecutive product, reaching a selectivity of up to 30.8% at 260 °C. It is likely to be formed *via* hydrogenation of 2-pentenoic acid (2-PEA), an open-ring isomer of GVL. The presence of 2-methyltetrahydrofuran (2-MTHF) at 180 °C and higher suggests hydrogenation of GVL towards 1,4-pentanediol (1,4-PDO), which undergoes intramolecular ring condensation to 2-MTHF, as reported by Al-Shaal *et al.*<sup>117</sup>. These intermediates can be further hydrogenated to 2-pentanol, which is also observed in high temperatures. On the other hand, 1,4-PDO can also be reduced to 4-hydroxypentanal (4-HP), which undergoes decarbonylation towards 2-butanol<sup>117</sup>, observed at 240 to 260 °C. Butanone, which is detected in low amounts at 220 °C and above, is assumed to be formed via hydrodecarboxylation of levulinic acid, as formation from the GVL is unlikely due to its keto group.

Since the highest GVL selectivity was observed at 160 °C, with only traces of the mentioned side products, the reaction at this temperature has been investigated over space time, as shown in Figure 5-23. With an observed maximum GVL yield of 96.4% (98.9% LA conversion), the optimum condition for this process is identified at a space time of 0.079 h g<sub>Pt</sub> g<sub>LA</sub><sup>-1</sup>.

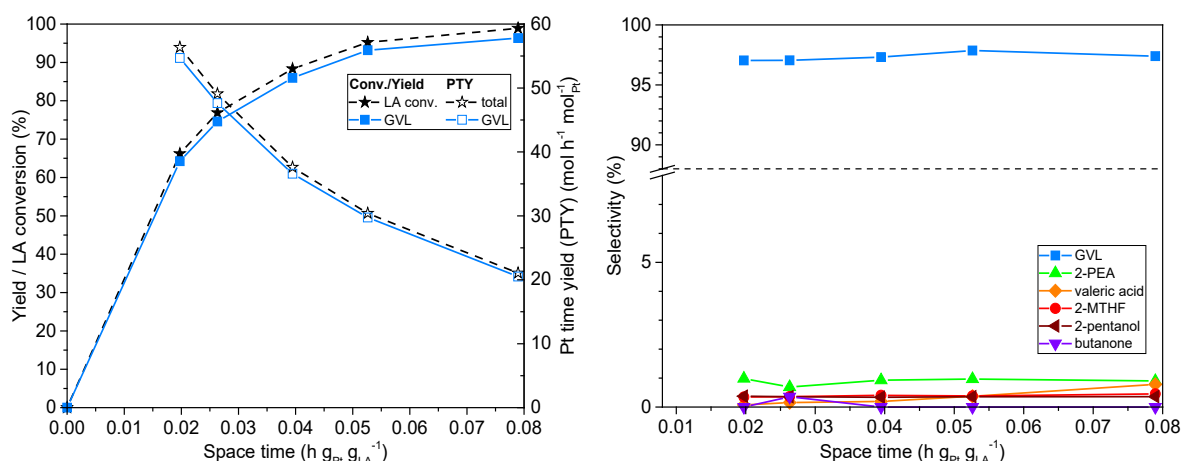


**Figure 5-23:** Effect of space time on conversion, yield, and Pt time yield of GVL (left) as well as selectivity (right) in LA hydrogenation over 2.7wt% Pt/C (2.4 × 3.5mm). Conditions: 0.1M LA in H<sub>2</sub>O, 160 °C, 50 bar H<sub>2</sub>, H<sub>2</sub>:LA 5:1

Due to the high GVL selectivity of the reaction below 180 °C, the kinetic parameters of the overall rate of GVL formation can be determined from the observed kinetics of LA conversion, with the first step of hydrogenation towards GHVA being the rate determining step. In analogy to the approach for the HMF hydrogenation in the previous subchapter, the activation energy is calculated under integral conditions from the LA conversion in the temperature range of 100 to 170 °C by linear regression.

The overall rate constant is calculated by linear regression of the first 4 points over space time, derived from the integrated mole balance over LA:

$$k_{LA}(160\text{ }^{\circ}\text{C}) = \frac{1}{C_{LA,0}} \frac{\Delta \ln\left(\frac{1}{1-X_{LA}}\right)}{\Delta \tau} \quad (5.21)$$

The fitted kinetic parameters of LA consumption are summarized in Table 5-5, including the pre-exponential factor  $A_{LA}$  that is determined from  $k_{LA}(160\text{ }^{\circ}\text{C})$  and  $E_{a,LA}$  by substitution.

**Table 5-5:** Arrhenius parameters fitted to the observed kinetics of LA consumption. Conditions as specified in Figure 5-23.

$k_{LA}(160\text{ }^{\circ}\text{C})$	$E_{a,LA}$	$A_{LA}$
$4.797 \frac{\text{L}}{\text{h g}_{\text{Pt}}}$	$36.95 \frac{\text{kJ}}{\text{mol}}$	$1.37 \cdot 10^{-5} \frac{\text{L}}{\text{h g}_{\text{Pt}}}$

The determined value of the apparent activation energy for the rate determining step is consistent with values reported in the literature. An activation energy of  $39\text{ kJ mol}^{-1}$  has been reported by Likozar and Grilc for the rate determining step of LA HDO over  $\text{NiMoS}_x/\text{Al}_2\text{O}_3$ <sup>118</sup>. For the competitive primary conversion of LA *via* decarboxylation towards butanone, a value several times higher ( $134\text{ kJ mol}^{-1}$ ) has been determined by Likozar and Grilc<sup>118</sup>. The high activation energy causes the high acceleration of LA decarboxylation over temperature and the sharp drop in GVL selectivity in the high temperature regime above  $220\text{ }^{\circ}\text{C}$ , presented in Figure 5-21 (left), which is highly consistent to the trends reported Likozar and Grilc<sup>118</sup>.

Based on these parameters, LA conversion can be determined from the integrated mole balance, while the total Pt time yield can be considered the integral (“mean”) LA consumption rate:

$$PTY_{tot}(\tau) = \frac{1}{\tau_N} \int_0^{\tau} r_{LA}^c d\tau_N = \frac{X}{\tau_N} \quad (5.22)$$

Here, the *molar* definitions of  $PTY$  and  $r$  are used for LA consumption and GVL formation, instead of *weight*-specific definitions, in order to be able to plot them in the same graph without “stretching” distortion due to the different molar masses of LA and GVL. As can be seen from Figure 5-24, the fitted kinetic model well describes the observed trend of LA consumption and GVL production.

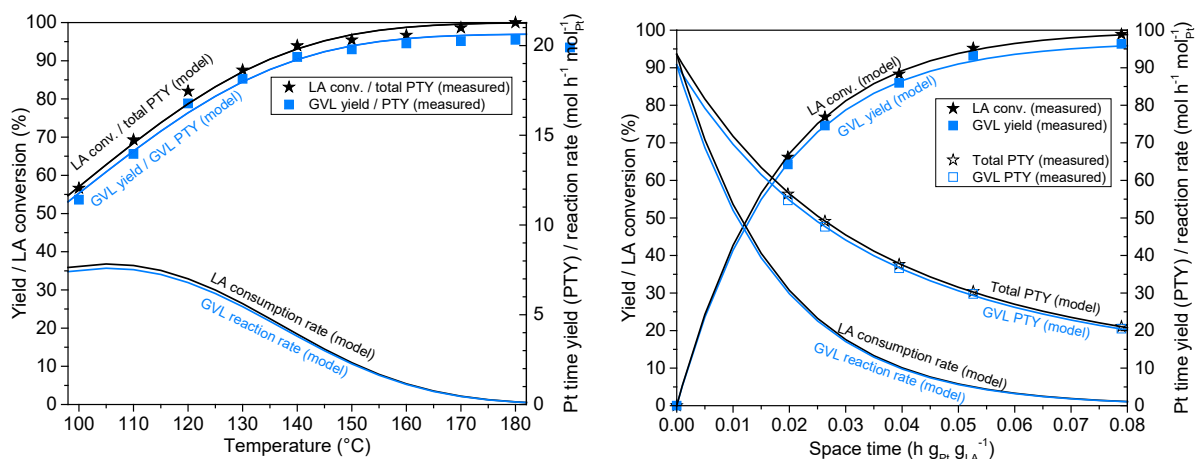


**Figure 5-24:** Measurements and fitted kinetic model for conversion, GVL yield, and Pt time yield in the LA hydrogenation over 2.7wt% Pt/C ( $2.4 \times 3.5$ mm). Effect of temperature (**left**) and space time (**right**). Conditions: 0.1M LA in H<sub>2</sub>O, 50 bar H<sub>2</sub>, H<sub>2</sub>:LA 5:1, space time of 0.079 h g<sub>Pt</sub> g<sub>LA</sub><sup>-1</sup> (**left**), 160 °C (**right**)

### 5.3.2 Formic Acid as Hydrogen Source

As an alternative to molecular external hydrogen, formic acid (FA) is used in the following as the reducing agent under conditions equivalent to those in the previous subchapter, using the same type of catalyst (2.7wt% Pt/C). As can be seen in Figure 5-25 (right), excellent GVL selectivity of >96% is obtained in the temperature range from 180 to 240 °C, with a maximum of 99.0% (48.6% LA conversion) at 210 °C and a similar value of 98.7% (65.3% LA conversion) at 220 °C. This even outperforms the H<sub>2</sub>-assisted LA hydrogenation process (97.9% GVL selectivity, as reported in section 5.3.1).

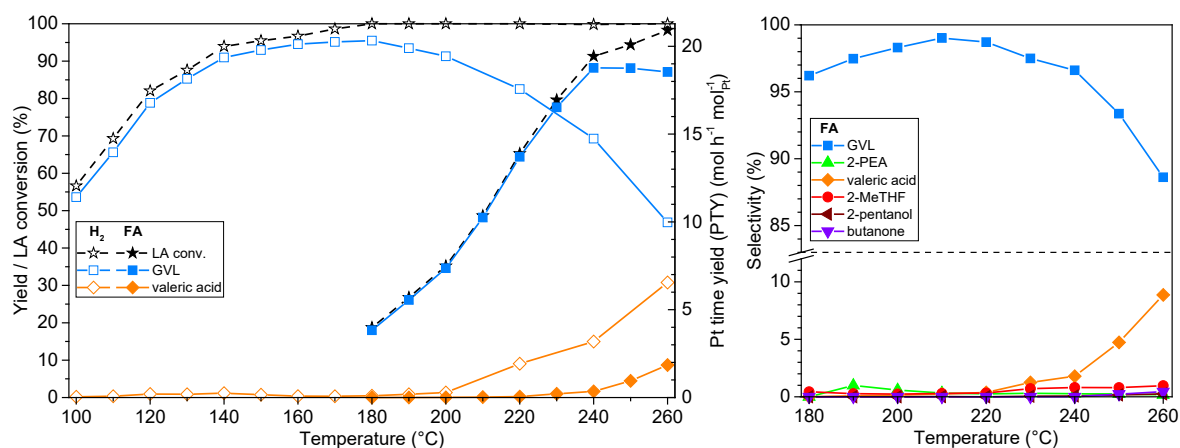


**Figure 5-25:** Effect of temperature on conversion, yield, and Pt time yield of main products (**left**) as well as selectivity (**right**) in LA hydrogenation over 2.7wt% Pt/C ( $2.4 \times 3.5$ mm). Conditions: 50 bar, 0.1M LA and 0.5M FA in H<sub>2</sub>O reactant solution (FA:LA 5:1), space time of 0.079 h g<sub>Pt</sub> g<sub>LA</sub><sup>-1</sup>; **left**: compared with H<sub>2</sub>-assisted hydrogenation conducted under the same conditions (50 bar H<sub>2</sub>; H<sub>2</sub>:LA 5:1)

Despite the outstanding selectivity, the overall activity is decreased, as compared to the H<sub>2</sub> system. To reach similar levels of activity at equal space time, temperature increase of *ca.* +110

°C would be necessary. In the very high temperature regime above 240 °C, consecutive reduction steps – predominantly towards valeric acid – diminish the GVL yield.

Therefore, the GVL yield can be enhanced by increasing the space time at lower temperature of 220 °C, where GVL is still highly resistant to consecutive hydrogenation. As can be seen from Figure 5-26, even very long contact times with the catalyst hardly increase the formation of byproducts at 220 °C. Maximum GVL yield of 92.6% (97.7% LA conversion) was provided at a high space time of 0.158 h g<sub>Pt</sub> g<sub>LA</sub><sup>-1</sup>. This is identified as the optimum condition for this catalytic system, albeit the maximum Pt time yield of 16.9 mol<sub>GVL</sub> h<sup>-1</sup> mol<sub>Pt</sub><sup>-1</sup> ( $\triangleq$  8.7 g<sub>GVL</sub> h<sup>-1</sup> g<sub>Pt</sub><sup>-1</sup>) is obtained in the low conversion regime, as shown in Figure 5-26 (left).

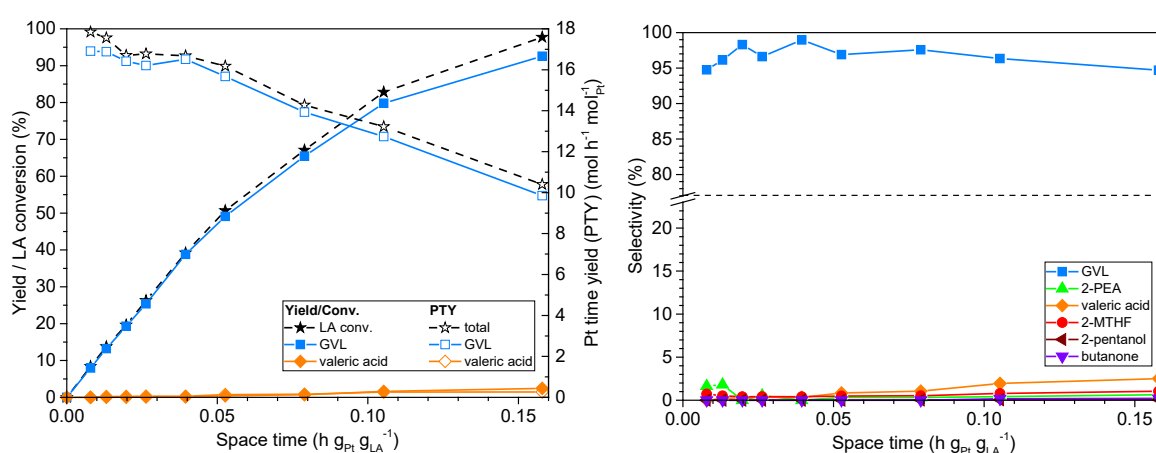


**Figure 5-26:** Effect of space time on conversion, yield, and Pt time yield of main products (**left**) and selectivity (**right**) in LA hydrogenation over 2.7wt% Pt/C (2.4 × 3.5mm). Conditions: 220 °C, 50 bar, 0.1M LA and 0.5M FA in H<sub>2</sub>O reactant solution (FA:LA 5:1)

Despite the lower GVL selectivity, the activity of the rate limiting step is strongly enhanced when increasing the temperature by 40 K to 260 °C. However, low space times provide high Pt time yield of up to 54.2 mol<sub>GVL</sub> h<sup>-1</sup> mol<sub>Pt</sub><sup>-1</sup> ( $\triangleq$  27.8 g<sub>GVL</sub> h<sup>-1</sup> g<sub>Pt</sub><sup>-1</sup>) with excellent selectivity of 97.8% due to the short exposure of the as-formed GVL to the catalyst, as can be seen in Figure 5-27. Increase of space time towards higher LA conversion strengthens the gradually increasing formation of valeric acid at 260 °C, which diminishes the GVL yield to a maximum of 85.9% (92.1% LA conversion), obtained for a space time of 0.039 h g<sub>Pt</sub> g<sub>LA</sub><sup>-1</sup>.



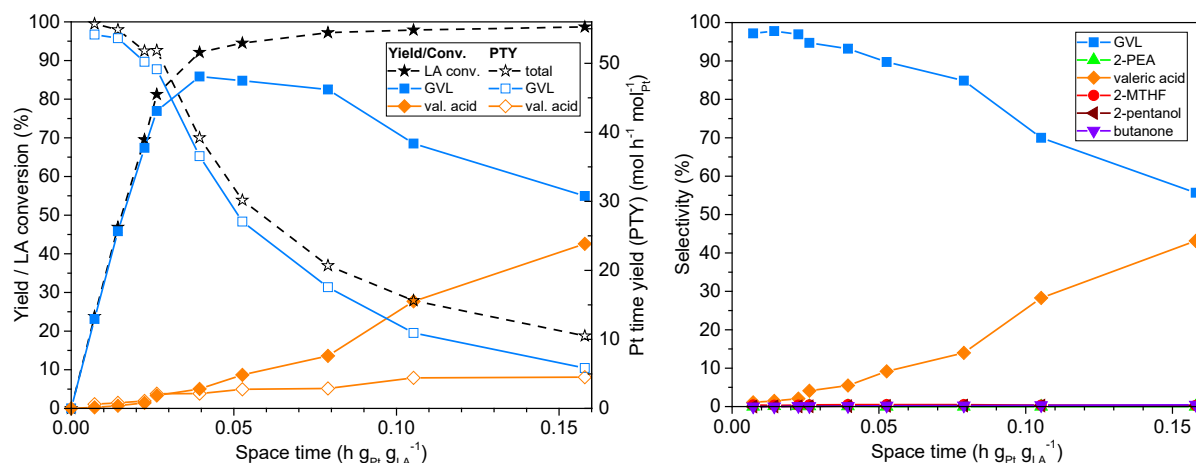


**Figure 5-27:** Effect of space time on conversion, yield, and Pt time yield of main products (**left**) and selectivity (**right**) in LA hydrogenation over 2.7wt% Pt/C ( $2.4 \times 3.5$ mm). Conditions: 260 °C, 50 bar, 0.1M LA and 0.5M FA in H<sub>2</sub>O reactant solution (FA:LA 5:1)

Despite the efforts to maximize the selectivity towards GVL by inhibiting consecutive reactions, valeric acid could be a valuable product, with possible application of its methyl and ethyl esters as flavors in the food industry or as high quality biofuels<sup>119</sup>. As shown in Figure 5-27 (left and right), high yield (42.6%) and selectivity (43.2%) of valeric acid is obtained even at the highest space time of 0.158 h g<sub>Pt</sub> g<sub>LA</sub><sup>-1</sup>, with side products amounting to only 1.0%. Further increase of temperature or space time is expected to further enhance the obtained yield of valeric acid, which would be interesting for future investigation targeted at the selective hydrogenation of LA towards valeric acid.

Increase in valeric acid yield has also been observed at operation pressures below the vapor pressure of the solvent. As can be seen in Figure 5-28 (left), lowering the pressure from 30 to 10 bar increases the valeric acid yield from 0.4% to 13.2% for the 2.7wt% Pt/C, which therefore results in diminished GVL yield.

Partly, this trend can be attributed to the fact that, due to vaporization of H<sub>2</sub>O in the preheating unit and the reactor, the high boiling point components reside in the system for a longer time in a concentrated liquid phase. This hypothesis is supported by the fact that LA conversion is slightly increased as well. However, extended residence time alone would not explain the promotion of the consecutive hydrogenation to such an extent, since increase of space time towards almost full LA conversion hardly promotes the formation of valeric acid at 220 °C, as has been shown earlier in Figure 5-26.

Therefore, it is hypothesized that the accumulation of GVL could exceed the saturation in the liquid phase, which consists of primarily H<sub>2</sub>O and LA. This phenomenon might cause dissolution

of GVL into a second, less volatile liquid phase that resides on the catalyst surface, intensifying the contact of GVL with the active sites, while displacing the LA-rich aqueous phase from the catalyst surface. However, to prove this hypothesis by evidence, further investigation is necessary.

At the same temperature of 220 °C, the catalyst with a lower Pt loading of 0.8wt% exhibits higher selectivity towards valeric acid than the 2.7wt% catalyst. It is assumed that the observed difference in terms of selectivity towards valeric acid is mainly due to temperature fluctuations inside the reactor. As can be seen on the right side of Figure 5-28, the formation of valeric acid over 0.8wt% Pt/C is highly sensitive to temperature in the range of 210 and 220 °C. Due to the lower loading with active metal, lower reactant flow rates are used in order to facilitate space times comparable to those over the catalyst with the higher loading of 2.7wt%. This could possibly cause local temperature gradients of a few K inside the reactor, allowing for the formation of valeric acid in thermal “hot spots” of the catalytic bed, which could lead to a higher yield, compared with true isothermal conditions. Operation at around or above the boiling point of the solvent could amplify such gradients as the axial thermal conductivity inside the reactor bed is diminished.

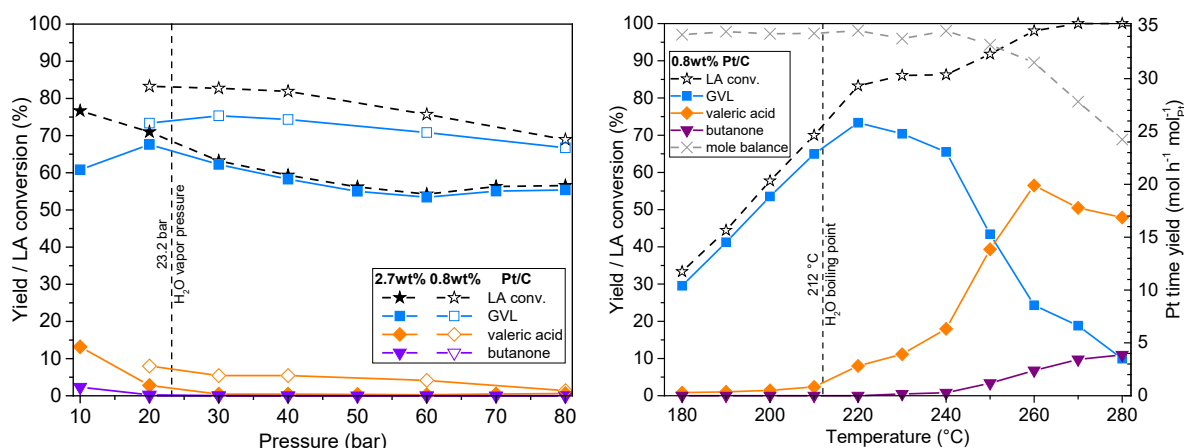


**Figure 5-28:** Effect of pressure (**left**) and temperature (**right**) on conversion, yield, and Pt time yield of main products in LA hydrogenation over 0.8wt% Pt/C (space time of 0.048 h g<sub>Pt</sub> g<sub>LA</sub><sup>-1</sup>). **left:** compared with 2.7wt% Pt/C (space time of 0.079 h g<sub>Pt</sub> g<sub>LA</sub><sup>-1</sup>). Conditions: 0.1M LA and 0.5M FA in H<sub>2</sub>O reactant solution (FA:LA 5:1), 220 °C (**left**), 20 bar (**right**)

Due to the higher tendency to form valeric acid, lower maximum yields of GVL are achieved with the 0.8wt% Pt pellets (75.3% at 30 bar, 220 °C), as compared to the previously reported 92.6% for the 2.7wt% Pt catalyst. However, the overall activity with respect to the weight of active metal is strongly increased, as can be seen by the higher slope of LA conversion vs. space time (with respect to the Pt weight) on the left side of Figure 5-29. This effect is likely to be caused by the higher dispersion of Pt on the support for lower loadings and – therefore higher surface area of the active metal, relative to its weight. Thus for the GVL production, increased time yield (with

respect to the total Pt weight) is obtained, reaching up to  $51.6 \text{ mol}_{\text{GVL}} \text{ mol}_{\text{Pt}}^{-1} \text{ h}^{-1}$  ( $26.5 \text{ g}_{\text{GVL}} \text{ g}_{\text{Pt}}^{-1} \text{ h}^{-1}$ ) at  $220^\circ\text{C}$  and 20 bar with GVL selectivity of up to 97.9% in the low conversion regime, as compared to the previously reported  $16.9 \text{ mol}_{\text{GVL}} \text{ h}^{-1} \text{ mol}_{\text{Pt}}^{-1}$  for 2.7wt% Pt/C at  $220^\circ\text{C}$  and 50 bar.

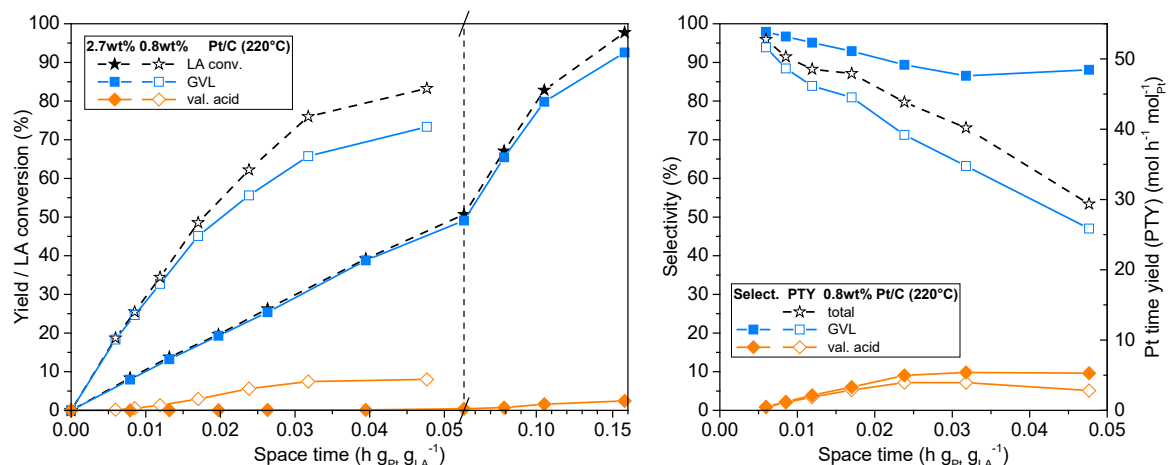


**Figure 5-29:** Effect of space time on conversion and yield (left) as well as selectivity and Pt time yield (right) of main products in LA hydrogenation over 0.8wt% Pt/C. **left:** compared with 2.7wt% Pt/C. Conditions: 0.1M LA and 0.5M FA in H<sub>2</sub>O reactant solution (FA:LA 5:1),  $220^\circ\text{C}$ , 20 bar

Similar influence of Pt particle size on the catalytic performance is observed for the Pt/C variant with only 0.5wt% Pt. Comparison with the 2.7wt% catalyst at  $260^\circ\text{C}$  and 50 bar over space time (with respect to the total weight of Pt) shows improved activity due to the higher Pt dispersion, reaching an Pt time yield of up to  $113.7 \text{ mol}_{\text{GVL}} \text{ mol}_{\text{Pt}}^{-1} \text{ h}^{-1}$  ( $\triangleq 58.3 \text{ g}_{\text{GVL}} \text{ g}_{\text{Pt}}^{-1} \text{ h}^{-1}$ ), as shown in Figure 5-30 (right). Furthermore, the formation of valeric acid is highly favored over the 0.5wt% catalyst.

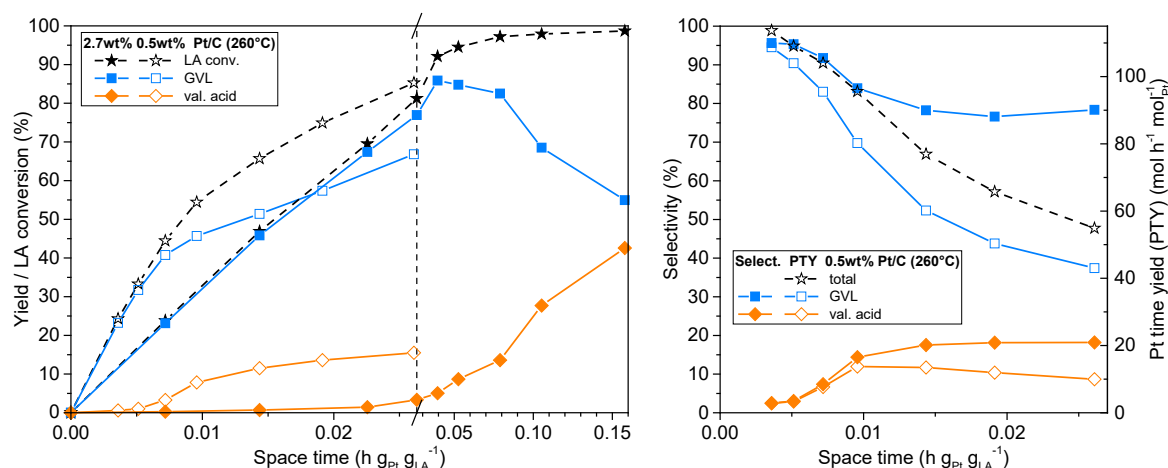


**Figure 5-30:** Effect of space time on conversion and yield (left) as well as selectivity and Pt time yield (right) of main products in LA hydrogenation over 0.5wt% Pt/C. **left:** compared with 2.7wt% Pt/C. Conditions: 0.1M LA and 0.5M FA in H<sub>2</sub>O reactant solution (FA:LA 5:1),  $260^\circ\text{C}$ , 50 bar

The prepared and tested Pt/C materials prove to be highly stable in the FA-assisted LA hydrogenation, despite the harsh reaction conditions of temperatures up to 260 °C in acidic medium. As can be seen in Figure 5-31, the 2.7wt% Pt/C provides decent stability over 23 h of time on stream, with stable high LA conversion at 260 °C, dropping from 97.2% at 3 h TOS to 96.6% at 22 h TOS.

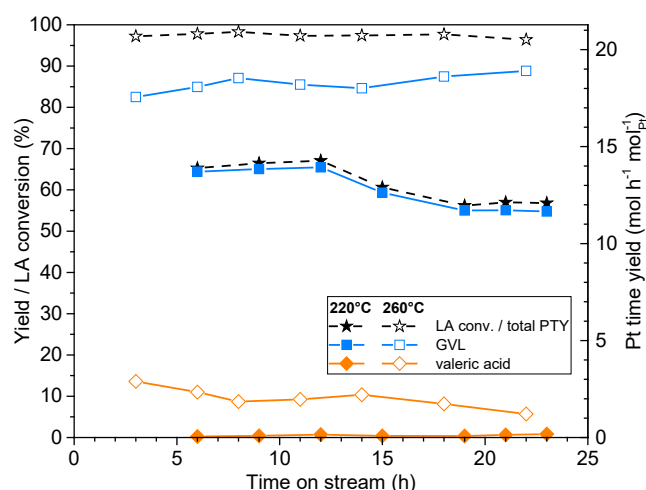


**Figure 5-31:** Time on stream evolution for conversion, yield, and Pt time yield for main products in LA hydrogenation over 2.7wt% Pt/C ( $2.4 \times 3.5$ mm). Conditions, 0.1M LA and 0.5M FA in H<sub>2</sub>O reactant solution (FA:LA 5:1), space time of 0.079 h g<sub>Pt</sub> g<sub>LA</sub><sup>-1</sup>, 50 bar

The consecutive hydrogenation towards valeric acid at 260 °C, as well as the LA conversion at 220 °C, exhibit a distinct drop in activity in a window between *ca.* 14 h and 19 h time on stream, whereas before and after this period of increased deactivation the catalyst provides higher stability. As during the intermediate phase of deactivation, the pressure was varied between 10 and 80 bar, it is concluded that extremely high and low pressures are detrimental to the stability and should be avoided for the sake of a longer lifetime of the Pt/C catalysts.

In addition to the prepared Pt/C catalysts, several pelletized Ni/C variants are tested in the FA-assisted hydrogenation of LA in aqueous reactant solution. In Figure 5-32, LA conversion and GVL yield are plotted against space time (with respect to the total weight of Ni) for the three different metal loadings 5, 21, and 29wt%.

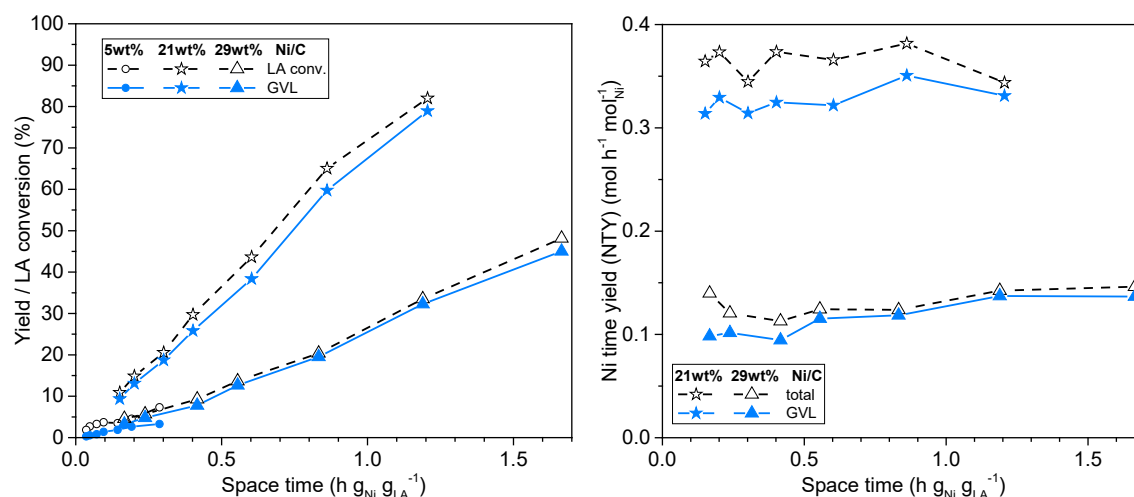


**Figure 5-32:** Effect of space time on conversion and yield (left) as well as Ni time yield (right) of main products in LA hydrogenation over 5wt%, 21wt%, and 29wt% Ni/C. Conditions: 0.1M LA and 0.5M FA in H<sub>2</sub>O reactant solution (FA:LA 5:1), 220 °C, 20 bar

Interestingly, of the three materials, the 21wt% Ni/C provides the highest level of activity with respect to the Ni weight. At 220 °C, a maximum Ni time yield of  $0.35 \text{ mol}_{\text{GVL}} \text{ mol}_{\text{Ni}}^{-1} \text{ h}^{-1}$  ( $\pm 0.21 \text{ g}_{\text{GVL}} \text{ g}_{\text{Ni}}^{-1} \text{ h}^{-1}$ ) was obtained for the 21wt% Ni/C, whereas the 29wt% Ni/C only provides a level of up to  $0.13 \text{ mol}_{\text{GVL}} \text{ mol}_{\text{Ni}}^{-1} \text{ h}^{-1}$  ( $\pm 0.08 \text{ g}_{\text{GVL}} \text{ g}_{\text{Ni}}^{-1} \text{ h}^{-1}$ ). This can be attributed to the higher dispersion of the metal, compared with the 29wt% catalyst. Furthermore, in view of the decreased pore volume of the 29wt% catalyst of  $0.55 \text{ cm}^3/\text{g}$ , compared to  $0.74 \text{ cm}^3/\text{g}$  for the support, as presented in section 3.2, it is hypothesized that the high amount of Ni blocks the entrances of pores, thus making sections of the porous network inaccessible for the reactant or limiting the diffusion through the pores to a considerable extent. The 5wt% catalyst, however, which is assumed to exhibit the highest Ni dispersion, provides activity on such a low level that it becomes unfeasible for the catalytic application because the retention time of the liquid inside the catalytic bed (and the preheating system) needs to be increased to more than 1 h. Due to the long exposure to high temperature, competing thermal decomposition of the reactant diminishes the GVL selectivity to only *ca.* 50%.

At 260 °C, no significant change of activity is observed apart from the additional formation of a low amount of valeric acid, compared with 220 °C, as can be seen in Figure 5-33. However, especially at high temperature, exposure of the Ni/C catalysts to acidic aqueous solution causes fast deactivation.

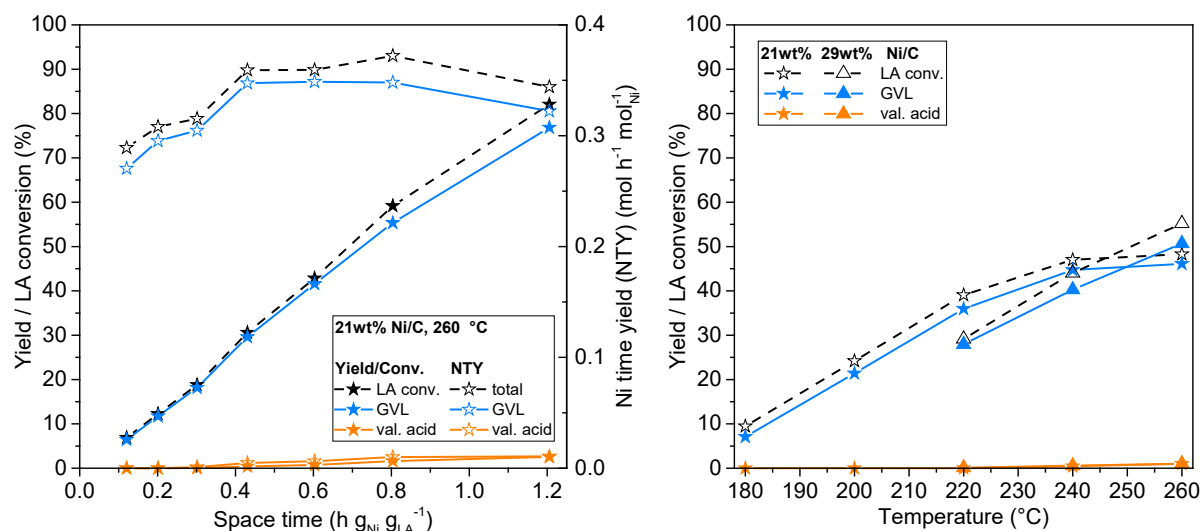


**Figure 5-33:** Effect of space time (**left**) and temperature (**right**) on conversion and yield of main products in LA hydrogenation over 21wt% Ni/C. **right:** compared with 29wt% Ni/C. Conditions: 0.1M LA and 0.5M FA in H<sub>2</sub>O reactant solution (FA:LA 5:1), 260 °C, 50 (**left**) and 40 (**right**) bar; **right:** space time of 1.21 (1.67) h g<sub>Ni</sub> g<sub>LA</sub><sup>-1</sup> for 21wt% (29wt%) Ni/C

This deactivation process is even strongly accelerated at constant operation temperature of 260 °C, as can be seen from Figure 5-34 (right), compared with 220 °C (Figure 5-34 left and middle). Although in this work, promising catalytic behavior in the LA hydrogenation reaction has been observed for the 21wt% Ni/C catalyst, its use in a continuous flow system with aqueous reactant solution is not recommended due to the fast deactivation process even at the milder condition of 220 °C. However, as the 21wt% Ni/C showed decent reactivity and stability in the HMF hydrogenation, using ethanol as the solvent, its performance in the LA hydrogenation reaction will be studied in further investigations, using ethanol and other non-hazardous bioderived solvents instead of water.

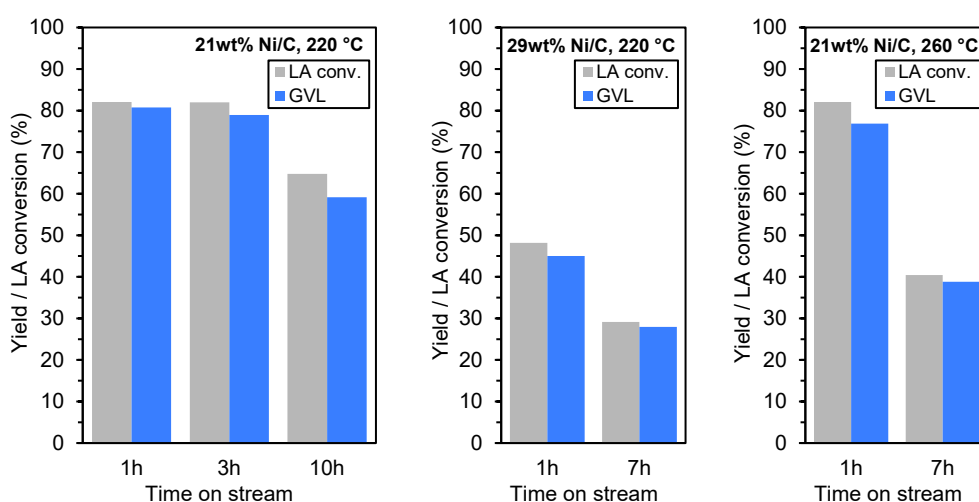


**Figure 5-34:** Time on stream evolution of conversion and GVL yield in LA hydrogenation over 21wt% and 29wt% Ni/C at 220 and 260 °C. Conditions: 0.1M LA and 0.5M FA in H<sub>2</sub>O reactant solution (FA:LA 5:1), space time of 1.21 (**left**, **right**) and 1.67 (**middle**) h g<sub>Ni</sub> g<sub>LA</sub><sup>-1</sup>, 40 bar (**left**, **middle**) and 50 bar (**right**)

As can be seen in Figure 5-35 from the TEM images and particle size distribution of the used 21wt% Ni/C, the catalyst pellets exhibit no considerable change of Ni nanoparticles size over 15 h time on stream of LA hydrogenation in water.

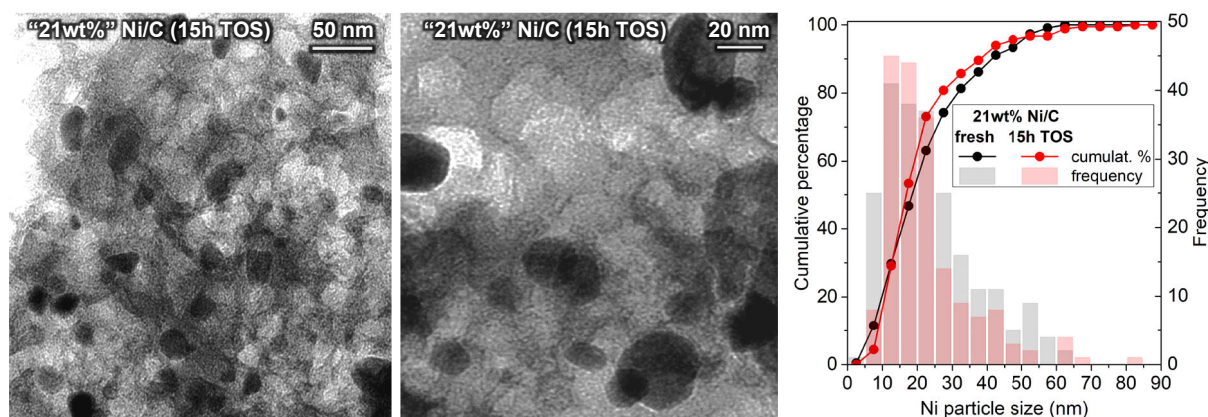


**Figure 5-35:** TEM images (**left, middle**) and Ni particle size distribution (**right**) of the (originally) 21wt% Ni/C pellets after 15 h time on stream of LA hydrogenation in water; **right**: compared with fresh catalyst before reaction

Ostwald ripening is not observed, as can be inferred from the constant mean particle size (26 – 27 nm) and nearly constant crystallite size (28 – 29 nm), measured by TEM and XRD (Figure 5-36), respectively, and summarized in Table 5-6. Therefore, the main deactivation processes are expected to be the leaching and fouling of the nanoparticles. Indeed, the Ni loading decreased considerably from the original 21wt% to 16wt%, as measured by ICP.

**Table 5-6:** Analysis of Ni nanoparticle and crystallite size of the 21wt% Ni/C catalyst before and after 15 h time on stream of LA hydrogenation in water; *a*: determined from particle size distribution on TEM images; *b*: determined as average value of three mean crystallite sizes calculated from the three main peaks in the XRD diffractogram; *c*: measured by inductively coupled plasma (ICP)

Sample	Mean particle size <sup>a</sup> [nm]		Crystallite size <sup>b</sup> [nm]	Ni loading <sup>c</sup> [wt%]
	Surface-weighted	Sauter		
21wt% Ni/C				
fresh	27	38	29 (Ni <sup>0</sup> )	21.3 ±1
15 h TOS	26	39	28 (Ni <sup>0</sup> )	16.4 ±1

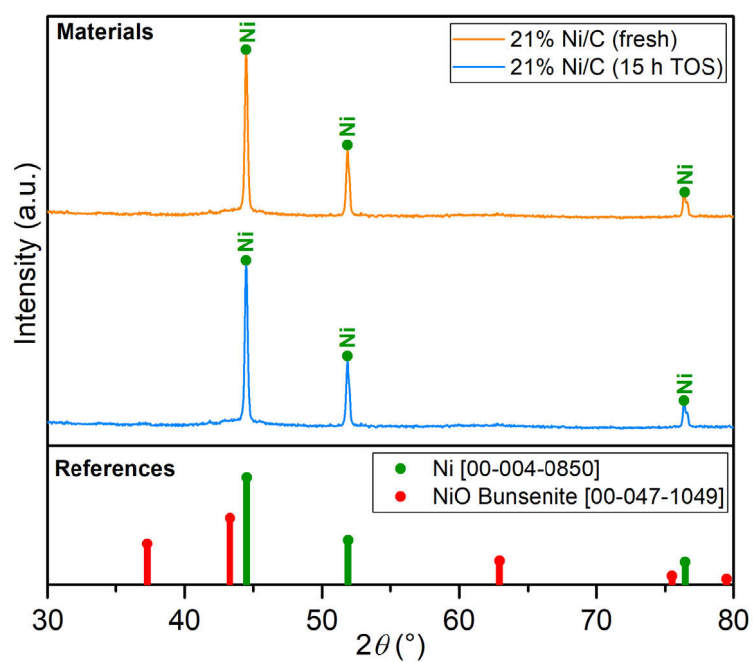


**Figure 5-36:** XRD diffractograms of the 21wt% Ni/C catalyst before and after 15 h time on stream of LA hydrogenation in water



# 6

## CONCLUSION AND OUTLOOK

Upgrading of bioderived carbohydrates towards valuable chemicals, fuels, and polymers is one of the most promising fields of biorefinery. It will play an essential part in the shift from the conventional industry, which is entirely dependent on the use of fossil resources, towards a more sustainable industry that utilizes abundant renewable resources and provides products with a closed carbon cycle and – ideally – carbon neutrality.

Despite the bright opportunities, the implementation of efficient valorization schemes remains a big challenge. Only extensive research will facilitate high product yields at low economic and environmental costs. One of the most important aspects is to develop suitable catalytic processes and multiprocess systems that allow for continuous large-scale production of biobased products. This includes the development of suitable catalysts and suitable reaction systems, as well as the effectiveness of the combination of these two aspects, since the performance of a catalyst also depends on the process environment.

The present research ties in with this concept by developing a novel synthesis procedure of pelletized, highly active hydrogenation catalysts, aimed at the utilization at industrial scale. The methodology was developed in an iterative procedure of material synthesis and simultaneous performance tests in the two applications for the production of valuable platform molecules: The hydrodeoxygenation of 5-hydroxymethylfurfural (HMF) to 2,5-dimethylfuran (DMF) and the hydrogenation of levulinic acid (LA) to  $\gamma$ -valerolactone (GVL).

Owing to this direct performance feedback, the synthesis of the extruded porous carbon support pellets was enhanced in many cycles for the use in continuous flow reactors. The final synthesis procedure is simple and capable of scaled-up catalyst production with only basic and cheap technical equipment, using durum semolina as the carbon source and ZnO nanopowder as the porogenic templating agent. The prepared carbon support extrudates exhibit a hierarchical pore structure with very high surface area of  $756 \text{ m}^2 \text{ g}^{-1}$  and very large mesopore volume of  $0.49 \text{ cm}^3 \text{ g}^{-1}$  (QSDFT  $\text{N}_2$  adsorption). This is a major advancement for the research on carbon-supported catalysts, as usually carbon supports with such a high porosity are developed as powders instead of firm pellets. Employing these high-performance materials in packed-bed reactors for continuous-flow operation opens a new window of engineering possibilities, such as process integration of several valorization steps.

To facilitate precise catalytic performance tests for the synthesized catalysts under varied conditions and different reactor dimensions, a tunable continuous-flow set-up has been built, which can accommodate flow reactors in the milliliter to liter scale and can be operated safely at up to 290 bar or up to 450 °C. Owing to several individually controlled heating sections, isothermal conditions inside the reactor can be ensured.

For the HMF hydrodeoxygenation in EtOH, the synthesized 21wt% Ni/C catalyst provided a DMF yield of up to 80.5% (99.0% HMF conversion) at 150 °C, 20 bar of  $\text{H}_2$ ,  $\text{H}_2$ :HMF ratio of 7.5:1 and space time of  $2.66 \text{ h g}_{\text{Ni}} \text{ g}_{\text{HMF}}^{-1}$ . The catalyst exhibited high stability during the total operation period, with a slight drop of DMF yield from 67.3% at 2 h to 63.7% at 33 h time on stream (space time of  $1.33 \text{ h g}_{\text{Ni}} \text{ g}_{\text{HMF}}^{-1}$ ).

Using a 2.7wt% Pt/C catalyst for the LA hydrogenation in water, extraordinary GVL selectivity of up to 97.9% (95.2% LA conversion) was obtained (160 °C, 50 bar of  $\text{H}_2$ ,  $\text{H}_2$ :LA ratio of 5:1, space time of  $0.053 \text{ h g}_{\text{Pt}} \text{ g}_{\text{LA}}^{-1}$ ). By extending the space time to  $0.079 \text{ h g}_{\text{Pt}} \text{ g}_{\text{LA}}^{-1}$ , the GVL yield was enhanced to 96.4% (98.9% LA conversion) with a Pt time yield of  $20.5 \text{ mol}_{\text{GVL}} \text{ h}^{-1} \text{ mol}_{\text{Pt}}^{-1}$ . At lower space time of  $0.020 \text{ h g}_{\text{Pt}} \text{ g}_{\text{LA}}^{-1}$ , Pt time yield of  $54.7 \text{ mol}_{\text{GVL}} \text{ h}^{-1} \text{ mol}_{\text{Pt}}^{-1}$  (66.2% LA conversion) was obtained.

In order to establish a process that is based on 100% bioderived feedstock, formic acid (FA) has been employed as an alternative, renewable hydrogen source instead of molecular hydrogen. Using the same type of 2.7wt% Pt/C catalyst as for the  $\text{H}_2$ -assisted process, a GVL yield of 92.6% (97.7% LA conversion) was achieved at a high space time of  $0.158 \text{ h g}_{\text{Pt}} \text{ g}_{\text{LA}}^{-1}$  (220 °C, 50 bar, FA:LA ratio of 5:1). Although FA naturally exhibits lower reactivity than molecular  $\text{H}_2$ , similar

trends of activity and selectivity were observed at temperatures 110 K higher than the reference points of the H<sub>2</sub>-assisted process. In terms of GVL selectivity, the FA-assisted process even outperformed the H<sub>2</sub>-assisted process with up to 99.0% (51.4% LA conversion) at 210 °C, 50 bar, FA:LA ratio of 5:1, and space time of 0.079 h g<sub>Pt</sub> g<sub>LA</sub><sup>-1</sup>.

To cover the entire valorization scheme from sugars towards the desired hydrogenation products DMF and GVL, preliminary results on the catalytic performance of glucose and fructose conversion towards HMF and LA have been conducted. For the base-catalyzed isomerization of 0.1M glucose in water, 49.0% fructose selectivity with traces of mannose (35.8% glucose conversion) was obtained over 10ZrO<sub>2</sub>-90Al<sub>2</sub>O<sub>3</sub> pellets at 125 °C. The acid-catalyzed dehydration of 0.1M fructose in water at 150 °C provided HMF selectivity of 50.4% (42.3% fructose conversion). Including the valuable consecutive products LA (20.7%) and FA (13.4%), a total carbon-based product selectivity of 84.5% was reached at this point.

In addition to the remarkable GVL selectivity in the presented LA hydrogenation processes, the fact that LA itself is produced *via* hydrolysis of HMF towards LA and FA demonstrates the potential of a process that integrates the acid-catalyzed hydrolysis of HMF into the subsequent metal-catalyzed hydrogenation of LA and employs *in situ* produced FA as the hydrogen source. Since this process integration prevents the necessity for a separation step of the equimolar product mixture of the two acids and, in addition, is a self-sufficient process without external hydrogen feed, it is assumed to have a high impact on the cost-efficiency and sustainability of the overall process. Therefore, it is recommended to investigate such a bicatalytic process as a future work based on the results of this research.

In conclusion, the present work developed a methodology for the synthesis of hydrogenation catalysts in a mature stage, combined with a broad screening of their catalytic performance in the hydrogenation of HMF and LA within a wide condition matrix. The high activity and selectivity of the catalysts observed for the two hydrogenation processes show great promise for future application at industrial scale. Nevertheless, in order to establish a complete mapping of the catalytic behavior, it is recommended to complement the present results with further investigation, particularly on the catalyst stability, deactivation mechanisms, and recyclability. In addition, further investigation is recommended into strategies of heteroatom-doping, such as nitrogen-doping, and their effect on the interactions of the support with the metal.

For many other biorefining schemes, hydrodeoxygenation steps also play a crucial role to reduce the high oxygen content of lignocellulosic and other types of biomass. For this reason, the

utilization of the synthesized catalysts will be expanded in future work to other hydrogenation applications. In particular, the catalysts have been tested in lignin depolymerization applications, which will be intensified in further investigation. To fit larger molecules such as lignin, the methodology can be easily tuned towards larger pores, just by varying the size distribution of the ZnO particles that are used as the templating agent. Furthermore, the prepared Ni/C catalysts have been tested in the hydrogenation of glucose towards sorbitol, which is, along with LA, ranked one of the *twelve top value-added biobased chemicals* that – according to the U.S. Department of Energy – constitute the most important building blocks for an extensive biorefining industry<sup>5</sup>.



## MATERIALS AND METHODS

### A.1 Chemicals and Materials

The following chemicals and materials were acquired from Sigma-Aldrich/Merck: Zinc chloride (ACS, 98%), tetraamineplatinum(II) nitrate (99.995% trace metal basis), hexaamineruthenium(III) chloride (98%), urea (99%), D-glucose (99%), D-fructose (99%), D-mannose (99%), D-galactonose (99%), glycolic acid (99%), levoglucosan (99%), D-sorbitol (98%),  $\delta$ -gluconolactone (99%), levulinic acid (98%), formic acid (98%), microcrystalline cellulose (20  $\mu$ m, 99%),  $\gamma$ -valerolactone (98%, FCC, FG)  $\alpha$ -angelica lactone (98%), 2,5-hexanedione (98%), 3-pentenoic acid (95%; 90% in *trans*-form), *trans*-2-pentenoic acid (98%), 5-methylfurfuryl alcohol (98%), 5-ethoxymethylfurfural (97%), 2,5-dimethyltetrahydrofuran (mixture of *cis* and *trans*, 96%), 2,5-dimethylfuran (99%), ethyl levulinate (99%), acetaldehyde diethyl acetal (99%), DL-glyceraldehyde (90%), ethyl valerate (99%), Amberlyst-15 (hydrogen form, dry), sea sand (extra pure).

Zinc oxide powder (99.5%) with 20 nm average particle size was purchased from Nanostructured & Amorphous Materials, Inc. (USA). Ethanol (absolute, ACS, AnalaR NORMAPUR), hydrochloric acid (1M in water) and sodium hydroxide (1M in water) was provided by VWR BDH Chemicals. 5-Hydroxymethylfurfural was provided by AVA Biochem BSL AG (Switzerland; 99%) and Toronto Research Chemicals (Canada; 99%). Valeric acid (99%) and lactic acid (ACS, 85.0-90.0% aq. soln.) was purchased from Alfa-Aesar. Nickel(II) nitrate hexahydrate (99%), urea (99.5%) and acetic acid (ROTIPURAN 100%) was provided by

Roth. Butanone (99.7%, for HPLC) and another bottle of 2,5-dimethylfuran (99%) was bought from Acros Organics. The silica-alumina extrudates SIRALOX 20 HPV (20% Al<sub>2</sub>O<sub>3</sub>, 80% SiO<sub>2</sub>, 1.7 mm diameter) and the alumina-zirconia extrudates PURALOX Zr10 (90% Al<sub>2</sub>O<sub>3</sub>, 10% ZrO<sub>2</sub>, 1.6 mm diameter) were bought from Sasol. D-Cellobiose (95%) was acquired from Apollo Scientific. Polystyrene sulfonate (“PSS”, 1-5mm) was provided by AppliChrom. Ultrapure Milli-Q water was used as solvent. Red sea salt was acquired as an aquarium accessory from Amazon. Italian durum semolina (Divella semola di grano duro, rimacinata) was obtained from Il Tortellino d’Oro, an Italian restaurant in Berlin. Gluten has been purchased from L-carb-Shop (“Weizenkleber”, < 8% moisture, mesh +50).

## A.2 Applied Methods

### A.2.1 Product Analysis Methods

#### *A.2.1.1 Gas Chromatography (GC)*

The liquid product samples were examined, using an Agilent Technologies 5975 gas chromatograph, equipped with a flame ionization detector (FID) and connected to mass spectrometry (MS) detector (Agilent Technologies MSD 5975). The MS is connected to a USP phase G27 column (Agilent Technologies J&W HP-5MS ultra inert column with 30 m length, 0.250 mm diameter, 0.25µm film, consisting of (5%-phenyl)-methylpolysiloxane), while the FID is connected to a wax phase column (Restek Stabilwax-MS column with 30 m length, 0.250 mm diameter, 0.25µm film). For both operation modes, the following heating programs was applied: isothermal phase of 2 min at 50 °C, heating phase with 30 K/min heating rate to 250 °C, isothermal phase at 250 °C of variable duration (depending on the retention time of the of the substrates in the respective column). The injection volume was varied between 0.2 and 5 µL and the split ratio was set to values between 1:10 and 1:250. The product composition has been identified by MS and quantified by FID, using calibration curves obtained from prepared reference solutions. Even though at first, external and internal standards (such as dioctyl ether) were used for the quantification, they were not used in the final experiments, as the variance of concentrations determined without external standards was constantly below 1% of the total concentration and could not be enhanced by the use of standards.

#### *A.2.1.2 High Performance Liquid Chromatography (HPLC)*

Sugar-containing product samples were analyzed by an HPLC system (Agilent Technologies 1200 series) equipped with a Rezex ROA-Organic Acid H<sup>+</sup> column (8% crosslinked sulfonated styrene-

divinylbenzene, 300 mm length, 7.8 mm diameter) and connected to a refractive index detector (RID) and diode array detector (DAD). As the mobile phase, isocratic 0.1 vol.% formic acid in water was used with a flow of 0.35 to 0.5 mL/min, depending on the necessary separation performance of the substrates. The analysis was conducted at 75 °C, using injection volumes between 2 and 10 µL, depending on the necessary separation performance and resolution. For the DAD, both the UV lamp and visible light lamp are used and the spectrum is recorded in the range of 190 to 400 nm.

## A.2.2 Characterization Methods

### A.2.2.1 Nitrogen Physisorption

Nitrogen physisorption of the degassed (150 °C for 20 h) samples was conducted on a Quantachrome Autosorb-1 at 77 K. The recorded data was analyzed with the QuantaChrome QuadraWin software, using the following theories: BET (Brunauer–Emmett–Teller), BJH (Barrett–Joyner–Halenda), QSDFT (Quenched Solid Density Functional Theory), and NLDFT (Non-linear Density Functional Theory). For the QSDFT analysis of the carbon supports and carbon-supported catalysts analysis, a model with mixed slit, cylindrical, and spherical pores has been applied on the adsorption branch, using a moving point average of 5.

### A.2.2.2 X-Ray Powder Diffraction (XRD)

XRD measurements were conducted on a Bruker D8 diffractometer with the characteristic  $K_{\alpha}$  radiation of Cu (1.54 Å). The reference patterns are acquired from the ICDD PDF-4+ database (2017 and 2018 edition).

### A.2.2.3 Scanning Electron Microscopy (SEM)

After Au/Pd sputtering of the non-conductive samples, SEM images were taken using a LEO 1550-Gemini system with an electron acceleration voltage of 3.00 kV.

### A.2.2.4 Transmission Electron Microscopy (TEM)

TEM images were obtained using a Zeiss EM 912 Ω microscope with an acceleration voltage of 120 kV. The electron beam is produced from a tungsten filament. The particle size of the observed metal nanoparticles are measured manually, using Fiji ImageJ.

### A.2.2.5 Inductively Coupled Plasma Optical Emission Spectrometry (ICP-OES)

For the detection and quantification of metals and phosphorus content, ICP-OES is applied. For this, a ground specimen of *ca.* 10-20 mg is added to 500 µL of aqua regia (333 µL fuming HCl +

167  $\mu\text{L}$  fuming  $\text{HNO}_3$ ) and left overnight for digestion, followed by dilution of factor 8. The plasma is generated by argon heated by a Tesla coil to 7000 K.

#### A.2.2.6 Combustion Elemental Analysis (EA)

For the determination of C, H, and N content of the materials, combustion elemental analysis was performed on a Vario Micro setup.

#### A.2.2.7 Thermogravimetric Analysis (TGA)

TGA was carried out using a Netzsch TG209-F1 Libra with a heating rate of  $10\text{ K min}^{-1}$  in  $\text{N}_2$ .

#### A.2.2.8 Böhm Titration

The density of acid sites on the surface of the solid acid materials was determined by Böhm titration. For this, 50-200 mg (depending on the expected acidity) of material has been added to 10mL of 0.05M NaOH solution. After stirring overnight, the suspension was filtered through a  $0.2\text{ }\mu\text{m}$  PP syringe filter to retain the solid material. 8 mL of the clear solution with excess of basic sites has been used as the analyte. A 0.05M HCl titrant has been added stepwise to the solution, while monitoring the  $\text{pH}$  with a WTW SenTix 61 KCl electrode connected to a WTW MultiLab 540 device.

On the crosslinked polystyrene sulfonate acquired from AppliChrom, Böhm titration was performed after washing the material for 2 h in  $\text{H}_2\text{O}$  and drying at  $60\text{ }^\circ\text{C}$  overnight. The resulting curve is shown in the following Figure.

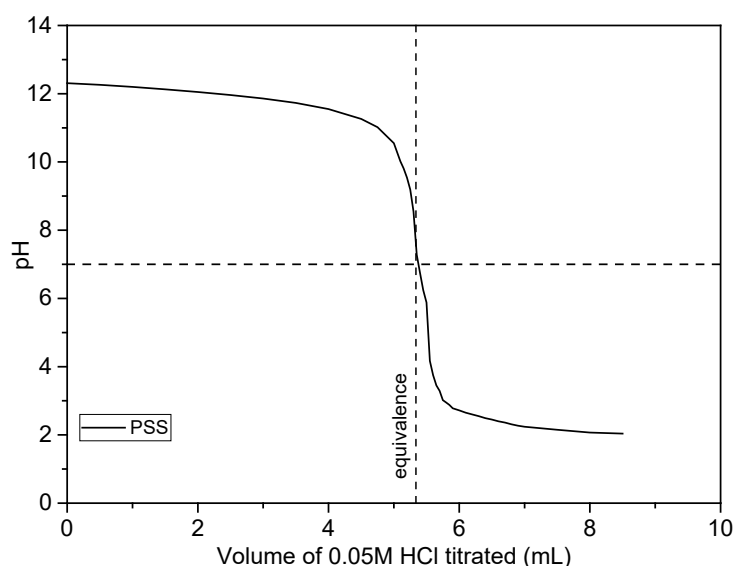


**Figure A-1:** Böhm titration of the polystyrene sulfonate (PSS). Analyte: 51.62 mg of material in 10mL 0.05M NaOH solution, stirred overnight, thereof 8 mL filtered through  $0.2\text{ }\mu\text{m}$  PP syringe filter. Equivalence point reached at 5.338 mL of 0.05M HCl titrated.



According to the following equation, the concentration of solid acid functionalities on the catalyst  $C_{SA}$  can be measured at this point, which is reached after adding  $V_{tit}^{eq} = 5.338$  mL of titrant to the solution.

$$C_{SA} = \frac{N_{SA}}{m_{cat} \frac{V_{ana}}{V_{NaOH}}} = \frac{[NaOH]_0 V_{ana} - [HCl] V_{tit}^{eq}}{m_{cat} \frac{V_{ana}}{V_{NaOH}}} = \frac{[NaOH]_0 - [HCl] \left( \frac{V_{tit}^{eq}}{V_{ana}} \right)}{\frac{m_{Ni/C}}{V_{NaOH}}} = 3.22 \frac{\text{eq}}{\text{kg}} \quad (6.1)$$

in which  $V_{ana} = 8$  mL is the analyte volume filtered from the prepared suspension with  $V_{NaOH} = 10$  mL of 0.05M NaOH and  $m_{cat} = 51.62$  mg of washed and dried PSS material.

Böhm titration was also carried out for the 21wt% Ni/C pellets used for the HMF hydrogenation in section 5.2. From the equivalence point of the titration curves presented in the following Figure, the density of solid acid sites is calculated, both for the fresh catalyst and the catalyst after 35 h of TOS in HMF hydrogenation. In Figure A-2, the Böhm titration curves are shown for both samples.

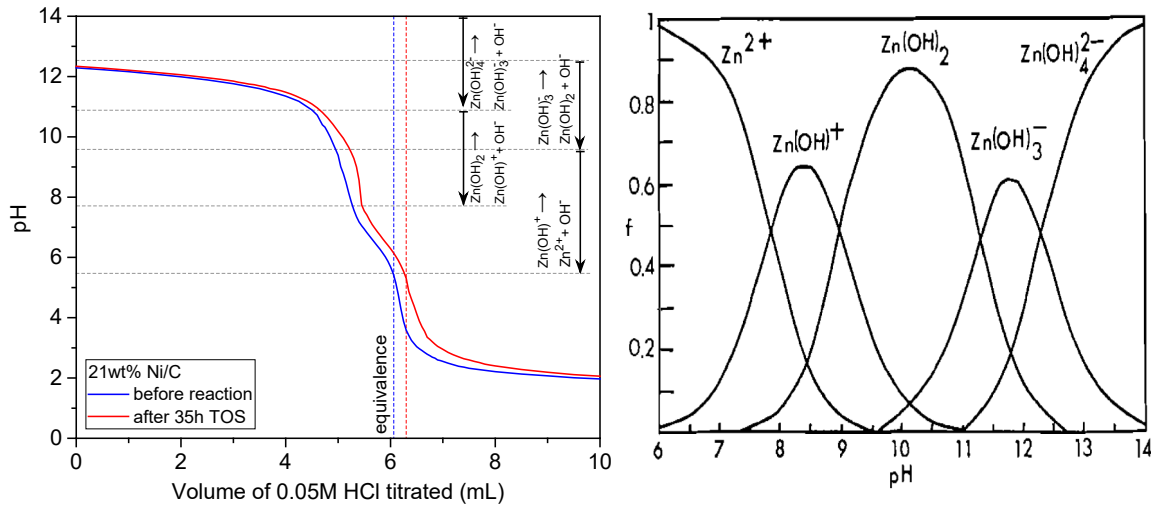
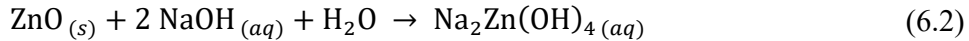


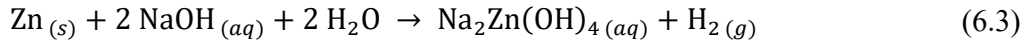
**Figure A-2:** left: Böhm titration of the 21wt% Ni/C catalyst. Analyte: 252.40 (251.75) mg of pellets before (after) 35 h TOS (HMF hydrogenation in EtOH). Preparation of analyte: 10mL 0.05M NaOH solution, stirred overnight, thereof 8 mL filtered through 0.2  $\mu\text{m}$  PP syringe filter; right: T and molar fractions of the associated species of  $\text{Zn}^{2+}$  and  $\text{OH}^-$  over pH in equilibrium at 25  $^\circ\text{C}$  (right), adapted from Reichle *et al.*<sup>97</sup>

The shoulder that both samples exhibit at a  $pH$  between *ca.* 5 to 6 in the titration diagram of Figure A-2 (left) suggests the presence of a dissolved weak acid that has passed through the filtration of the analyte before titration. The most probably cause of present acid is residues of Zn and ZnO in the material which have not been removed entirely during the catalyst preparation that involved the use of ZnO nanopowder as the porogen. Upon exposure to the strong dilute base

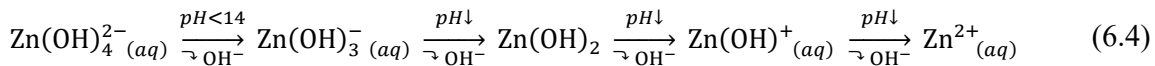
(0.05M NaOH), the ZnO residue in the material is expected to yield sodium zincate in NaOH solution:



Likewise, the elemental Zn that has been formed in the preceding heat treatment and reduction steps, readily reacts by displacing the hydrogen, which is lower than Zn in the activity series of metals. In this way, sodium zincate is formed:



Due to the amphoteric character of zinc hydroxide, titration of 0.05M HCl solution into the analyte leads to gradual release of  $\text{OH}^-$  from the associated complexes<sup>97</sup>:



At the equivalence point of *pH* 5.5, the zinc hydroxide species are completely dissociated. As presented in the Appendix A.2.2.8, a concentration of 0.48 eq  $\text{kg}^{-1}$  is calculated for the fresh catalyst, whereas after 35 h TOS the value decreases to a value of 0.43 eq  $\text{kg}^{-1}$ . This might include acidity from oxygen-containing groups on the surface of the porous carbon. However, at the *pH* of 12.29 (and 12.34), measured for the analytes produced from the 21wt% Ni/C before (and *after*) reaction, only 50% is present as the zincate species  $\text{Zn(OH)}_4^{2-}_{(aq)}$ , with 46% as  $\text{Zn(OH)}_3^{-}_{(aq)}$  and 4% as  $\text{Zn(OH)}_2$  at equilibrium<sup>97</sup>, as can be seen in Figure A-2 (right). The associated species of  $\text{Zn(OH)}_2$  is practically insoluble in water, as can be deduced from the low solubility of  $3.1 \cdot 10^{-6}$  mol  $\text{L}^{-1}$  at the half equivalence point (*pH* 10.14), at which  $\text{Zn(OH)}_2$  is present primarily in the associated form<sup>97</sup>.

With the equivalence point obtained for a titrant volume of  $V_{tit}^{eq} = 6.05$  (6.25) mL added to the solution for the 21wt% Ni/C catalyst before (after) 35 h TOS, the concentration of solid acid functionalities on the catalyst  $C_{SA}$  can be calculated by:

$$C_{SA} = \frac{N_{SA}}{m_{\text{Ni/C}} \frac{V_{ana}}{V_{\text{NaOH}}}} = \frac{[\text{NaOH}]_0 V_{ana} - [\text{HCl}] V_{tit}^{eq}}{m_{\text{Ni/C}} \frac{V_{ana}}{V_{\text{NaOH}}}} = \frac{[\text{NaOH}]_0 - [\text{HCl}] \left( \frac{V_{tit}^{eq}}{V_{ana}} \right)}{\frac{m_{\text{Ni/C}}}{V_{\text{NaOH}}}} \quad (6.5)$$

in which  $V_{ana} = 8$  mL is the analyte volume filtered from the prepared suspension with  $V_{\text{NaOH}} = 10$  mL of 0.05M NaOH and  $m_{\text{Ni/C}} = 252.40$  (251.75) mg of catalyst pellets before (after) the

catalytic experiment. For the fresh catalyst, a concentration of  $0.48 \text{ eq kg}^{-1}$  is calculated, whereas after 35 h TOS the value decreases to  $0.43 \text{ eq kg}^{-1}$ .



## ACKNOWLEDGMENT

I would like to express my sincere gratitude to Prof. Markus Antonietti for the great opportunity to be part of the MPIKG and carry out the research for my doctoral thesis under his supervision. His enthusiasm, his creative ideas, and his thinking outside the box gave valuable input to my work.

Furthermore, I would like to acknowledge Prof. Schomäcker for his interest in my topic and his kind support of my request to graduate at the Technical University of Berlin.

I would like to extend special thanks to Dr. Valerio Molinari, my mentor during the first period of my doctoral study, for the fruitful discussions and the valuable advice. Especially, I treasured Vale's clear-sightedness that continuously guided me in the right direction. Moreover, I am very grateful to Dr. Majd Al-Naji for his constant support throughout the second period of my work. Majd put much effort in mentoring me during this final phase of my doctoral research.

I would also like to acknowledge Max for his support as a peer doctoral student. He introduced me to various facilities and scientific fields and never got tired of answering the same questions over and over. In addition, José strongly contributed to the progress of my work with his broad knowledge about catalysis and chromatography, which I am very thankful for.

Furthermore, I would like to thank Irina for her technical and practical help in the laboratory. She constantly helped me with my work in and around the lab and provided countless time-consuming measurements for my research. Additional thanks go to Francesco for his great work as a Master's student in our group.

Moreover, I would like to thank the various colleagues for their valuable ideas. Although many more people have provided valuable input, I would like to give special thanks to Runyu, Ralf, Milena, Martin, Svitlana, and Nina.

Many thanks go to the many people who supported me with their technical skills. Namely, I want to thank Bodo, Regina, Jessica, Jeannette, Heike, Rona, Antje, Caro, Luisa, Eva, Sylvia, Daniel, Paul, Ralf, René, and Fridjof.

However, many more people have contributed with their knowledge and skills. By addressing the whole Colloid Chemistry department, I would like to extend my acknowledgment to everyone who was directly and indirectly involved in the progress of my work.

As creative advancement rarely develops without the right social environment, I am very grateful for the numerous wonderful encounters and new friendships that generated a welcoming working atmosphere. Therefore, I would like to thank Nikki, Paolo, Max, and Julya for being the very best office mates. But also Vale, Ralf, Milena, Baris, Majd, José, Francesco, and many more created memorable moments, made tough times bearable, and kept my personal happiness index on a high level.

Finally, I am very grateful to my family for their support and their enduring encouragement. They always showed genuine interest and excitement for my research.

# LIST OF TABLES

Table 1-1: Twelve top value-added chemicals as building blocks for biorefinery, according to the U.S. Dept. of Energy <sup>5</sup> .....	3
Table 1-2: Fuel properties of bioethanol, DMF, and gasoline .....	4
Table 3-1: Composition of precursor dough for the ZnCl <sub>2</sub> approach. MC: microcrystalline .....	28
Table 3-2: Elemental composition of pellets prepared on the ZnCl <sub>2</sub> route, before (C <sub>ZnCl-500</sub> ) and after (C <sub>ZnCl-500L</sub> ) washing. <i>a</i> : measured by combustion elemental analysis; <i>b</i> : measured by inductively coupled plasma (ICP) .....	30
Table 3-3: Nitrogen physisorption data of carbon support pellets (2.4 × 3.5 mm) prepared on the ZnCl <sub>2</sub> route after washing. ....	31
Table 3-4: Composition of precursor dough for the NaCl approach with a weight ratio of 8:3 for NaCl:semolina .....	31
Table 3-5: Elemental composition of pellets prepared on the NaCl route, before (C <sub>NaCl-500</sub> ) and after (C <sub>NaCl-500L</sub> ) washing. <i>a</i> : measured by combustion elemental analysis; <i>b</i> : measured by IR elemental oxygen analysis; <i>c</i> : measured by inductively coupled plasma (ICP) .....	32
Table 3-6: Nitrogen physisorption data of carbon support pellets (2.4 × 3.5 mm) prepared on the NaCl route after washing. ....	33
Table 3-7: Composition of precursor dough for the ZnO approach .....	34
Table 3-8: Elemental composition of pellets (2.4 × 3.5 mm) prepared on the ZnO route. <i>a</i> : measured by combustion elemental analysis; <i>b</i> : measured by elemental oxygen analysis; <i>c</i> : measured by inductively coupled plasma (ICP) ....	36
Table 3-9: Nitrogen physisorption data of carbon support pellets (2.4 × 3.5 mm) prepared on the ZnO route at 800 and 950 °C, before and after leaching. ....	38
Table 3-10: Elemental composition of carbon support pellets (2.4 × 3.5 mm) prepared on the ZnO route (C <sub>ZnO-950L</sub> ) and catalysts supported on the pellets with different Ni loadings (Ni/C <sub>ZnO-950L</sub> , abbreviated by Ni/C). <i>a</i> : measured by combustion elemental analysis; <i>b</i> : measured by inductively coupled plasma (ICP) .....	40
Table 3-11: Nitrogen physisorption data of the C <sub>ZnO-950L</sub> carbon support pellets (2.4 × 3.5 mm) compared to catalyst pellets based on the C <sub>ZnO-950L</sub> support with incorporated Ni nanoparticles of different loading .....	41
Table 3-12: Analysis of Ni and NiO nanoparticle and crystallite size of the reduced 21wt% Ni/C catalyst and of its precursor before reduction; <i>a</i> : determined from particle size distribution on TEM images; <i>b</i> : determined as average value of three mean crystallite sizes calculated from the three main peaks in the XRD diffractogram .....	44
Table 3-13: Analysis of Ni nanoparticle and crystallite size of catalyst pellets with different Ni loadings (Ni/C <sub>ZnO-950L</sub> , abbreviated by Ni/C); <i>a</i> : determined from particle size distribution on TEM images; <i>b</i> : determined as average value of three mean crystallite sizes calculated from the three main peaks in the XRD diffractogram .....	45
Table 3-14: Ni and Pt salt, used for incipient wetness impregnation, and applied heat treatment programs for metal nanoparticle synthesis on the supports. The heat treatment of each calcination and reduction step was preceded by 0:30 waiting time and 1:00 preheating at 90 °C (3 K min <sup>-1</sup> ) .....	46
Table 3-15: Nitrogen physisorption data of the C <sub>ZnO-950L</sub> carbon support pellets (2.4 × 3.5 mm) compared to catalyst pellets based on the C <sub>ZnO-950L</sub> support with incorporated Pt nanoparticles of different loading .....	47
Table 3-16: Analysis of Pt nanoparticle size distribution of catalyst pellets with different Pt loadings (Pt/C <sub>ZnO-950L</sub> , abbreviated by Pt/C), determined from particle size distribution on TEM images .....	47
Table 3-17: Nitrogen physisorption data of granular (1-5mm) polystyrene before sulfonation ("neutral"). ....	50
Table 3-18: Nitrogen physisorption data of 10wt% ZrO <sub>2</sub> -Al <sub>2</sub> O <sub>3</sub> (1.6 × 3 mm). ....	51
Table 4-1: Dimensions of packed-bed reactors used with the flow set-up, compared with the particle size of the synthesized 2.4 × 3.5 mm catalyst pellets .....	56
Table 5-1: Yields of four intermediates of HMF conversion over 21wt% Ni/C (2.4 × 3.5mm) at lowest space time (0.11 h g <sub>Ni</sub> g <sub>HMF</sub> <sup>-1</sup> ). Conditions: 0.1M HMF in EtOH reactant solution, 150 °C, 20 bar H <sub>2</sub> pressure, H <sub>2</sub> :HMF 7.5:1. ....	75

Table 5-2: Nitrogen physisorption data of the 21wt% Ni/C catalyst before reaction and after 35 h time on stream of HMF hydrodeoxygenation reaction in EtOH. ....	86
Table 5-3: Ni loading of 21 and 16wt% Ni/C before and after HMF hydrogenation reaction in EtOH. <i>a</i> : measured by inductively coupled plasma (ICP) ....	88
Table 5-4: Ni crystallite size of the 21wt% Ni/C catalyst before and after 35 h TOS of HMF hydrogenation in EtOH; <i>a</i> : determined as average value of three mean crystallite sizes calculated from the three main peaks in the XRD diffractogram ....	88
Table 5-5: Arrhenius parameters fitted to the observed kinetics of LA consumption. Conditions as specified in Figure 5-23. ....	92
Table 5-6: Analysis of Ni nanoparticle and crystallite size of the 21wt% Ni/C catalyst before and after 15 h time on stream of LA hydrogenation in water; <i>a</i> : determined from particle size distribution on TEM images; <i>b</i> : determined as average value of three mean crystallite sizes calculated from the three main peaks in the XRD diffractogram; <i>c</i> : measured by inductively coupled plasma (ICP) ....	101



## LIST OF FIGURES

Figure 1-1: Main components of lignocellulosic biomass .....	2
Figure 1-2: Graphical outline of the present work. HMF: 5-hydroxymethylfurfural; LA: levulinic acid; DMF: 2,5-dimethylfuran; GVL: $\gamma$ -valerolactone .....	6
Figure 2-1: The 12 principles of green chemistry, according to the ACS Green Chemistry Pocket Guide <sup>16</sup> .....	8
Figure 2-2: Structure and constituents of LCB. Adapted from Isikgor and Becer <sup>8</sup> and edited.....	9
Figure 2-3: O/C and H/C molar ratio for biobased and petroleum-based products. Adapted from Rinaldi and Schüth <sup>23</sup> .....	11
Figure 2-4: Scheme of acid-catalyzed fructose dehydration to HMF with consecutive hydrolysis and decomposition to levulinic acid and formic acid. Adapted from Qi <i>et al.</i> <sup>37</sup> and edited. ....	13
Figure 2-5: Major contributors to DMF price. Adapted from Kazi <i>et al.</i> <sup>45</sup> .....	14
Figure 2-6: Proposed pathways for HMF production from fructose and glucose. Adapted from Lin <i>et al.</i> <sup>30</sup> and edited. ....	15
Figure 2-7: Simplified reaction scheme of hexose conversion towards DMF .....	18
Figure 2-8: Reaction pathways for the production of GVL from LA, adapted from Alonso <i>et al.</i> <sup>64</sup> .....	20
Figure 3-1: Extrusion of the carbon support precursor through pasta machine. left: extrusion of uncut spaghetti shape; right: automatic pellet cutting during extrusion by rotating cutting knife .....	26
Figure 3-2: Scheme for the synthesis of porous carbon pellets on the ZnCl <sub>2</sub> route .....	29
Figure 3-3: Precursor pellets of the carbon support prepared on the ZnCl <sub>2</sub> –urea–glucose route after extrusion (left), after preheating at 100 °C (second from left), and final carbon support pellets after carbonization and washing (third from left), compared with commercial Ni/C–Al <sub>2</sub> O <sub>3</sub> catalyst extrudates (right) .....	29
Figure 3-4: N <sub>2</sub> physisorption isotherms (left) and pore size distribution (right) of carbon support pellets (2.4 × 3.5 mm) prepared on the ZnCl <sub>2</sub> route after washing. Measurement conducted at 77.3 K. Calculation of pore size distribution based on QSDFT adsorption method on carbon with slit, cylindrical, and spherical pores. ....	30
Figure 3-5: Scheme for the synthesis of porous carbon pellets on the NaCl route .....	32
Figure 3-6: Carbon precursor pellets synthesized on the NaCl route. left: placed in crucibles, ready for carbonization; right: after carbonization .....	32
Figure 3-7: N <sub>2</sub> physisorption isotherms (left) and pore size distribution (right) of carbon support pellets (2.4 × 3.5 mm) prepared on the NaCl route after washing. Measurement conducted at 77.3 K. Calculation of pore size distribution based on QSDFT adsorption method on carbon with slit, cylindrical, and spherical pores. ....	33
Figure 3-8: Scheme for the synthesis of porous carbon pellets on the ZnO route .....	35
Figure 3-9: N <sub>2</sub> physisorption isotherms (top) and pore size distribution over volume (middle) and surface area (bottom) of carbon support pellets (2.4 × 3.5 mm) prepared on the ZnO route at 800 °C (left) and 950 °C (right), before and after leaching. Measurements conducted at 77.3 K. Calculation of pore size distribution based on QSDFT adsorption method on carbon with slit, cylindrical, and spherical pores. ....	37
Figure 3-10: Precursor pellets prepared on the ZnO route before and after carbonization .....	38
Figure 3-11: Scheme for the Ni nanoparticle incorporation on the support pellets .....	40
Figure 3-12: N <sub>2</sub> physisorption isotherms (top) and pore size distribution over volume (bottom left) and surface area (bottom right) of the C <sub>ZnO-950L</sub> carbon support pellets (2.4 × 3.5 mm), compared to catalyst pellets based on the C <sub>ZnO-950L</sub> support with incorporated Ni nanoparticles of different loading. Measurements conducted at 77.3 K. Calculation of pore size distribution based on QSDFT adsorption method on carbon with slit, cylindrical, and spherical pores. ....	41
Figure 3-13: XRD diffractograms of the C <sub>ZnO-950L</sub> carbon support, the “21wt% Ni/C” precursor before reduction, and the final 21wt% Ni/C catalyst .....	42
Figure 3-14: TEM images (top) and particle size distribution (bottom) of the 21wt% Ni/C pellets before (left) and after (right) reduction. ....	43

Figure 3-15: TEM images in low (top) and high (middle) magnification and particle size distribution (bottom) of the 5wt%, 21wt%, and 29wt% Ni/C catalyst. ....	45
Figure 3-16: SEM images of the cross-section surface of the 21wt% Ni/C catalyst pellet.....	46
Figure 3-17: N <sub>2</sub> physisorption isotherms (left) and pore size distribution (right) of the C <sub>ZnO-950L</sub> carbon support pellets (2.4 × 3.5 mm), compared to catalyst pellets based on the C <sub>ZnO-950L</sub> support with incorporated Pt nanoparticles of different loading. Measurements conducted at 77.3 K. Calculation of pore size distribution based on QSDFT adsorption method on carbon with slit, cylindrical, and spherical pores. ....	47
Figure 3-18: TEM images in low (top) and high (middle) magnification and particle size distribution (bottom) of the 0.5wt%, 0.8wt%, and 2.7wt% Pt/C catalyst. ....	48
Figure 3-19: N <sub>2</sub> physisorption isotherms (left) and pore size distribution (right) of granular (1-5mm) polystyrene (“PS”) before sulfonation (“neutral”). Measurement conducted at 77.3 K. Calculation of pore size distribution based on QSDFT adsorption method on carbon with slit, cylindrical, and spherical pores. ....	49
Figure 3-20: N <sub>2</sub> physisorption isotherms (left) and pore size distribution (right) of 10wt% ZrO <sub>2</sub> -Al <sub>2</sub> O <sub>3</sub> (1.6 × 3 mm). Measurement conducted at 77.3 K. Calculation of pore size distribution based on NLDFT adsorption method on “zeolite” with cylindrical and spherical pores. ....	50
Figure 4-1: Implemented continuous flow set-up with large packed-bed reactor (OD1.5inch) .....	54
Figure 4-2: Piping and instrumentation diagram (P&ID) of the continuous flow set-up. FC: flow control; PI: pressure indication; TI/TC: temperature indication/control .....	56
Figure 4-3: Size adjustments of the continuous flow set-up. left: heating coil with high cooling capacity. right: Downsized set-up with OD11mm reactor and decreased dead volume in the outlet .....	57
Figure 4-4: Three quartz tubes (ID 7 mm) filled with 2.4 × 3.5 mm catalyst pellets. middle: subsequently filled with SiC (840-1190 μm); bottom: subsequently filled with pure HCl-washed sea sand (100-315 μm) .....	59
Figure 5-1: Reaction scheme of catalyzed processes presented in this section .....	61
Figure 5-2: Product yields for the conversion of fructose over granular (1-5mm) sulfonated polystyrene-divinylbenzene, as a function of space time. Conditions: 0.1M fructose in H <sub>2</sub> O reactant solution, 150 °C (left) and 130 °C (right) .....	64
Figure 5-3: Product yields (left) and selectivities (right) for the conversion of glucose over 10wt% ZrO <sub>2</sub> -Al <sub>2</sub> O <sub>3</sub> (1.6 × 3 mm), as a function of temperature. Conditions: 0.1M glucose in H <sub>2</sub> O reactant solution, space time of 3.3 h g <sub>ZrO<sub>2</sub></sub> <sup>-1</sup> , 25 bar .....	65
Figure 5-4: Decomposition of glucose and fructose by base-catalyzed <i>retro</i> -aldol reaction. Adapted from Onda <i>et al.</i> <sup>103</sup> . ...	66
Figure 5-5: Product yields for the catalytic conversion of glucose over 10wt% ZrO <sub>2</sub> -Al <sub>2</sub> O <sub>3</sub> (1.6 × 3 mm), as a function of space time. Conditions: 0.1M glucose in H <sub>2</sub> O reactant solution, 150 °C, 25 bar. ....	67
Figure 5-6: Bed packing of bicatalytic reactor with 10wt% ZrO <sub>2</sub> -Al <sub>2</sub> O <sub>3</sub> (1.6×3 mm) and granular (1-5mm) polystyrene sulfonate (“PSS”). Packed bed consists of 75vol.% ZrO <sub>2</sub> -Al <sub>2</sub> O <sub>3</sub> and 25vol.% PSS. Dimensions of “OD1inch_1” reactor (see section 4.1): 21×80 mm (ID×L), cross-sectional (“QS”) area of bed 352 mm <sup>2</sup> . left: profile of relative QS areas of the catalysts along reactor axis; middle: photos of several cross-sections, taken during bed packing; right: scheme of catalyst distribution. ....	68
Figure 5-7: Product yields for the catalytic conversion of glucose in a bicatalytic reactor with 10wt% ZrO <sub>2</sub> -Al <sub>2</sub> O <sub>3</sub> (1.6 × 3 mm) and granular (1-5mm) sulfonated polystyrene-divinylbenzene, as a function of space time. Conditions: 0.1M glucose in H <sub>2</sub> O reactant solution, 130 °C, 20 bar. ....	69
Figure 5-8: Product yields for the catalytic conversion of glucose in a bicatalytic reactor with 10wt% ZrO <sub>2</sub> -Al <sub>2</sub> O <sub>3</sub> (1.6 × 3 mm) and granular (1-5mm) sulfonated polystyrene-divinylbenzene, as a function of space time. Conditions: 0.1M glucose in H <sub>2</sub> O reactant solution, 110 °C, 20 bar. ....	69
Figure 5-9: Reductive steps of HMF deoxygenation to DMF and consecutive reactions .....	71
Figure 5-10: Proposed reaction scheme for HMF hydrodeoxygenation in ethanol, including the main hydrogenation steps (highlighted in grey), parallel side reactions with the solvent, and consecutive reactions of DMF. This scheme is deduced from GC-MS analysis. ....	72
Figure 5-11: Effect of space time on yield in HMF hydrogenation over 21wt% Ni/C (2.4 × 3.5mm). Conditions: 0.1M HMF in EtOH reactant solution, 150 °C, 20 bar H <sub>2</sub> pressure, H <sub>2</sub> :HMF 7.5:1; left: whole range of investigated space time; right: enlarged section for low space time .....	73

Figure 5-12: Reaction of HMF, 5-MF, BHMF, and MFA in ethanol solution and absence of H <sub>2</sub> . Initial concentration 14 mL reactant solution: 25 mmol L <sup>-1</sup> in HMF, 5-MF, BHMF, and MFA in ethanol. Conditions: 1.12 g <sub>cat</sub> (0.23 g <sub>Ni</sub> ), 1 h reaction time at 150 °C (equivalent to space time of 1.33 h g <sub>Ni</sub> g <sub>HMF</sub> <sup>-1</sup> in continuous flow hydrogenation) .....	74
Figure 5-13: Effect of space time on selectivity (left) and Ni time yield (right) in HMF hydrogenation. Conditions: 0.1M HMF in EtOH reactant solution, 21wt% Ni/C (2.4 × 3.5 mm), 150 °C, 20 bar H <sub>2</sub> , H <sub>2</sub> :HMF 7.5:1 .....	76
Figure 5-14: Time-on-stream evolution of yield and Ni space time in HMF hydrogenation. left: intermediate derivatives of same reduction level grouped together; right: derivatives displayed separately in enlarged diagram. Conditions: 0.1M HMF in EtOH reactant solution, 21wt% Ni/C (2.4 × 3.5mm), space time of 1.33 h g <sub>Ni</sub> g <sub>HMF</sub> <sup>-1</sup> , 150 °C, 20 bar H <sub>2</sub> pressure, H <sub>2</sub> :HMF 7.5:1 .....	77
Figure 5-15: Effect of H <sub>2</sub> pressure (left) and H <sub>2</sub> :HMF molar ratio (right) on yield and Ni time yield in HMF hydrogenation. Conditions: 0.1M HMF in EtOH reactant solution, 21wt% Ni/C pellets (2.4 × 3.5mm), 150 °C, space time of 2.66 (left) and 1.33 (right) h g <sub>Ni</sub> g <sub>HMF</sub> <sup>-1</sup> , H <sub>2</sub> :HMF 7.5:1 (left), 20 bar H <sub>2</sub> (right) .....	80
Figure 5-16: Effect of temperature on yield and Ni time yield in HMF hydrogenation. left: derivatives of same reduction level grouped together; right: derivatives displayed separately in enlarged scale of low yield. Conditions: 0.1M HMF in EtOH reactant solution, 21wt% Ni/C pellets (2.4 × 3.5mm), space time of 1.33 h g <sub>Ni</sub> g <sub>HMF</sub> <sup>-1</sup> , 20 bar H <sub>2</sub> , H <sub>2</sub> :HMF 7.5:1 .....	81
Figure 5-17: Yield, cumulative yield, and hypothetical conversion of BHMF and EMHMF over temperature. Conditions according to Figure 5-16 .....	83
Figure 5-18: Possible pathways for the formation of DMTHF and hexane-2,5-diol from DMF .....	84
Figure 5-19: N <sub>2</sub> physisorption isotherms (left) and pore size distribution (right) of the 21wt% Ni/C catalyst before reaction and after 35 h time on stream. Measurements conducted at 77.3 K. Calculation of pore size distribution based on QSDFT adsorption method on carbon with slit, cylindrical, and spherical pores. ....	85
Figure 5-20: Effect of space time (left) and temperature (right) on conversion and yield in HMF hydrogenation over 16wt% Ni/C catalyst pellets (2.4 × 3.5mm). Conditions: 0.05M HMF in EtOH reactant solution, 20 bar H <sub>2</sub> , H <sub>2</sub> :HMF 15:1; left: 150 °C, compared to DMF yield over 21wt% Ni/C from 0.1M HMF solution with H <sub>2</sub> :HMF 7.5:1; right: space time of 0.77 h g <sub>Ni</sub> g <sub>HMF</sub> <sup>-1</sup> .....	87
Figure 5-21: Effect of temperature on conversion, yield, and Pt time yield (left) as well as selectivity (right) in LA hydrogenation over 2.7wt% Pt/C (2.4 × 3.5mm). Conditions: 0.1M LA in H <sub>2</sub> O, space time of 0.079 h g <sub>Pt</sub> g <sub>LA</sub> <sup>-1</sup> , 50 bar H <sub>2</sub> , H <sub>2</sub> :LA 5:1 .....	89
Figure 5-22: Suggested reaction scheme of LA hydrogenation, including parallel and consecutive reactions to byproducts .....	90
Figure 5-23: Effect of space time on conversion, yield, and Pt time yield of GVL (left) as well as selectivity (right) in LA hydrogenation over 2.7wt% Pt/C (2.4 × 3.5mm). Conditions: 0.1M LA in H <sub>2</sub> O, 160 °C, 50 bar H <sub>2</sub> , H <sub>2</sub> :LA 5:1 .....	91
Figure 5-24: Measurements and fitted kinetic model for conversion, GVL yield, and Pt time yield in the LA hydrogenation over 2.7wt% Pt/C (2.4 × 3.5mm). Effect of temperature (left) and space time (right). Conditions: 0.1M LA in H <sub>2</sub> O, 50 bar H <sub>2</sub> , H <sub>2</sub> :LA 5:1, space time of 0.079 h g <sub>Pt</sub> g <sub>LA</sub> <sup>-1</sup> (left), 160 °C (right) .....	93
Figure 5-25: Effect of temperature on conversion, yield, and Pt time yield of main products (left) as well as selectivity (right) in LA hydrogenation over 2.7wt% Pt/C (2.4 × 3.5mm). Conditions: 50 bar, 0.1M LA and 0.5M FA in H <sub>2</sub> O reactant solution (FA:LA 5:1), space time of 0.079 h g <sub>Pt</sub> g <sub>LA</sub> <sup>-1</sup> ; left: compared with H <sub>2</sub> -assisted hydrogenation conducted under the same conditions (50 bar H <sub>2</sub> ; H <sub>2</sub> :LA 5:1) .....	93
Figure 5-26: Effect of space time on conversion, yield, and Pt time yield of main products (left) and selectivity (right) in LA hydrogenation over 2.7wt% Pt/C (2.4 × 3.5mm). Conditions: 220 °C, 50 bar, 0.1M LA and 0.5M FA in H <sub>2</sub> O reactant solution (FA:LA 5:1) .....	94
Figure 5-27: Effect of space time on conversion, yield, and Pt time yield of main products (left) and selectivity (right) in LA hydrogenation over 2.7wt% Pt/C (2.4 × 3.5mm). Conditions: 260 °C, 50 bar, 0.1M LA and 0.5M FA in H <sub>2</sub> O reactant solution (FA:LA 5:1) .....	95
Figure 5-28: Effect of pressure (left) and temperature (right) on conversion, yield, and Pt time yield of main products in LA hydrogenation over 0.8wt% Pt/C (space time of 0.048 h g <sub>Pt</sub> g <sub>LA</sub> <sup>-1</sup> ). left: compared with 2.7wt% Pt/C (space time of 0.079 h g <sub>Pt</sub> g <sub>LA</sub> <sup>-1</sup> ). Conditions: 0.1M LA and 0.5M FA in H <sub>2</sub> O reactant solution (FA:LA 5:1), 220 °C (left), 20 bar (right) .....	96

Figure 5-29: Effect of space time on conversion and yield (left) as well as selectivity and Pt time yield (right) of main products in LA hydrogenation over 0.8wt% Pt/C. left: compared with 2.7wt% Pt/C. Conditions: 0.1M LA and 0.5M FA in H <sub>2</sub> O reactant solution (FA:LA 5:1), 220 °C, 20 bar	97
Figure 5-30: Effect of space time on conversion and yield (left) as well as selectivity and Pt time yield (right) of main products in LA hydrogenation over 0.5wt% Pt/C. left: compared with 2.7wt% Pt/C. Conditions: 0.1M LA and 0.5M FA in H <sub>2</sub> O reactant solution (FA:LA 5:1), 260 °C, 50 bar	97
Figure 5-31: Time on stream evolution for conversion, yield, and Pt time yield for main products in LA hydrogenation over 2.7wt% Pt/C (2.4 × 3.5mm). Conditions, 0.1M LA and 0.5M FA in H <sub>2</sub> O reactant solution (FA:LA 5:1), space time of 0.079 h g <sub>Pt</sub> g <sub>LA</sub> <sup>-1</sup> , 50 bar	98
Figure 5-32: Effect of space time on conversion and yield (left) as well as Ni time yield (right) of main products in LA hydrogenation over 5wt%, 21wt%, and 29wt% Ni/C. Conditions: 0.1M LA and 0.5M FA in H <sub>2</sub> O reactant solution (FA:LA 5:1), 220 °C, 20 bar	99
Figure 5-33: Effect of space time (left) and temperature (right) on conversion and yield of main products in LA hydrogenation over 21wt% Ni/C. right: compared with 29wt% Ni/C. Conditions: 0.1M LA and 0.5M FA in H <sub>2</sub> O reactant solution (FA:LA 5:1), 260 °C, 50 (left) and 40 (right) bar; right: space time of 1.21 (1.67) h g <sub>Ni</sub> g <sub>LA</sub> <sup>-1</sup> for 21wt% (29wt%) Ni/C	100
Figure 5-34: Time on stream evolution of conversion and GVL yield in LA hydrogenation over 21wt% and 29wt% Ni/C at 220 and 260 °C. Conditions: 0.1M LA and 0.5M FA in H <sub>2</sub> O reactant solution (FA:LA 5:1), space time of 1.21 (left, right) and 1.67 (middle) h g <sub>Ni</sub> g <sub>LA</sub> <sup>-1</sup> , 40 bar (left, middle) and 50 bar (right)	100
Figure 5-35: TEM images (left, middle) and Ni particle size distribution (right) of the (originally) 21wt% Ni/C pellets after 15 h time on stream of LA hydrogenation in water; right: compared with fresh catalyst before reaction	101
Figure 5-36: XRD diffractograms of the 21wt% Ni/C catalyst before and after 15 h time on stream of LA hydrogenation in water	102
Figure A-1: Böhm titration of the polystyrene sulfonate (PSS). Analyte: 51.62 mg of material in 10mL 0.05M NaOH solution, stirred overnight, thereof 8 mL filtered through 0.2 µm PP syringe filter. Equivalence point reached at 5.338 mL of 0.05M HCl titrated.	110
Figure A-2: left: Böhm titration of the 21wt% Ni/C catalyst. Analyte: 252.40 (251.75) mg of pellets before (after) 35 h TOS (HMF hydrogenation in EtOH). Preparation of analyte: 10mL 0.05M NaOH solution, stirred overnight, thereof 8 mL filtered through 0.2 µm PP syringe filter; right: T and molar fractions of the associated species of Zn <sup>2+</sup> and OH <sup>-</sup> over pH in equilibrium at 25 °C (right), adapted from Reichle <i>et al.</i> <sup>97</sup>	111

## REFERENCES

- (1) Deffeyes, K. S. *Hubbert's Peak - The Impending World Oil Shortage - New Edition*; 2008.
- (2) Cherubini, F. The Biorefinery Concept: Using Biomass Instead of Oil for Producing Energy and Chemicals. *Energy Convers. Manag.* **2010**, *51* (7), 1412–1421. <https://doi.org/10.1016/j.enconman.2010.01.015>.
- (3) Alonso, D. M.; Bond, J. Q.; Dumesic, J. A. Catalytic Conversion of Biomass to Biofuels. *Green Chem.* **2010**, *12* (9), 1493–1513. <https://doi.org/10.1039/c004654j>.
- (4) Holzman, D. C. The Carbon Footprint of Biofuels Can We Shrink It down to Size in Time? *Environ. Health Perspect.* **2008**, *116* (6). <https://doi.org/10.1289/ehp.116-a246>.
- (5) Werpy, T.; Petersen, G. *Top Value Added Chemicals from Biomass: Volume I -- Results of Screening for Potential Candidates from Sugars and Synthesis Gas*; Golden, CO (United States), 2004. <https://doi.org/10.2172/15008859>.
- (6) Tong, X.; Ma, Y.; Li, Y. Biomass into Chemicals: Conversion of Sugars to Furan Derivatives by Catalytic Processes. *Appl. Catal. A Gen.* **2010**, *385* (1–2), 1–13. <https://doi.org/10.1016/j.apcata.2010.06.049>.
- (7) Chang, C. C.; Green, S. K.; Williams, C. L.; Dauenhauer, P. J.; Fan, W. Ultra-Selective Cycloaddition of Dimethylfuran for Renewable p-Xylene with H-BEA. *Green Chem.* **2014**, *16* (2), 585–588. <https://doi.org/10.1039/c3gc40740c>.
- (8) Isikgor, F. H.; Becer, C. R. Lignocellulosic Biomass: A Sustainable Platform for the Production of Bio-Based Chemicals and Polymers. *Polym. Chem.* **2015**, *6* (25), 4497–4559. <https://doi.org/10.1039/C5PY00263J>.
- (9) Tenenbaum, D. J. Food vs. Fuel: Diversion of Crops Could Cause More Hunger. *Environ. Health Perspect.* **2008**, *116* (6), 254–257. <https://doi.org/10.1289/ehp.116-a254>.
- (10) Thananattathanachon, T.; Rauchfuss, T. B. Efficient Production of the Liquid Fuel 2,5-Dimethylfuran from Fructose Using Formic Acid as a Reagent. *Angew. Chemie - Int. Ed.* **2010**, *49* (37), 6616–6618. <https://doi.org/10.1002/anie.201002267>.
- (11) Zhong, S.; Daniel, R.; Xu, H.; Zhang, J.; Turner, D.; Wyszynski, M. L.; Richards, P. Combustion and Emissions of 2,5-Dimethylfuran in a Direct-Injection Spark-Ignition Engine. *Energy and Fuels* **2010**, *24* (5), 2891–2899. <https://doi.org/10.1021/ef901575a>.
- (12) Moore, J. S.; Jensen, K. F. “Batch” Kinetics in Flow: Online IR Analysis and Continuous Control. *Angew. Chemie Int. Ed.* **2014**, *53* (2), 470–473. <https://doi.org/10.1002/anie.201306468>.
- (13) DeMello, A. J. Control and Detection of Chemical Reactions in Microfluidic Systems. *Nature* **2006**, *442* (7101), 394–402. <https://doi.org/10.1038/nature05062>.
- (14) Berntsson, T.; Sanden, B.; Olsson, L.; Asblad, A. What Is a Biorefinery? *Syst.*

- Perspect. Biorefineries* **2014**, No. 2008, 16–25.  
[https://doi.org/http://dx.doi.org/10.1016/S0040-6090\(97\)01110-3](https://doi.org/http://dx.doi.org/10.1016/S0040-6090(97)01110-3).
- (15) Ghatak, H. R. Biorefineries from the Perspective of Sustainability: Feedstocks, Products, and Processes. *Renew. Sustain. Energy Rev.* **2011**, *15* (8), 4042–4052.  
<https://doi.org/10.1016/j.rser.2011.07.034>.
- (16) Green Chemistry Pocket Guide - The 12 Principles of Green Chemistry. American Chemical Society.
- (17) Palmeros Parada, M.; Osseweijer, P.; Posada Duque, J. A. Sustainable Biorefineries, an Analysis of Practices for Incorporating Sustainability in Biorefinery Design. *Ind. Crops Prod.* **2017**, *106*, 105–123. <https://doi.org/10.1016/j.indcrop.2016.08.052>.
- (18) Edwards, R.; Padella, M.; Giuntoli, J.; Koebler, R.; O’Connell, A.; Bulgheroni, C.; Marelli, L. *JRC Science for Policy Report - Definition of Input Data to Assess GHG Default Emissions from Biofuels in EU Legislation*; 2017.
- (19) Mountraki, A.; Tsakalova, M.; Panteli, A.; Papoutsis, A. I.; Kokossis, A. C. Integrated Waste Management in Multiproduct Biorefineries: Systems Optimization and Analysis of a Real-Life Industrial Plant. *Ind. Eng. Chem. Res.* **2016**, *55* (12), 3478–3492.  
<https://doi.org/10.1021/acs.iecr.5b03431>.
- (20) Agbor, V. B.; Cicek, N.; Sparling, R.; Berlin, A.; Levin, D. B. Biomass Pretreatment: Fundamentals toward Application. *Biotechnol. Adv.* **2011**, *29* (6), 675–685.  
<https://doi.org/10.1016/j.biotechadv.2011.05.005>.
- (21) Lu, F.; Ralph, J. Lignin. In *Cereal Straw as a Resource for Sustainable Biomaterials and Biofuels*; John Wiley & Sons, Inc.: Hoboken, NJ, USA, 2010; pp 169–207.  
<https://doi.org/10.1016/B978-0-444-53234-3.00006-7>.
- (22) Abdel-Hamid, A. M.; Solbiati, J. O.; Cann, I. K. O. *Insights into Lignin Degradation and Its Potential Industrial Applications*; Elsevier, 2013; Vol. 82.  
<https://doi.org/10.1016/B978-0-12-407679-2.00001-6>.
- (23) Rinaldi, R.; Schüth, F. Design of Solid Catalysts for the Conversion of Biomass. *Energy Environ. Sci.* **2009**, *2* (6), 610–626. <https://doi.org/10.1039/b902668a>.
- (24) Román-Leshkov, Y.; Barrett, C. J.; Liu, Z. Y.; Dumesic, J. A. Production of Dimethylfuran for Liquid Fuels from Biomass-Derived Carbohydrates. *Nature* **2007**, *447* (7147), 982–985. <https://doi.org/10.1038/nature05923>.
- (25) Barakat, A.; de Vries, H.; Rouau, X. Dry Fractionation Process as an Important Step in Current and Future Lignocellulose Biorefineries: A Review. *Bioresour. Technol.* **2013**, *134*, 362–373. <https://doi.org/10.1016/j.biortech.2013.01.169>.
- (26) Taherzadeh, M. J.; Karimi, K. *Pretreatment of Lignocellulosic Wastes to Improve Ethanol and Biogas Production: A Review*; 2008; Vol. 9.  
<https://doi.org/10.3390/ijms9091621>.
- (27) Mosier, N.; Wyman, C.; Dale, B.; Elander, R.; Lee, Y. Y.; Holtzapple, M.; Ladisch, M. Features of Promising Technologies for Pretreatment of Lignocellulosic Biomass. *Bioresour. Technol.* **2005**, *96* (6), 673–686.  
<https://doi.org/10.1016/j.biortech.2004.06.025>.
- (28) Zviely, M. Converting Lignocellulosic Biomass to Low-Cost Fermentable Sugars. In



- Pretreatment Techniques for Biofuels and Biorefineries*; Fang, Z., Ed.; 2013; pp 133–150. [https://doi.org/10.1007/978-3-642-32735-3\\_7](https://doi.org/10.1007/978-3-642-32735-3_7).
- (29) Mukherjee, A.; Dumont, M. J.; Raghavan, V. Review: Sustainable Production of Hydroxymethylfurfural and Levulinic Acid: Challenges and Opportunities. *Biomass and Bioenergy* **2015**, *72*, 143–183. <https://doi.org/10.1016/j.biombioe.2014.11.007>.
- (30) Hu, L.; Zhao, G.; Hao, W.; Tang, X.; Sun, Y.; Lin, L.; Liu, S. Catalytic Conversion of Biomass-Derived Carbohydrates into Fuels and Chemicals via Furanic Aldehydes. *RSC Adv.* **2012**, *2* (30), 11184–11206. <https://doi.org/10.1039/c2ra21811a>.
- (31) Rinaldi, R.; Meine, N.; vom Stein, J.; Palkovits, R.; Schüth, F. Which Controls the Depolymerization of Cellulose in Ionic Liquids: The Solid Acid Catalyst or Cellulose? *ChemSusChem* **2010**, *3* (2), 266–276. <https://doi.org/10.1002/cssc.200900281>.
- (32) Huang, Y. B.; Fu, Y. Hydrolysis of Cellulose to Glucose by Solid Acid Catalysts. *Green Chem.* **2013**, *15* (5), 1095–1111. <https://doi.org/10.1039/c3gc40136g>.
- (33) Shuai, L.; Pan, X. Hydrolysis of Cellulose by Cellulase-Mimetic Solid Catalyst. *Energy Environ. Sci.* **2012**, *5* (5), 6889–6894. <https://doi.org/10.1039/c2ee03373a>.
- (34) Bin Yang; Ziyu Dai; Shi-You Ding; Charles E Wyman. Enzymatic Hydrolysis of Cellulosic Biomass. *Biofuels* **2011**, *2* (4), 421–449. <https://doi.org/10.4155/BFS.11.116>.
- (35) Okazaki, M.; Moo-Young, M. Kinetics of Enzymatic Hydrolysis of Cellulose: Analytical Description of a Mechanistic Model. *Biotechnol. Bioeng.* **1978**, *20* (5), 637–663. <https://doi.org/10.1002/bit.260200503>.
- (36) Foo, G. S.; Van Pelt, A. H.; Krötschel, D.; Sauk, B. F.; Rogers, A. K.; Jolly, C. R.; Yung, M. M.; Sievers, C. Hydrolysis of Cellobiose over Selective and Stable Sulfonated Activated Carbon Catalysts. *ACS Sustain. Chem. Eng.* **2015**, *3* (9), 1934–1942. <https://doi.org/10.1021/acssuschemeng.5b00530>.
- (37) Qi, X.; Watanabe, M.; Aida, T. M.; Smith, R. L. Efficient Process for Conversion of Fructose to 5-Hydroxymethylfurfural with Ionic Liquids. *Green Chem.* **2009**, *11* (9), 1327–1331. <https://doi.org/10.1039/b905975j>.
- (38) Kuster, B. F. M. 5-Hydroxymethylfurfural (HMF). A Review Focussing on Its Manufacture. *Starch - Stärke* **1990**, *42* (8), 314–321. <https://doi.org/10.1002/star.19900420808>.
- (39) Luo, W.; Deka, U.; Beale, A. M.; van Eck, E. R. H.; Bruijninx, P. C. A.; Weckhuysen, B. M. Ruthenium-Catalyzed Hydrogenation of Levulinic Acid: Influence of the Support and Solvent on Catalyst Selectivity and Stability. *J. Catal.* **2013**, *301*, 175–186. <https://doi.org/10.1016/j.jcat.2013.02.003>.
- (40) Antonetti, C.; Raspolli Galletti, A. M.; Fulignati, S.; Licursi, D. Amberlyst A-70: A Surprisingly Active Catalyst for the MW-Assisted Dehydration of Fructose and Inulin to HMF in Water. *Catal. Commun.* **2017**, *97* (April), 146–150. <https://doi.org/10.1016/j.catcom.2017.04.032>.
- (41) Qi, X.; Watanabe, M.; Aida, T. M.; Smith, R. L. Catalytic Dehydration of Fructose into 5-Hydroxymethylfurfural by Ion-Exchange Resin in Mixed-Aqueous System by Microwave Heating. *Green Chem.* **2008**, *10* (7), 799–805. <https://doi.org/10.1039/b801641k>.

- (42) Moreau, C.; Durand, R.; Razigade, S.; Duhamet, J.; Faugeras, P.; Rivalier, P.; Pierre, R.; Avignon, G. Dehydration of Fructose to 5-Hydroxymethylfurfural over H-Mordenites. *Appl. Catal. A Gen.* **1996**, *145* (1–2), 211–224. [https://doi.org/10.1016/0926-860X\(96\)00136-6](https://doi.org/10.1016/0926-860X(96)00136-6).
- (43) Ordonsky, V. V.; van der Schaaf, J.; Schouten, J. C.; Nijhuis, T. A. The Effect of Solvent Addition on Fructose Dehydration to 5-Hydroxymethylfurfural in Biphasic System over Zeolites. *J. Catal.* **2012**, *287* (7), 68–75. <https://doi.org/10.1016/j.jcat.2011.12.002>.
- (44) Qi, X.; Watanabe, M.; Aida, T. M.; Smith, R. L. Catalytical Conversion of Fructose and Glucose into 5-Hydroxymethylfurfural in Hot Compressed Water by Microwave Heating. *Catal. Commun.* **2008**, *9* (13), 2244–2249. <https://doi.org/10.1016/j.catcom.2008.04.025>.
- (45) Kazi, F. K.; Patel, A. D.; Serrano-Ruiz, J. C.; Dumesic, J. A.; Anex, R. P. Techno-Economic Analysis of Dimethylfuran (DMF) and Hydroxymethylfurfural (HMF) Production from Pure Fructose in Catalytic Processes. *Chem. Eng. J.* **2011**, *169* (1–3), 329–338. <https://doi.org/10.1016/j.cej.2011.03.018>.
- (46) Rosatella, A. A.; Simeonov, S. P.; Frade, R. F. M.; Afonso, C. A. M. 5-Hydroxymethylfurfural (HMF) as a Building Block Platform: Biological Properties, Synthesis and Synthetic Applications. *Green Chem.* **2011**, *13* (4), 754–793. <https://doi.org/10.1039/c0gc00401d>.
- (47) Watanabe, M.; Aizawa, Y.; Iida, T.; Aida, T. M.; Levy, C.; Sue, K.; Inomata, H. Glucose Reactions with Acid and Base Catalysts in Hot Compressed Water at 473 K. *Carbohydr. Res.* **2005**, *340* (12), 1925–1930. <https://doi.org/10.1016/j.carres.2005.06.017>.
- (48) Qi, X.; Watanabe, M.; Aida, T. M.; Smith, R. L. Synergistic Conversion of Glucose into 5-Hydroxymethylfurfural in Ionic Liquid-Water Mixtures. *Bioresour. Technol.* **2012**, *109*, 224–228. <https://doi.org/10.1016/j.biortech.2012.01.034>.
- (49) Dutta, S.; De, S.; Patra, A. K.; Sasidharan, M.; Bhaumik, A.; Saha, B. Microwave Assisted Rapid Conversion of Carbohydrates into 5-Hydroxymethylfurfural Catalyzed by Mesoporous TiO<sub>2</sub>nanoparticles. *Appl. Catal. A Gen.* **2011**, *409–410*, 133–139. <https://doi.org/10.1016/j.apcata.2011.09.037>.
- (50) Byrne, F. P.; Jin, S.; Paggiola, G.; Petchey, T. H. M.; Clark, J. H.; Farmer, T. J.; Hunt, A. J.; Robert McElroy, C.; Sherwood, J. Tools and Techniques for Solvent Selection: Green Solvent Selection Guides. *Sustain. Chem. Process.* **2016**, *4* (1), 7. <https://doi.org/10.1186/s40508-016-0051-z>.
- (51) Zhang, J.; Lin, L.; Liu, S. Efficient Production of Furan Derivatives from a Sugar Mixture by Catalytic Process. *Energy and Fuels* **2012**, *26* (7), 4560–4567. <https://doi.org/10.1021/ef300606v>.
- (52) Takagaki, A.; Ohara, M.; Nishimura, S.; Ebitani, K. A One-Pot Reaction for Biorefinery: Combination of Solid Acid and Base Catalysts for Direct Production of 5-Hydroxymethylfurfural from Saccharides. *Chem. Commun.* **2009**, No. 41, 6276–6278. <https://doi.org/10.1039/b914087e>.
- (53) Tuteja, J.; Nishimura, S.; Ebitani, K. One-Pot Synthesis of Furans from Various Saccharides Using a Combination of Solid Acid and Base Catalysts. *Bull. Chem. Soc.*



- Jpn.* **2012**, *85* (3), 275–281. <https://doi.org/10.1246/bcsj.20110287>.
- (54) Gallo, J. M. R.; Alonso, D. M.; Mellmer, M. A.; Dumesic, J. A. Production and Upgrading of 5-Hydroxymethylfurfural Using Heterogeneous Catalysts and Biomass-Derived Solvents. *Green Chem.* **2013**, *15* (1), 85–90. <https://doi.org/10.1039/c2gc36536g>.
- (55) Moliner, M.; Roman-Leshkov, Y.; Davis, M. E. Tin-Containing Zeolites Are Highly Active Catalysts for the Isomerization of Glucose in Water. *Proc. Natl. Acad. Sci.* **2010**, *107* (14), 6164–6168. <https://doi.org/10.1073/pnas.1002358107>.
- (56) Huang, Y. B.; Chen, M. Y.; Yan, L.; Guo, Q. X.; Fu, Y. Nickel-Tungsten Carbide Catalysts for the Production of 2,5-Dimethylfuran from Biomass-Derived Molecules. *ChemSusChem* **2014**, *7* (4), 1068–1072. <https://doi.org/10.1002/cssc.201301356>.
- (57) Qian, Y.; Zhu, L.; Wang, Y.; Lu, X. Recent Progress in the Development of Biofuel 2,5-Dimethylfuran. *Renew. Sustain. Energy Rev.* **2015**, *41*, 633–646. <https://doi.org/10.1016/j.rser.2014.08.085>.
- (58) Shi, J.; Wang, Y.; Yu, X.; Du, W.; Hou, Z. Production of 2,5-Dimethylfuran from 5-Hydroxymethylfurfural over Reduced Graphene Oxides Supported Pt Catalyst under Mild Conditions. *Fuel* **2016**, *163*, 74–79. <https://doi.org/10.1016/j.fuel.2015.09.047>.
- (59) Chidambaram, M.; Bell, A. T. A Two-Step Approach for the Catalytic Conversion of Glucose to 2,5-Dimethylfuran in Ionic Liquids. *Green Chem.* **2010**, *12* (7), 1253–1262. <https://doi.org/10.1039/c004343e>.
- (60) Binder, J. B.; Raines, R. T. Simple Chemical Transformation of Lignocellulosic Biomass into Furans for Fuels and Chemicals. *J. Am. Chem. Soc.* **2009**, *131* (5), 1979–1985. <https://doi.org/10.1021/ja808537j>.
- (61) Braun, M.; Antonietti, M. A Continuous Flow Process for the Production of 2,5-Dimethylfuran from Fructose Using (Non-Noble Metal Based) Heterogeneous Catalysis. *Green Chem.* **2017**, *19* (16), 3813–3819. <https://doi.org/10.1039/c7gc01055a>.
- (62) Wright, W. R. H.; Palkovits, R. Development of Heterogeneous Catalysts for the Conversion of Levulinic Acid to  $\gamma$ -Valerolactone. *ChemSusChem* **2012**, *5* (9), 1657–1667. <https://doi.org/10.1002/cssc.201200111>.
- (63) Manzer, L. E. Catalytic Synthesis of  $\alpha$ -Methylene- $\gamma$ -Valerolactone: A Biomass-Derived Acrylic Monomer. *Appl. Catal. A Gen.* **2004**, *272* (1–2), 249–256. <https://doi.org/10.1016/j.apcata.2004.05.048>.
- (64) Alonso, D. M.; Wettstein, S. G.; Dumesic, J. A. Gamma-Valerolactone, a Sustainable Platform Molecule Derived from Lignocellulosic Biomass. *Green Chem.* **2013**, *15* (3), 584–595. <https://doi.org/10.1039/c3gc37065h>.
- (65) Serrano-Ruiz, J. C.; West, R. M.; Dumesic, J. A. Catalytic Conversion of Renewable Biomass Resources to Fuels and Chemicals. *Annu. Rev. Chem. Biomol. Eng.* **2010**, *1* (1), 79–100. <https://doi.org/10.1146/annurev-chembioeng-073009-100935>.
- (66) Al-Naji, M. Liquid-Phase Hydrogenation of Lignocellulosic Biomass-Derived Model Mixtures Using Supported Metal Catalysts, Universität Leipzig, 2017.
- (67) Galletti, A. M. R.; Antonetti, C.; De Luise, V.; Martinelli, M. A Sustainable Process for

- the Production of  $\gamma$ -Valerolactone by Hydrogenation of Biomass-Derived Levulinic Acid. *Green Chem.* **2012**, *14* (3), 688–694. <https://doi.org/10.1039/c2gc15872h>.
- (68) Sudhakar, M.; Kumar, V. V.; Naresh, G.; Kantam, M. L.; Bhargava, S. K.; Venugopal, A. Vapor Phase Hydrogenation of Aqueous Levulinic Acid over Hydroxyapatite Supported Metal (M= Pd, Pt, Ru, Cu, Ni) Catalysts. *Appl. Catal. B Environ.* **2016**, *180*, 113–120. <https://doi.org/10.1016/j.apcatb.2015.05.050>.
- (69) Christian, R. V.; Brown, H. D.; Hixon, R. M. Derivatives of  $\gamma$ -Valerolactone, 1,4-Pentanediol and 1,4-Di-( $\beta$ -Cyanoethoxy)-Pentane. *J. Am. Chem. Soc.* **1947**, *69* (8), 1961–1963. <https://doi.org/10.1021/ja01200a036>.
- (70) Yan, Z. P.; Lin, L.; Liu, S. Synthesis of  $\gamma$ -Valerolactone by Hydrogenation of Biomass-Derived Levulinic Acid over Ru/C Catalyst. *Energy and Fuels* **2009**, *23* (8), 3853–3858. <https://doi.org/10.1021/ef900259h>.
- (71) Al-Shaal, M. G.; Wright, W. R. H.; Palkovits, R. Exploring the Ruthenium Catalysed Synthesis of  $\gamma$ -Valerolactone in Alcohols and Utilisation of Mild Solvent-Free Reaction Conditions. *Green Chem.* **2012**, *14* (5), 1260–1263. <https://doi.org/10.1039/c2gc16631c>.
- (72) Michel, C.; Zaffran, J.; Ruppert, A. M.; Matras-Michalska, J.; Jędrzejczyk, M.; Grams, J.; Sautet, P. Role of Water in Metal Catalyst Performance for Ketone Hydrogenation: A Joint Experimental and Theoretical Study on Levulinic Acid Conversion into Gamma-Valerolactone. *Chem. Commun.* **2014**, *50* (83), 12450–12453. <https://doi.org/10.1039/c4cc04401k>.
- (73) Tan, J.; Cui, J.; Deng, T.; Cui, X.; Ding, G.; Zhu, Y.; Li, Y. Water-Promoted Hydrogenation of Levulinic Acid to  $\gamma$ -Valerolactone on Supported Ruthenium Catalyst. *ChemCatChem* **2015**, *7* (3), 508–512. <https://doi.org/10.1002/cctc.201402834>.
- (74) Xiao, C.; Goh, T.-W.; Qi, Z.; Goes, S.; Brashler, K.; Perez, C.; Huang, W. Conversion of Levulinic Acid to  $\gamma$ -Valerolactone over Few-Layer Graphene-Supported Ruthenium Catalysts. *ACS Catal.* **2016**, *6* (2), 593–599. <https://doi.org/10.1021/acscatal.5b02673>.
- (75) Hengne, A. M.; Rode, C. V. Cu-ZrO<sub>2</sub> nanocomposite Catalyst for Selective Hydrogenation of Levulinic Acid and Its Ester to  $\gamma$ -Valerolactone. *Green Chem.* **2012**, *14* (4), 1064–1072. <https://doi.org/10.1039/c2gc16558a>.
- (76) Ewan, B. C. R.; Allen, R. W. K. A Figure of Merit Assessment of the Routes to Hydrogen. *Int. J. Hydrogen Energy* **2005**, *30* (8), 809–819. <https://doi.org/10.1016/j.ijhydene.2005.02.003>.
- (77) Tuteja, J.; Choudhary, H.; Nishimura, S.; Ebitani, K. Direct Synthesis of 1,6-Hexanediol from HMF over a Heterogeneous Pd/ZrP Catalyst Using Formic Acid as Hydrogen Source. *ChemSusChem*. 2014, pp 96–100. <https://doi.org/10.1002/cssc.201300832>.
- (78) Son, P. A.; Nishimura, S.; Ebitani, K. Production of  $\gamma$ -Valerolactone from Biomass-Derived Compounds Using Formic Acid as a Hydrogen Source over Supported Metal Catalysts in Water Solvent. *RSC Adv.* **2014**, *4* (21), 10525–10530. <https://doi.org/10.1039/c3ra47580h>.
- (79) Braden, D. J.; Henao, C. A.; Heltzel, J.; Maravelias, C. C.; Dumesic, J. A. Production of Liquid Hydrocarbon Fuels by Catalytic Conversion of Biomass-Derived Levulinic

- Acid. *Green Chem.* **2011**, *13* (7), 1755–1765. <https://doi.org/10.1039/c1gc15047b>.
- (80) Yuan, J.; Li, S. S.; Yu, L.; Liu, Y. M.; Cao, Y.; He, H. Y.; Fan, K. N. Copper-Based Catalysts for the Efficient Conversion of Carbohydrate Biomass into  $\gamma$ -Valerolactone in the Absence of Externally Added Hydrogen. *Energy Environ. Sci.* **2013**, *6* (11), 3308–3313. <https://doi.org/10.1039/c3ee40857d>.
- (81) Al-Naji, M.; Yepez, A.; Balu, A. M.; Romero, A. A.; Chen, Z.; Wilde, N.; Li, H.; Shih, K.; Gläser, R.; Luqueb, R. Insights into the Selective Hydrogenation of Levulinic Acid to  $\gamma$ -Valerolactone Using Supported Mono- and Bimetallic Catalysts. *Journal of Molecular Catalysis A: Chemical*. 2016, pp 145–152. <https://doi.org/10.1016/j.molcata.2016.03.015>.
- (82) Al-Naji, M.; Popova, M.; Gläser, R.; Wilde, N. ZrO<sub>2</sub>-Based Catalysts with Enhanced Hydrothermal Stability for the Aqueous-Phase in-Situ Hydrogenation of Levulinic Acid. 255th American Chemical Society (Nexus of Food, Energy and Water): New Orleans 2018.
- (83) M. Al-Naji; Aelst, J. Van; Wilde, N.; Gläser, R.; Sels, B. F. Selective Hydrogenation of  $\gamma$ -Valerolactone to Pentanoic Acid over Pt/Zeolite Using Formic Acid as a Hydrogen Source. 255th American Chemical Society (Nexus of Food, Energy and Water): New Orleans 2018.
- (84) Jüntgen, H. Activated Carbon as Catalyst Support. A Review of New Research Results. *Fuel* **1986**, *65* (10), 1436–1446. [https://doi.org/10.1016/0016-2361\(86\)90120-1](https://doi.org/10.1016/0016-2361(86)90120-1).
- (85) Yue, Z.; Economy, J. Synthesis of Highly Mesoporous Carbon Pellets from Carbon Black and Polymer Binder by Chemical Activation. *Microporous Mesoporous Mater.* **2006**, *96* (1–3), 314–320. <https://doi.org/10.1016/j.micromeso.2006.07.025>.
- (86) Nickel, W.; Oschatz, M.; Rico-Francés, S.; Klosz, S.; Biemelt, T.; Mondin, G.; Eychmüller, A.; Silvestre-Albero, J.; Kaskel, S. Synthesis of Ordered Mesoporous Carbon Materials by Dry Etching. *Chem. - A Eur. J.* **2015**, *21* (42), 14753–14757. <https://doi.org/10.1002/chem.201502038>.
- (87) Fechler, N. Salts as Highly Diverse Porogens : Functional Ionic Liquid-Derived Carbons and Carbon-Based Composites for Energy-Related Applications. **2012**.
- (88) Ergun, S.; Orning, A. A. Fluid Flow through Randomly Packed Columns and Fluidized Beds. *Ind. Eng. Chem.* **2005**, *41* (6), 1179–1184. <https://doi.org/10.1021/ie50474a011>.
- (89) Rothe, R.; Antonietti, M.; Fechler, N. The Bakery of High-End Sorption Carbons: Sugar-Urea Doughs as Processable Precursors for Functional Carbons. *J. Mater. Chem. A* **2017**, *5* (31), 16352–16358. <https://doi.org/10.1039/c7ta02052j>.
- (90) Kim, D. P.; Lin, C. L.; Mihalisin, T.; Labes, M. M.; Heiney, P. Electronic Properties of Nitrogen-Doped Graphite Flakes. *Chem. Mater.* **1991**, *3* (4), 686–692. <https://doi.org/10.1021/cm00016a023>.
- (91) Sotomayor, F. J.; Cychosz, K. A.; Thommes, M. Characterization of Micro/Mesoporous Materials by Physisorption : Concepts and Case Studies. *Acc. Mater. Surf. Res* **2018**, *3* (2), 36–37.
- (92) Strubel, P.; Thieme, S.; Biemelt, T.; Helmer, A.; Oschatz, M.; Brückner, J.; Althues, H.; Kaskel, S. ZnO Hard Templating for Synthesis of Hierarchical Porous Carbons with Tailored Porosity and High Performance in Lithium-Sulfur Battery. *Adv. Funct.*

- Mater.* **2015**, 25 (2), 287–297. <https://doi.org/10.1002/adfm.201402768>.
- (93) Brockner, W.; Ehrhardt, C.; Gjikaj, M. Thermal Decomposition of Nickel Nitrate Hexahydrate,  $\text{Ni}(\text{NO}_3)_2 \cdot 6\text{H}_2\text{O}$ , in Comparison to  $\text{Co}(\text{NO}_3)_2 \cdot 6\text{H}_2\text{O}$  and  $\text{Ca}(\text{NO}_3)_2 \cdot 4\text{H}_2\text{O}$ . *Thermochim. Acta* **2007**, 456 (1), 64–68. <https://doi.org/10.1016/j.tca.2007.01.031>.
- (94) Agriculture, U. S. D. of; Service, A. R. USDA Food Composition Databases <https://ndb.nal.usda.gov/ndb/>.
- (95) Goertzen, S. L.; Thériault, K. D.; Oickle, A. M.; Tarasuk, A. C.; Andreas, H. A. Standardization of the Boehm Titration. Part I.  $\text{CO}_2$  Expulsion and Endpoint Determination. *Carbon N. Y.* **2010**, 48 (4), 1252–1261. <https://doi.org/10.1016/j.carbon.2009.11.050>.
- (96) Contescu, A.; Contescu, C.; Putyera, K.; Schwarz, J. A. Surface Acidity of Carbons Characterized by Their Continuous PK Distribution and Boehm Titration. *Carbon N. Y.* **1997**, 35 (1), 83–94. [https://doi.org/10.1016/S0008-6223\(96\)00125-X](https://doi.org/10.1016/S0008-6223(96)00125-X).
- (97) Reichle, R. A.; McCurdy, K. G.; Hepler, L. G. Zinc Hydroxide: Solubility Product and Hydroxy-Complex Stability Constants from 12.5–75 °C. *Can. J. Chem.* **2006**, 53 (24), 3841–3845. <https://doi.org/10.1139/v75-556>.
- (98) Swagelok. Tubing Data. **2017**.
- (99) Swagelok. *Proportional Relief Valves*.
- (100) Mears, D. E. The Role of Axial Dispersion in Trickle-Flow Laboratory Reactors. *Chem. Eng. Sci.* **1971**, 26 (9), 1361–1366. [https://doi.org/10.1016/0009-2509\(71\)80056-8](https://doi.org/10.1016/0009-2509(71)80056-8).
- (101) Gierman, H. Design of Laboratory Hydrotreating Reactors. *Appl. Catal.* **2002**, 43 (2), 277–286. [https://doi.org/10.1016/S0166-9834\(00\)82732-3](https://doi.org/10.1016/S0166-9834(00)82732-3).
- (102) Maestri, M.; Tronconi, E.; Berger, R.; Kapteijn, F.; Moulijn, J. A. *EUROKIN - Overview of Requirements for Measurement of Intrinsic Kinetics in and Overview of Correlations for Characteristics of the G-S and L-S Fixed-Bed Reactor*; 2014.
- (103) Onda, A.; Ochi, T.; Kajiyoshi, K.; Yanagisawa, K. Lactic Acid Production from Glucose over Activated Hydrotalcites as Solid Base Catalysts in Water. *Catal. Commun.* **2008**, 9 (6), 1050–1053. <https://doi.org/10.1016/j.catcom.2007.10.005>.
- (104) Li, Y.; Lv, G.; Wang, Y.; Deng, T.; Wang, Y.; Hou, X.; Yang, Y. Synthesis of 2,5-Hexanedione from Biomass Resources Using a Highly Efficient Biphasic System. *ChemistrySelect* **2016**, 1 (6), 1252–1255. <https://doi.org/10.1002/slct.201600280>.
- (105) Barton, S. S.; Evans, M. J. B.; Halliop, E.; MacDonald, J. A. F. Acidic and Basic Sites on the Surface of Porous Carbon. *Carbon N. Y.* **1997**, 35 (9), 1361–1366. [https://doi.org/10.1016/S0008-6223\(97\)00080-8](https://doi.org/10.1016/S0008-6223(97)00080-8).
- (106) Gawade, A. B.; Tiwari, M. S.; Yadav, G. D. Biobased Green Process: Selective Hydrogenation of 5-Hydroxymethylfurfural to 2,5-Dimethyl Furan under Mild Conditions Using Pd-Cs 2.5 H 0.5 PW 12 O 40 /K-10 Clay. *ACS Sustain. Chem. Eng.* **2016**, 4 (8), 4113–4123. <https://doi.org/10.1021/acssuschemeng.6b00426>.
- (107) Op De Beeck, B.; Dusselier, M.; Geboers, J.; Holsbeek, J.; Morré, E.; Oswald, S.; Giebel, L.; Sels, B. F. Direct Catalytic Conversion of Cellulose to Liquid Straight-

- Chain Alkanes. *Energy Environ. Sci.* **2015**, 8 (1), 230–240. <https://doi.org/10.1039/c4ee01523a>.
- (108) Saha, B.; Bohn, C. M.; Abu-Omar, M. M. Zinc-Assisted Hydrodeoxygenation of Biomass-Derived 5-Hydroxymethylfurfural to 2,5-Dimethylfuran. *ChemSusChem* **2014**, 7 (11), 3095–3101. <https://doi.org/10.1002/cssc.201402530>.
- (109) Parsell, T. H.; Owen, B. C.; Klein, I.; Jarrell, T. M.; Marcum, C. L.; Hauptert, L. J.; Amundson, L. M.; Kenttämä, H. I.; Ribeiro, F.; Miller, J. T.; et al. Cleavage and Hydrodeoxygenation (HDO) of C–O Bonds Relevant to Lignin Conversion Using Pd/Zn Synergistic Catalysis. *Chem. Sci.* **2013**, 4 (2), 806–813. <https://doi.org/10.1039/C2SC21657D>.
- (110) Louie, Y. L.; Tang, J.; Hell, A. M. L.; Bell, A. T. Kinetics of Hydrogenation and Hydrogenolysis of 2,5-Dimethylfuran over Noble Metals Catalysts under Mild Conditions. *Appl. Catal. B Environ.* **2017**, 202, 557–568. <https://doi.org/10.1016/j.apcatb.2016.09.046>.
- (111) Yang, Y.; Liu, Q.; Li, D.; Tan, J.; Zhang, Q.; Wang, C.; Ma, L. Selective Hydrodeoxygenation of 5-Hydroxymethylfurfural to 2,5-Dimethylfuran on Ru–MoO<sub>x</sub>/C Catalysts. *RSC Adv.* **2017**, 7 (27), 16311–16318. <https://doi.org/10.1039/C7RA00605E>.
- (112) Jackson, M. A.; Appell, M.; Blackburn, J. A. Hydrodeoxygenation of Fructose to 2,5-Dimethyltetrahydrofuran Using a Sulfur Poisoned Pt/C Catalyst. *Ind. Eng. Chem. Res.* **2015**, 54 (28), 7059–7066. <https://doi.org/10.1021/acs.iecr.5b00766>.
- (113) Yamaguchi, A.; Hiyoshi, N.; Sato, O.; Shirai, M. Stereoselective Intramolecular Dehydration of 2,5-Hexanediol in High-Temperature Liquid Water with High-Pressure Carbon Dioxide. *ACS Catal.* **2011**, 1 (1), 67–69. <https://doi.org/10.1021/cs100064a>.
- (114) Van Haasterecht, T.; Swart, M.; De Jong, K. P.; Bitter, J. H. Effect of Initial Nickel Particle Size on Stability of Nickel Catalysts for Aqueous Phase Reforming. *J. Energy Chem.* **2016**, 25 (2), 289–296. <https://doi.org/10.1016/j.jechem.2016.01.006>.
- (115) Serrano-Ruiz, J. C.; Wang, D.; Dumesic, J. A. Catalytic Upgrading of Levulinic Acid to 5-Nonanone. *Green Chem.* **2010**, 12 (4), 574–577. <https://doi.org/10.1039/b923907c>.
- (116) Abdelrahman, O. A.; Heyden, A.; Bond, J. Q. Analysis of Kinetics and Reaction Pathways in the Aqueous-Phase Hydrogenation of Levulinic Acid to Form  $\gamma$ -Valerolactone over Ru/C. *ACS Catal.* **2014**, 4 (4), 1171–1181. <https://doi.org/10.1021/cs401177p>.
- (117) Al-Shaal, M. G.; Dzierbinski, A.; Palkovits, R. Solvent-Free  $\gamma$ -Valerolactone Hydrogenation to 2-Methyltetrahydrofuran Catalysed by Ru/C: A Reaction Network Analysis. *Green Chem.* **2014**, 16 (3), 1358–1364. <https://doi.org/10.1039/c3gc41803k>.
- (118) Grilc, M.; Likozar, B. Levulinic Acid Hydrodeoxygenation, Decarboxylation and Oligomerization over NiMo/Al<sub>2</sub>O<sub>3</sub> catalyst to Bio-Based Value-Added Chemicals: Modelling of Mass Transfer, Thermodynamics and Micro-Kinetics. *Chem. Eng. J.* **2017**, 330 (February), 383–397. <https://doi.org/10.1016/j.cej.2017.07.145>.
- (119) Zhou, J.; Zhu, R.; Deng, J.; Fu, Y. Preparation of Valeric Acid and Valerate Esters from Biomass-Derived Levulinic Acid Using Metal Triflates + Pd/C. *Green Chem.* **2018**, 20 (17), 3974–3980. <https://doi.org/10.1039/c8gc01606b>.